

Contemporary Slip Rates of All Active Faults in the Indo–Asian Collision Zone

Richard Styron, GEM Foundation (richard.styron@globalquakemodel.org)

Abstract

Deformation within the Indo–Asian Collision Zone is accommodated on a complex network of faults spanning thousands of kilometers in any direction. In order to characterize faulting in the orogen for seismic hazard assessment, a new fault database was compiled, resulting in ~1000 fault traces mapped at around 1:100,000. A block model was created simultaneously with the fault mapping to estimate robust, internally-consistent slip rates on all mapped faults. The block model inverts >3000 GNSS velocities and ~200 Quaternary geologic slip rates. The results yield slip rates that are generally quite consistent with geologic estimates, indicating that decadal and millennial-scale deformation rates are compatible. Additionally, the great strike-slip faults of the orogen are the dominant faults of the orogen's interior, accumulating and redistributing slip from linked, subordinate fault networks in a way similar to transfer faults within a basin or thrust belt, but on much larger scale.

Contents

1	Introduction	3
1.1	Tectonic overview	4
2	Methods	4
2.1	Fault and block mapping	5
2.2	Fault and geodetic data compilation	6
2.2.1	GNSS data compilation	6
2.2.2	Geologic slip rates	6
2.3	Block modeling	8
2.3.1	Preparation of velocity observations	8
2.3.2	Solution strategy	9
2.3.3	The effects of fault locking on geodetic velocities	10
2.3.4	Block velocity closure constraints	10
2.3.5	Propagation of uncertainty	11
3	Results and Regional Kinematics	11
3.1	Evaluation of model fits	11
3.2	Orogen-scale transfer faults	11
3.3	Tien Shan	13
3.3.1	NW-striking dextral faults	16
3.4	Pamir	16
3.4.1	Western Tarim Basin	18
3.5	Himalaya	18
3.5.1	Main Frontal Thrust	18
3.5.2	Intra-Himalayan faults	20
3.6	Central Tibet	21
3.6.1	Karakoram fault	21
3.6.2	Southern Tibetan rifts and dextral faults	21
3.6.3	Central Tibetan sinistral faults and associated normal faults	22
3.6.4	Tanggula Shan and central–eastern Tibet	23

43	3.7 Northern Tibet	24
44	3.7.1 Kunlun fault system	24
45	3.7.2 Altyn Tagh fault system	25
46	3.7.3 Gobi-Altai and Gobi	26
47	3.7.4 Qimen Tagh	27
48	3.7.5 Qilian Shan and Hexi Corridor	28
49	3.7.6 Haiyuan fault	28
50	3.7.7 Qinling fault	28
51	3.8 Eastern Tibet and the Longmen Shan	28
52	3.8.1 Eastern termination of the Kunlun fault	28
53	3.8.2 Longmen Shan	30
54	3.8.3 Xianshuihe–Xiaojiang fault system	30
55	3.9 Southeastern Tibet and Indochina	32
56	3.9.1 High-elevation transtensive faults	32
57	3.9.2 Zhongdian–Lijiang–Dali fault system	32
58	3.9.3 Red River fault system	33
59	3.9.4 Northeast Assam and Mishmi thrust	34
60	3.9.5 Clockwise rotation and sinistral shear in Myanmar and Yunnan	34
61	3.9.6 Sagaing fault	34
62	3.9.7 Indo-Burman ranges and the Shillong Plateau	35
63	3.10 Eastern and Northeastern China	36
64	3.10.1 Ordos plateau and marginal grabens	36
65	3.10.2 Tangshan fault and Bohai Sea	38
66	3.10.3 Yilan-Yitong fault, Tanlu fault	38
67	4 Discussion	38
68	4.1 Comparison of results with previous geodetic studies	38
69	4.2 Comparison of geologic and geodetic slip rates	39
70	5 Conclusions	40
71	6 Data Availability	40
72	References	40

[Note to editors and reviewers: Fault slip rates and some other numbers in this manuscript often set in an italic or bold font. Rates in italics are pulled from the output files from the block inversion and inserted into the manuscript via a Python script. Rates (or other numbers) in bold are not automated, and need to be updated manually. The use of these fonts helps me keep track of what values need to be checked when the data, block geometry, or inversion is updated, both in terms of the actual numerical value and the context in which it is interpreted. When the model is finalized and the paper has been accepted, I will remove these fonts but in the mean time they are extremely helpful to me, so please do not mind the typesetting.]

1 Introduction

In this paper, a regionally-integrated active fault database for the Indo-Asian collision zone (Figure 1) is presented as HimaTibetMap v.2.0. This represents a major update to HimaTibetMap v.1.0 (Styron et al., 2010; Taylor & Yin, 2009). The most substantial changes are the addition of slip rates for every structure, informed by a high-resolution block model, and a complete remapping of the original HimaTibetMap database at a much higher resolution. However, in many regions new faults have been added to the database, and a few structures are also omitted, typically because evidence for them was lacking or they were not able to be placed within the block framework (i.e., they were interpreted as minor splay faults).

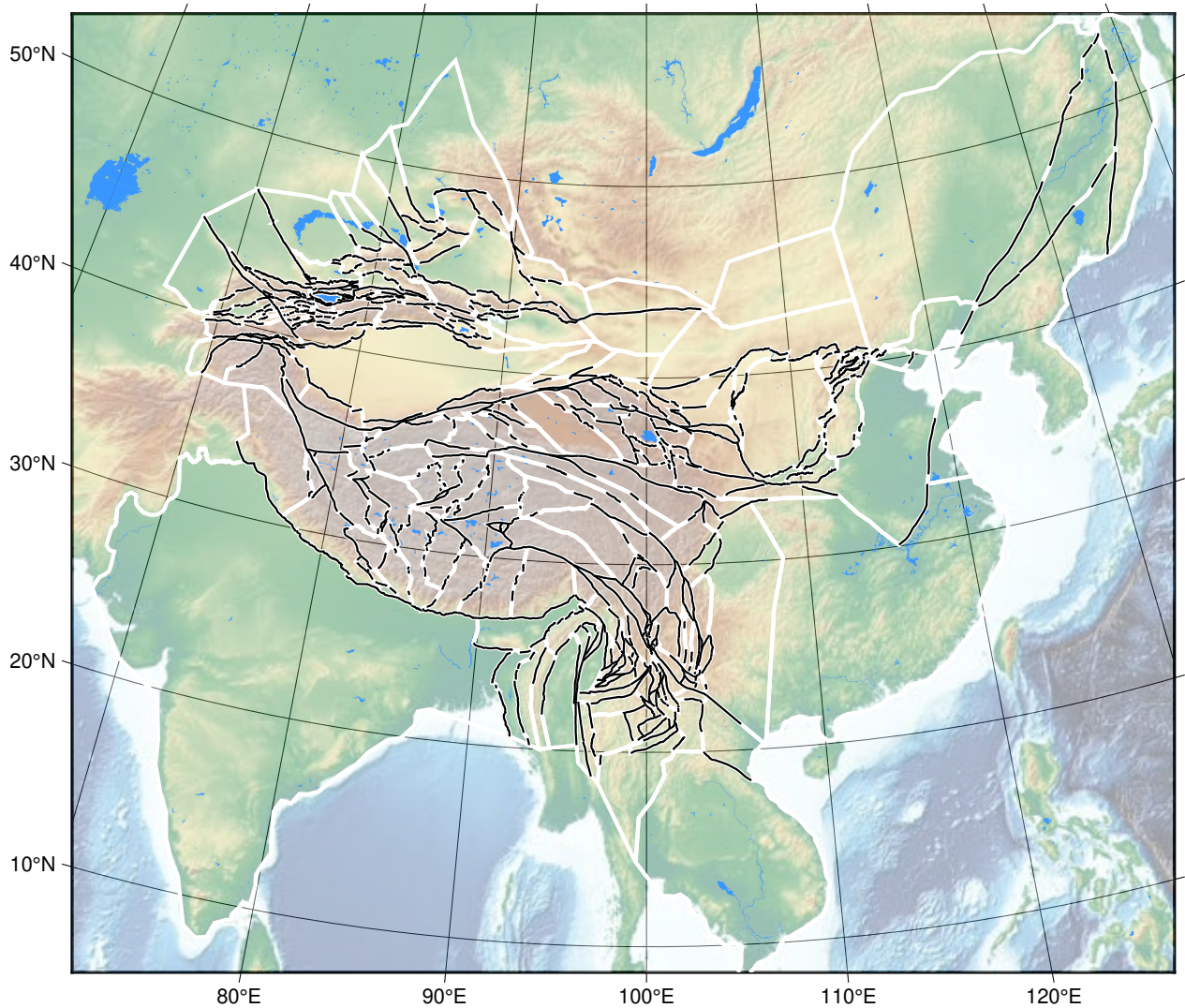


Figure 1: Faults and block model of the study area.

The work is motivated by the need for accurate and internally-consistent fault geometries, kinematics and slip rates for a new probabilistic seismic hazard model for China being constructed by the Global Earthquake Model Foundation (GEM). Consequently, this paper will focus on the kinematics of sub-regions of the study area, particularly those that are elucidated by the block modeling; this is intended to provide documentation for the fault data that inform the seismic hazard model. As a consequence, less attention will be paid to the tectonic implications of these new data and interpretations to questions of geodynamics and orogenic evolution, however inseparable these may be in reality. The data and code are publicly available and it is hoped that they will be of utility to interested scientists. The implications of certain findings for seismic hazard will also not be discussed quantitatively or in much detail. These discussions will instead be found in a forthcoming publication describing the seismic hazard model (Chartier et al., *in prep*), where they may be placed within a quantitative context.

1.1 Tectonic overview

The Indo-Asian collision zone comprises a number of orogenic provinces undergoing deformation related to India's convergence with southeastern Asia (e.g., Tapponnier & Molnar, 1977; Taylor & Yin, 2009). The Tibetan plateau is at the center and is the largest province, and is characterized by E-W extension and N-S contraction, largely accommodated along N-trending rifts and NE- and SE-trending strike-slip fault systems (Armijo et al., 1989; Taylor et al., 2003), throughout its central and western extent; deformation on the eastern and northeastern margins is generally transpressive (Densmore et al., 2007; e.g., Yin et al., 2008). The Himalaya lies at the southern margin of Tibet, and most active deformation occurs on the Main Himalayan Thrust, which is the megathrust separating the modern continents of India and Eurasia (e.g., P Kapp & DeCelles, 2019), though some deformation occurs within the Himalayan thrust wedge itself, with similar characteristics to adjacent Tibet (Styron et al., 2011). These orogenic provinces grade into others to the west, north, and east, where other plate interactions may be important.

The Pamir orogenic province is at the northwestern end of the Himalaya and Tibet, which is bound by rapidly-slipping E-striking thrusts, and has transtensive deformation in its interior (e.g., Metzger et al., 2017). North of the Pamir, the NE-trending Tien Shan thrust belt takes up a sizeable fraction of India-Eurasia convergence, and contains long but fairly slowly-slipping NW-striking strike-slip faults that extend far northwest into the Kazakh platform (Tapponnier & Molnar, 1979). Structures in the eastern end of the Tien Shan link with those of the Altai belt of Russia and Mongolia, and the Gobi-Altai region in Mongolia and China, which is part of a system of deformation that continues northeast through the Baikal rift into the Russian Arctic and north Pacific (Cunningham, 2013; Tapponnier & Molnar, 1979), though these latter regions are not covered here.

Deformation in northeastern Tibet continues east through north-central China to the Bohai and Japan seas at rates that generally decrease eastward, though extremely damaging earthquakes have occurred here throughout history (McGuire et al., 1992). Southeastern Tibet has a globally-unique, complex arcuate strike-slip fault system that extends south into Indochina and the tectonic systems of Sundaland and the equatorial western Pacific and Indonesia (Yu Wang et al., 2014).

The orogen is notable for the number of great (>1000 km) strike-slip faults that are located well away from the boundary between the Eurasian and Indian plates (located at the Main Himalayan Thrust and Sagaing fault). This list includes the Talas-Ferghana, Karakoram, Altyn Tagh, Jiali-Red River, Xianshuehe-Xiaojiang, Kunlun and Haiyuan fault systems. The 3000+ km Yitong-Yulang fault system in northeastern China is perhaps outside of the orogen but longer still. Additionally, the system of arcuate strike-slip faults oriented concentrically around the eastern terminus of the Himalaya (termed the Eastern Himalaya syntaxis) is without an analog today. No other contemporary orogen offers this breadth of strike-slip faulting.

The role of the great strike-slip faults in a fault network perspective is perhaps under-discussed in the literature (in contrast to their role in Tibetan orogenesis, e.g. Peltzer & Tapponnier (1988)), and will receive some discussion herein.

2 Methods

The fault data and slip rates presented here were produced through a joint mapping-block modeling process. Faults and blocks were mapped in a Geographic Information Systems (GIS) program, and the block modeling was

performed with the program *Oiler* (Styron, 2022b), which was developed during this project (see *Data Availability*). *Oiler* predicts fault slip rates by inverting GNSS geodetic velocities and fault slip rates for relative block motions, and fault slip rates are considered to be the relative velocities of the blocks separated by each fault at the location of the faults. All data and the script to run the inversion are found in the supplementary materials as well as in a repository on GitHub (Styron, 2022a).

It is important to note that all faults occupy block boundaries, but not all block boundary segments are faults. Faults are mapped where there are clear signs of continuous, localized active deformation (as in most or all active fault mapping projects) but off-fault block boundaries are drawn to connect faults to form closed polygons. The nature of strain at these off-fault block boundaries is not yet known, but a subject of ongoing research by the author.

2.1 Fault and block mapping

Faults and blocks were mapped in QGIS (Team, 2022), broadly simultaneously, on 30 m Shuttle Radar Topographic Mission topographic data and derivatives (primarily hillshades) and satellite imagery aggregated by Google. Relevant publications, particularly field studies, and existing digital fault data, primarily *HimaTibetMap v.1* (Styron et al., 2010; Taylor & Yin, 2009) and the GEM Global Active Faults Database (Styron & Pagani, 2020), were frequently consulted as references but generally not viewed during mapping, to encourage a fresher evaluation of fault trace locations as expressed in the topography and satellite imagery. Nonetheless, the representations of the fault traces made by different mappers in different years tend to be quite similar apart from issues related to map resolution.

The mapping workflow used here is an iterative process. First, fault traces for an area were mapped in a draft GIS dataset as Polyline data, based on previous work and the topographic expressions of faulting. Indicators for faulting at any time in the past, as would be preserved in the bedrock by obvious juxtaposition of rock units, offset markers, preferential erosion along faults, were considered, primarily to gauge the location and kinematics of potentially active faults. Then, the fault trace and surroundings were searched for signs of Quaternary faulting such as the disruption of young sedimentary deposits and very sharp fault scarps. A more full treatment of the methods used to evaluate the activity of faults is given by Styron et al. (2020).

Next, blocks were created in a separate GIS layer of Polygon type. The block boundaries are located on the fault traces where the fault traces are present. The boundaries were drawn crudely as drafts away from the faults initially, and then refined as the model geometry took shape. After many adjustments and test runs of the block inversion code, the fault and block geometries are finalized. The target resolution for fault mapping is around 1:100,000, though this may change based on the resolution of the satellite imagery and the clarity of the fault's expression in the topographic and photographic imagery.

Drawing blocks requires the explicit connection of disconnected faults. These connections may be obvious: where deformation between nearby fault sections may be evident but not localized to a single clear fault trace, or perhaps hidden by rugged terrain or areas of rapid sedimentation, or where the sign of Quaternary activity dies out for some distance along an obvious structure such as an old fault or suture zone, that is elsewhere clearly reactivated. Another scenario is commonly found in long rifts such as in Tibet: the side of the rift graben that contains the master normal fault switches one or more times along strike, so connections to these traces represent relays with no surface signature. In the best cases, the search for a site to locate the block boundary actually leads to the discovery of a new fault.

In other cases, the connections may be unclear. In these instances, faults were connected through geologic reasoning and experimentation. Given a set of faults and velocity data, different geometries or topologies of connections will predict different rates and kinematics. A primary goal when evaluating potential connections is to preserve the interpreted kinematics of all faults, and, if possible, to connect faults so that the kinematics of the connector block segment are similar to those of the faults. Similarly, the goodness of fit to the GNSS and fault slip rate observations will be affected by different configurations, so this criteria was used where possible (though for most difficult choices, there was no statistically significant difference). Another goal is to minimize the length of the connecting segments. Because this work is performed in order to get fault geometries and slip rates for seismic hazard analysis, the goal is to maximize the amount of deformation that can credibly be allocated onto faults and minimize the rest, as it is not currently straightforward to include into a seismic hazard model.

If a good potential structure is found that could credibly represent a block boundary, but without the characteristics indicating active faulting that would lead to a fault being mapped, the block boundary was mapped along the trace of this structure, similar to how a fault is mapped, at resolutions of around 1:200,000. If nothing is found, then a very coarse boundary was mapped at a much higher resolution.

Throughout this process, it was much more common to be confident that two faults are connected with a clear topology but with no obvious place to put a block boundary (i.e., one candidate location clearly better than others), than to have multiple conflicting topologies that seem equally credible.

Another constraint on block geometry is the location and density of the geodetic and geologic data used to solve for the block motions. If geodetic stations are numerous and dense, and fault slip rates are known, then the motions of many small blocks may be well constrained. If faults are unclear in the landscape and unstudied, and geodetic stations are sparse, it may be beneficial to characterize an area with a few large blocks, which may mean removing some active faults from the model. This was mostly an issue in Tibet, where the data density is very low away from a few transects, and deformation is in placed distributed over complex fault systems. Preliminary work integrating high-resolution, wide-scale velocity fields derived from InSAR (Wright et al., 2021) has begun, which will greatly reduce this tradeoff in areas of good InSAR coverage.

This workflow has benefits and costs compared to others. The methods here rely heavily on time-intensive geologic mapping and the subjective judgement of the mapper, but offer great detail compared to previous efforts, yielding high-resolution fault mapping that is deeply integrated with the block model geometry, over a very broad area of southeastern Asia. But it is not the only way, and many geometrically simpler models have been made over different regions within this model.

Additionally, Evans et al. (2015) have developed a method where blocks are formed from disconnected faults algorithmically, and then the model is simplified based on evaluation of a goodness of fit criterion. This places the ‘subjectivity’ in the choice and design of the algorithm and the parameterization of the goodness of fit criterion rather than in the many block construction choices, and is more reproducible. In the absence of direct comparisons starting from the same fault and geodesy data, it is not possible to evaluate the impact of this type of workflow on the results, so the selection of workflow must depend on the competencies of the workers.

The final block model contains **264** blocks and **987** faults.

2.2 Fault and geodetic data compilation

2.2.1 GNSS data compilation

GNSS data was compiled from several recent compilations and other studies. The main dataset used was assembled by M. Wang & Shen (2020) and is primarily a new solution for data from the extensive Crustal Movement Observation Network of China as well as from other regional studies. Additional data outside of China were taken from the compilation by Kreemer et al. (2014) and the study by Metzger et al. (2020). All GNSS velocities are referenced to stable Eurasia. When a single GNSS station has vectors present in multiple datasets, the vector from the newest dataset is used. This results in **3364** GNSS velocities in the block model, out of **4043** in the total compilation (the remainder are outside of blocks in the model, and are discarded).

2.2.2 Geologic slip rates

Almost 200 Quaternary geologic slip rates were compiled for this study from the literature, in what is hoped to be a comprehensive collection as of mid-2021. These use neotectonic techniques, where rates are estimated by measuring and dating offset geologic or geomorphic markers, rather than slip rates derived from paleoseismology, which may yield inaccurate slip rates if fewer than 5-10 events are measured Styron (2019). Rates were compiled if the study sites could be precisely located in topographic or satellite imagery, or if the study included spatial coordinates. As explained in Section 2.3, the point locations of slip rate sites are used in the block inversion, rather than slip rates ascribed more generally to some fault or fault section; this is important as slip rates may change along strike if an Euler pole describing block motion is close to the block boundary. This requirement unfortunately prevents the use of a few slip rate studies, particularly older studies and those from the Chinese literature (which may have identifying information that I cannot translate).

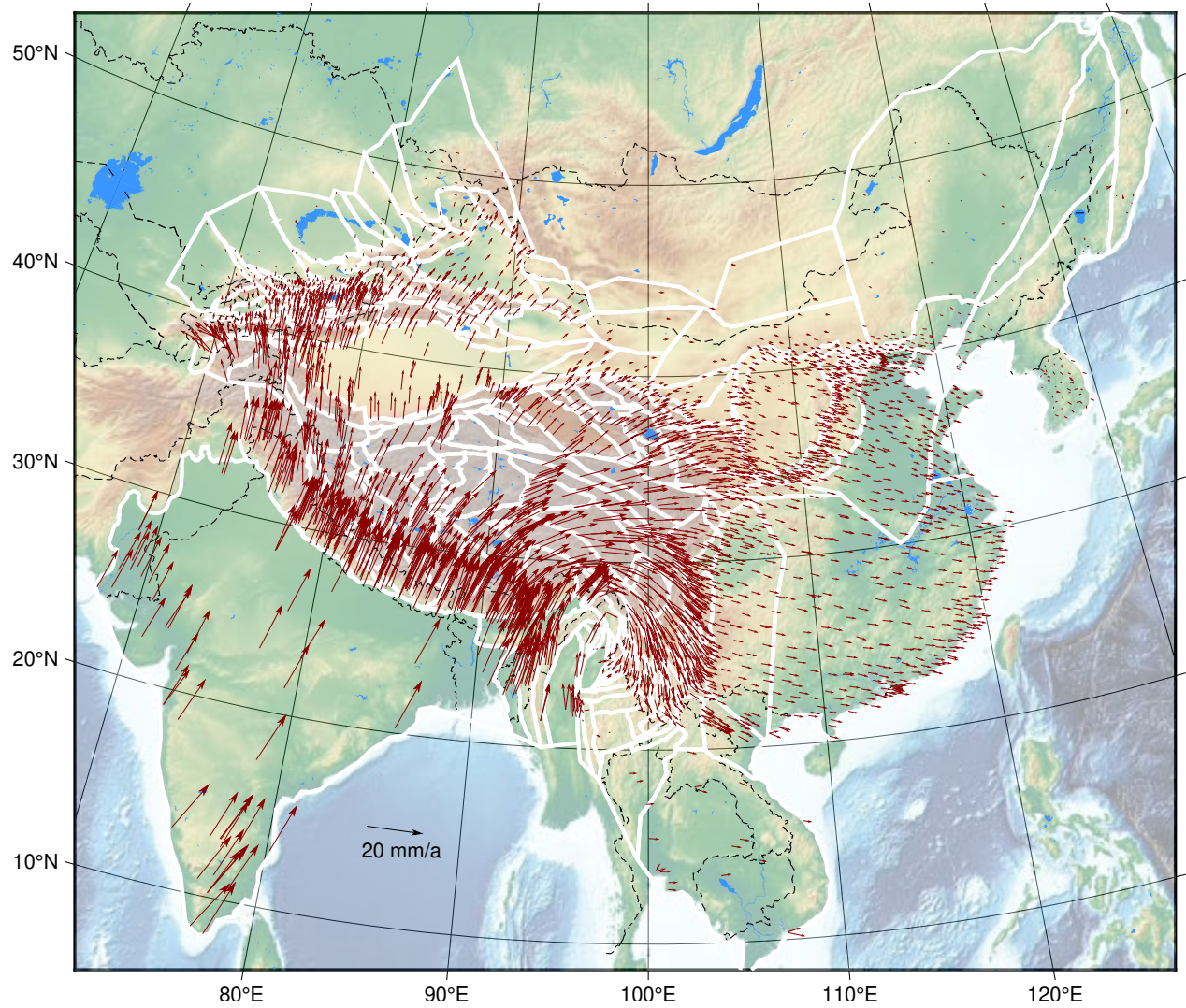


Figure 2: GNSS velocities used in the study. Velocity vectors are shown here without uncertainty ellipses to aid in clarity.

Of the 198 compiled Quaternary slip rates, more than three quarters (166) were used in the inversion. Rates were not used if they were not thought to accurately represent slip rates on the structure they are most closely associated with. In some cases, they may be too far away from a fault in the study (such as on a minor splay). In other cases, rates were not used if the study uses dating assumptions that have been later shown to be problematic, yielding rates that are in conflict with other observations and inferences. Many of the studies of strike-slip faults before the late 2000s utilize flights of fluvial terraces that are differentially offset, and treat the (younger) lower terrace ages as the date of zero offset of the terrace riser rather than the (older) upper terrace age, which has the potential to greatly overestimate slip rates. Following Lensen (1964), Cowgill (2007) and Gold et al. (2009) systematically studied the reconstruction process and found that using the upper terrace ages for many Tibetan faults increases the congruence with slip rates from other datasets. Similarly, some older studies use charcoal from sag ponds or tectonically dammed drainages to estimate the age since the drainages were unmodified (e.g., Burtman et al., 1996) though subsequent investigation (e.g., Rizza et al., 2019) has shown that these dates more likely record the timing of the most recent surface-breaking earthquake, and that the measured offsets have been accumulating for much longer. This category of error also yields slip rates that are much higher than rates observed by other means. Other studies do not directly date the earth materials that are offset but infer ages based on climate events; these are not here considered reliable. Quaternary slip rates that are compiled but not used in the inversion are included in the supplementary data for potential use by others.

2.3 Block modeling

The block model computations were performed using *Oiler* (Styron, 2022b), a block modeling package written in the Julia language, a relatively new programming language designed for high-performance numerical computing (Bezanson et al., 2017). *Oiler* is free and open-source software (see **Data Availability** for more information).

Oiler solves for the best-fit poles of rotation (Euler poles) of the blocks via an inversion of GNSS velocities and Quaternary fault slip rates. *Oiler* draws heavily from previous work in this domain, particularly the mathematical formulations of B. J. Meade & Loveless (2009), Chase (1972), and Cox & Hart (1986). The work by B. J. Meade & Loveless (2009) was most influential. B. J. Meade & Loveless (2009) describe a linearization of the problem of solving for Euler poles given velocity observations on a spherical Earth, such that Euler poles are the solution to a system of linear equations based on the velocity observations. This linearization allows one to solve the system for the globally optimal Euler pole parameters using the extremely common and well-optimized linear regression techniques, obviating the need for more complex and computationally-intensive nonlinear optimization used by many previous workers (Chase, 1972; McCaffrey, 2002; Minster et al., 1974). Fault slip rates in this framework are linear functions of the relative motions of the blocks on either side of a fault, so they are predicted by the Euler pole solutions. Additionally, several algorithms in *Oiler* were adapted from the *Blocks* code (written in MATLAB®) described by B. J. Meade & Loveless (2009). However, some fundamental differences exist between *Oiler* and *Blocks*: primarily, *Oiler* does not employ a reference frame or block for the block motions, such that the system solves for the rotations of each block with respect to this reference frame; instead, the relative block motions of pairs of blocks are solved for directly.

The solution strategy used by *Oiler* is to create a set of equations from each velocity observation that can be solved to find the parameters of the Euler pole describing the block rotations that the velocity is associated with. Both GNSS velocities and fault slip rates are considered velocities, and are treated similarly (though not identically) in the inversion. GNSS velocities result from the rotation of the blocks upon which the GNSS stations are located, with respect to some reference block that may or may not be spatially in the model, and are subject to the effects of the earthquake cycles of faults in the model (i.e., interseismic locking) (B. J. Meade & Loveless, 2009; e.g., Savage & Burford, 1973). (Postseismic effects are not included in the model, and coseismic effects are in principle removed from the velocities by the data compilers.) Geologic slip rates, which are generally measured at a single point along a fault, are considered to be velocities resulting from the rotation of one fault block relative to the other fault block.

2.3.1 Preparation of velocity observations

Oiler uses two types of velocity data in the inversion, GNSS velocities and fault slip rates. The GNSS data need little preparation; the east (V_E) and north (V_N) components of the velocities and their uncertainties are used directly, and the vertical component is considered to be zero.

Fault slip rates require some conversion to horizontal velocity vectors in order to be used. If both strike-slip and horizontal shortening or extension (i.e., heave) rates are given, a velocity vector in fault-normal and fault-parallel coordinates is rotated into east and north coordinates, such that the hanging wall is fixed and the footwall moves (vertical strike-slip faults are given a dip of 89° towards an arbitrary side to ensure that the hanging and footwalls are defined). However, typically Quaternary fault slip rate studies only resolve a single component of deformation; in this case, the other component is given a rate of $0 \pm 5 \text{ mm a}^{-1}$.

There is also the issue of converting dip-slip rates to heave rates. B. J. Meade & Loveless (2009) take a simple trigonometric approach, where the dip-slip rate is the heave rate divided by the cosine of the fault dip. However, this leads to very high rates for steeply-dipping faults; it also implies that the dip-slip rate of a fault separating two blocks is always higher than the far-field convergence or divergence rates of the two blocks, and that the far-field vertical velocity difference is non-zero, i.e. the whole of one block uplifts or subsides relative to the other (which may be accurate in some instances but inconsistent for two blocks separated by a fault system that changes dip direction along strike). Instead, *Oiler* considers the dip-slip rate to be equal to the heave rate, which is physically realistic if the footwall undergoes flexural folding at the fault trace; in this case there is no far-field relative uplift or subsidence of the blocks.

To stabilize the solution, synthetic relative velocity data are sampled along fault traces and non-fault block boundaries at regular intervals. These synthetic observations have velocities of $0 \pm 5 \text{ mm a}^{-1}$ for both horizontal velocity components. This essentially damps the results, minimizing seemingly spurious block rotations where data are sparse, noisy or poorly distributed, and increasing the consistency of the kinematics of block-bounding faults in these regions, while leaving the solution to areas with good data coverage and low velocity uncertainties unaffected. A similar strategy is employed in the inversion software by Hammond et al. (2011), used in part of this study area by X. Li et al. (2021).

2.3.2 Solution strategy

A velocity vector $\mathbf{V} = [V_E \ V_N \ V_U = 0]^T$ is related to an Euler pole (a vector in Cartesian coordinates centered at the Earth's center) $\mathbf{\Omega} = [\omega_x \ \omega_y \ \omega_z]^T$ through the equation

$$\mathbf{V} = \mathbf{\Omega} \times \mathbf{RP} \quad (1)$$

where \mathbf{RP} is the Cartesian representation of the coordinates of point P (in latitude and longitude, on the surface of a spherical Earth) (e.g., Chase, 1972; Cox & Hart, 1986).

B. J. Meade & Loveless (2009) transform Equation 1 into a linear equation by using linear operators \mathbf{Pv} and \mathbf{Gb} that are functions of P in place of \mathbf{RP} ; the product of these, \mathbf{G} , is a 3×3 matrix

$$\mathbf{G} = \mathbf{Pv} \cdot \mathbf{Gb} = \begin{bmatrix} G_{11} & G_{12} & G_{13} \\ G_{21} & G_{22} & G_{23} \\ G_{31} & G_{32} & G_{33} \end{bmatrix} \quad (2)$$

Then, Equation 1 can be represented as

$$\mathbf{G} \cdot \mathbf{\Omega} = \mathbf{V}. \quad (3)$$

When the velocity is known but the Euler pole is not, it may be derived by the solving Equation 3 for $\mathbf{\Omega}$:

$$\hat{\mathbf{\Omega}} = \mathbf{G} \setminus \mathbf{V} \quad (4)$$

where the 'backslash' operator \setminus indicates an inverse solution, i.e. $\hat{\mathbf{\Omega}} = (\mathbf{G}^T \mathbf{G})^{-1} \mathbf{G}^T \mathbf{V}$, and the 'hat' symbol $\hat{}$ indicates an estimate.

The system to be solved involves N observations that constrain M poles. A larger system of equations can be constructed to solve for all of the poles simultaneously by grouping the matrices $G_1 \dots G_N$ and $V_1 \dots V_N$ by the pairs of blocks they are associated with. This is represented as the sparse matrix **BigG**, in which groups of \mathbf{G} matrices share the same columns, and each G occupies its own rows. The velocity observation matrices $V_1 \dots V_N$ are similarly stacked vertically as the column vector **BigV**, and the system is solved for the stacked pole vector **Big $\hat{\Omega}$** . When $M > N$ (as in this study), the system is overdetermined and the solution is the least-squares solution.

As an example, a system with six velocity observations $V_1 \dots V_N$ describing the relative motion of four plates A, B, C and D can be solved for the set of poles via the equation

$$\begin{bmatrix} {}^A\mathbf{G}_1^B & \mathbf{0} & \mathbf{0} & \mathbf{0} \\ {}^A\mathbf{G}_2^B & \mathbf{0} & \mathbf{0} & \mathbf{0} \\ \mathbf{0} & {}^B\mathbf{G}_3^C & \mathbf{0} & \mathbf{0} \\ \mathbf{0} & \mathbf{0} & {}^A\mathbf{G}_4^C & \mathbf{0} \\ \mathbf{0} & \mathbf{0} & {}^A\mathbf{G}_5^C & \mathbf{0} \\ \mathbf{0} & \mathbf{0} & \mathbf{0} & {}^B\mathbf{G}_6^D \end{bmatrix} \setminus \begin{bmatrix} {}^A\mathbf{V}_1^B \\ {}^A\mathbf{V}_2^B \\ {}^B\mathbf{V}_3^C \\ {}^A\mathbf{V}_4^C \\ {}^A\mathbf{V}_5^C \\ {}^B\mathbf{V}_6^D \end{bmatrix} = \begin{bmatrix} {}^A\hat{\boldsymbol{\Omega}}^B \\ {}^B\hat{\boldsymbol{\Omega}}^C \\ {}^A\hat{\boldsymbol{\Omega}}^C \\ {}^B\hat{\boldsymbol{\Omega}}^D \end{bmatrix}. \quad (5)$$

Note that the superscripts denote which blocks are involved, and the elements \mathbf{G} , \mathbf{V} and $\boldsymbol{\Omega}$ are matrices and vectors rather than scalars, and $\mathbf{0}$ is a 3×3 matrix of 0s, so **BigG** has 18 rows and 12 columns.

2.3.3 The effects of fault locking on geodetic velocities

GNSS geodetic velocities are the sum of both the long-term block motion (Equation 1) and the effects of interseismic fault locking on other faults in the model. As the standard approach, the effects of fault locking are modeled as an elastic dislocation on each fault equal to, but in the opposite sense of, the long-term fault slip rate.

As the slip rates of the faults are unknowns in the model, they are included in the inversion following methods adapted from B. J. Meade & Loveless (2009). The displacements at each GNSS site given unit slip on each linear segment of each fault, and the displacements from all of the faults associated with each Euler pole are summed and then added to **BigG** in the appropriate location.

As an example, if \mathbf{V}_1 above is a GNSS velocity, and there are two faults in between Blocks A and B as well as three faults between Blocks B and C, then

$${}^A\mathbf{V}_1^B = \mathbf{G}_1^A \hat{\boldsymbol{\Omega}}^B + \sum_i^{n=2} ({}^A\mathbf{F}_i^B(P_1)) + \sum_i^{n=3} ({}^B\mathbf{F}_i^C(P_1)). \quad (6)$$

where ${}^A\mathbf{F}_i^B(P_1)$ is the displacement matrix at point P_1 resulting from unit slip on fault F_i (\mathbf{F} is a 3×3 diagonal matrix). The first sum would be added to the ${}^A\mathbf{G}_1^B$ term in **BigG**, and the second sum would be added to the $\mathbf{0}$ term immediately to the right.

These effects are only applied to GNSS velocities in the model; velocities from fault slip rates, and the synthetic data from fault traces and non-fault block boundaries are unaffected.

Additionally, only mapped fault segments are used to calculate these effects; block boundaries that do not correspond to mapped faults are considered to be creeping. This contrasts with the approach of B. J. Meade & Loveless (2009) but is common in other block modeling systems (J. Elliott & Freymueller, 2020; McCaffrey, 2002). This choice allows non-fault block boundaries (which tend to be inferred rather than known, in geologic mapping parlance) to be drawn more crudely, as the geometry of the boundary does not impact the geodetic velocity observations. There are very few GNSS stations near long non-fault block boundaries in the model, so it is not expected that un-modeled earthquake cycle effects from these boundaries are biasing the model results.

2.3.4 Block velocity closure constraints

Because all velocities and Euler poles are not given with respect to a single reference frame, the system needs additional constraints to satisfy the block velocity closure constraints ${}^A\hat{\boldsymbol{\Omega}}^B + {}^B\hat{\boldsymbol{\Omega}}^C - {}^A\hat{\boldsymbol{\Omega}}^C = 0$ (Chase, 1972; Cox & Hart, 1986). An equality constraint matrix **CM** is constructed from equations describing this relationship for each component of $\hat{\boldsymbol{\Omega}}$, e.g. ${}^A\omega_x^B + {}^B\omega_x^C - {}^A\omega_x^C = 0$. From the example above, the matrix would be

$$\mathbf{CM} = \begin{bmatrix} 1 & 0 & 0 & 1 & 0 & 0 & -1 & 0 & 0 & 0 & 0 & 0 \\ 0 & 1 & 0 & 0 & 1 & 0 & 0 & -1 & 0 & 0 & 0 & 0 \\ 0 & 0 & 1 & 0 & 0 & 1 & 0 & 0 & -1 & 0 & 0 & 0 \end{bmatrix}. \quad (7)$$

${}^B\hat{\boldsymbol{\Omega}}^D$ is not included in the block velocity circuit, so the right-most three columns, corresponding to ${}^B\hat{\boldsymbol{\Omega}}^D$, only contain zeros. **CM** is the left-hand side of the equality constraint, and is matched on the right-hand side by $\mathbf{0}^{\text{CM}}$, which is a column vector of zeroes with the same number of rows as **CM** ($\mathbf{0}^{\text{CM}}$ is a vector of Lagrange multipliers).

In the real model, all block velocity circuits are identified through a breadth-first search of a graph describing which blocks are linked through poles that correspond to a velocity observation. Any three blocks mutually separated by faults form a circuit, as do two blocks separated by a fault that each host GNSS stations in the same reference frame (a non-spatial block in the model). The matrix **CM** has stacked submatrices representing each circuit.

The final component to the inversion is the weight matrix **W**, which weights each observation proportionally to the inverse of the variance associated with each velocity observations.

The matrices **BigG**, **CM** and **W** are concatenated to form a larger system corresponding to an equality constrained, weighted least squares solution (Abdel-Aziz, 2006; Gulliksson & Wedin, 1992):

$$\begin{bmatrix} \mathbf{0} & \mathbf{0} & \mathbf{CM} \\ \mathbf{0} & \mathbf{W} & \mathbf{BigG} \\ \mathbf{CM}^T & \mathbf{BigG}^T & \mathbf{0} \end{bmatrix} \setminus \begin{bmatrix} \mathbf{0}^{CM} \\ \mathbf{BigV} \\ \mathbf{0} \end{bmatrix} = \begin{bmatrix} b_1 \\ b_2 \\ \mathbf{Big\hat{\Omega}} \end{bmatrix}. \quad (8)$$

The system is solved using an LU factorization of the design matrix with algorithms from *UMFPACK* (Davis, 2004). b_1 and b_2 are discarded.

2.3.5 Propagation of uncertainty

Uncertainties in the velocity observations are propagated to the Euler pole solution **Big $\hat{\Omega}$** through Monte Carlo techniques.

Once the design matrix in Equation 8 is factorized, 1000 samples of **BigV** are drawn from the mean and standard deviation of each component of each velocity observation, and the system is solved iteratively. The covariance matrix $\Sigma_{\mathbf{Big\hat{\Omega}}}$ of **Big $\hat{\Omega}$** is then constructed from the 1000 iterations of **Big $\hat{\Omega}$** and the variance of the solution is

$$\sigma^2(\mathbf{Big\hat{\Omega}}) = \frac{\mathbf{e} \cdot \mathbf{e}'}{3N - 3M} \cdot \Sigma_{\mathbf{Big\Omega}}. \quad (9)$$

where **e** is the vector of residuals, and N and M are the numbers of velocity observations and poles, respectively (as above). The covariance matrix for each Euler pole Σ_{Ω} is extracted from the appropriate elements of $\sigma^2(\mathbf{Big\hat{\Omega}})$.

The uncertainties in the Euler poles are then propagated to the predicted velocities, and then finally to the faults. The covariance matrix for any velocity vector **V** is calculated as $\Sigma_{\mathbf{V}} = \mathbf{G} \cdot \Sigma_{\Omega} \cdot \mathbf{G}'$.

It should be noted that the uncertainties calculated here are only those resulting from the formal uncertainties on the velocity observations. The uncertainties that are related to uncertainties in the model construction (i.e., the location of faults or how the faults are connected to form blocks) may be much larger. It is possible that they may be estimated through the incorporation of branches in a logic tree with nodes corresponding to different, mutually exclusive block geometries and topologies, but this is not done in this study.

3 Results and Regional Kinematics

3.1 Evaluation of model fits

In general, the data are fit quite well by the model. Considering the combined geologic slip rate and GNSS velocity dataset, the predicted velocity components (e.g., V_E , not the whole horizontal vector) have a median misfit of 0.5 mm a⁻¹, and a mean misfit of 0.9 mm a⁻¹. The root mean square error is 2.1 mm a⁻¹.

3.2 Orogen-scale transfer faults

The great strike-slip faults in the Indo-Asian collision zone are first-order orogenic features, with lengths and slip rates surpassed only by the Main Himalayan Thrust. The various geodynamic roles played by these faults has been discussed at length (e.g., Peltzer & Tapponnier, 1988). However, what is less discussed is the role of these structures within the broader network of faults that accommodates strain throughout the orogen.

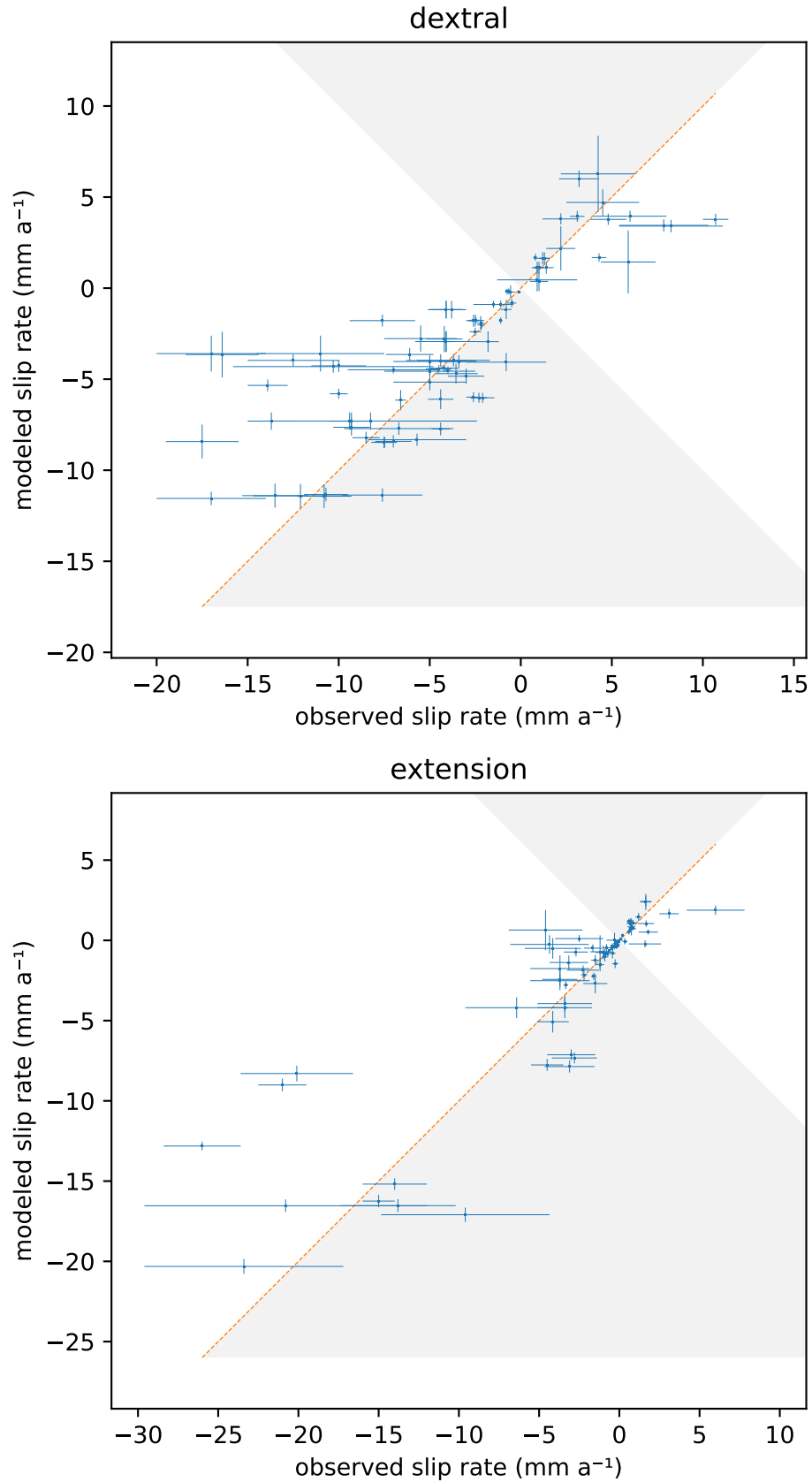


Figure 3: Comparison of modeled and observed geologic slip rates. Negative dextral rates are sinistral, and negative extension rates are contractional. Uncertainties are $1-\sigma$. Regions of the figures shown in grey are where modeled slip rates are higher than observed rates, and areas in white are where modeled rates are lower than observed rates.

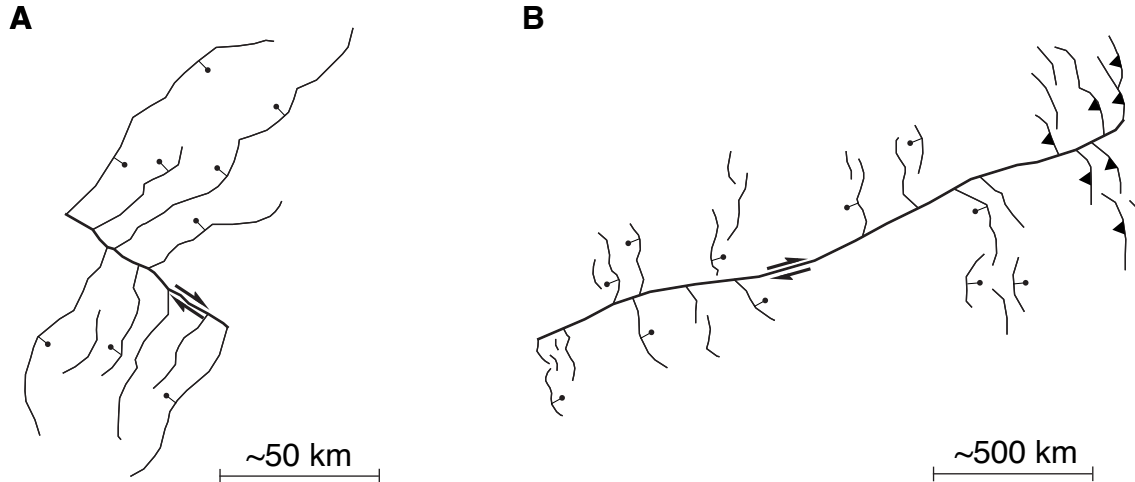


Figure 4: Types of transfer faults. **A:** Classically-defined transfer fault (Faulds & Varga, 1998; Gibbs, 1984). Transfer fault (thick line) is subordinate to larger fault network, and accommodates minor changes in the location and/or magnitude of faulting. **B:** Orogen-scale transfer fault. Transfer fault (thick line) aggregates and redistributes slip from many smaller fault networks along strike, and may connect extensional to contractional domains. Note change in scale.

These strike-slip aggregate, concentrate and redistribute strain from slower, more distributed extensional and contractional fault systems throughout the orogen. The subordinate fault systems feed slip into (or out of) the great strike-slip faults, similarly to how residential or surface streets feed car traffic into or out of highways. This leads to substantial along-strike slip rate changes, with a general pattern of low rates at the ends of the fault and high rates in the middle (Figure 5), unless the faults link at one end with a major dip-slip fault system, in which case the high rates may be maintained until that junction (such as the Talas-Ferghana and Haiyuan faults).

Structurally, the great strike-slip fault systems function as orogen-scale transfer faults (Faulds & Varga, 1998; Gibbs, 1984), but at a much greater scale than the faults labeled as such in the literature, and as the primary, rather than secondary, structures in the fault network. In both cases, transfer faults accommodate differential extension or contraction of crust on either (or both) sides of the fault, and transfer strain along strike to other linked fault systems. However, the orogen-scale transfer faults are longer than the extensional faults that feed in, and they link up many smaller structures all along their length. Furthermore, many of them (including the Karakoram, Altyn Tagh, Kunlun, and Haiyuan fault systems) transfer strain from extensional to contractional domains.

The recognition that some of these great strike-slip faults transfer strain to linked extensional or contractional systems is not new (e.g., Burchfiel et al., 1989; Cowgill et al., 2003; Murphy et al., 2002; Styron et al., 2011; Yin et al., 2008). What is more novel is the observation that the strike-slip faults are dominant in terms of their lengths and slip rates to the linked extensional and contractional systems, they serve as major conduits of strain in the orogen, and that their slip rates change constantly along strike as the smaller linked fault networks feed slip in or out.

3.3 Tien Shan

The Tien Shan is the northwesternmost deforming zone in the Indo-Asian collision zone. The mountain system undergoes N-S contraction through slip on E-striking reverse faults distributed throughout (e.g., Thompson et al., 2002), leading to a contractional basin and range physiography. The region is bound to the southwest by the Pamir, farther east by the rigid Tarim Basin, and in the north by the Kazakh shield, which is geodetically part of stable Eurasia. GNSS velocities in the northern margin of the Pamir and western Tarim Basin have northward components of $\sim 20 \text{ mm a}^{-1}$, which decreases to about half of that in the eastern Tarim basin (Figure 6); this is the shortening budget of the Tien Shan.

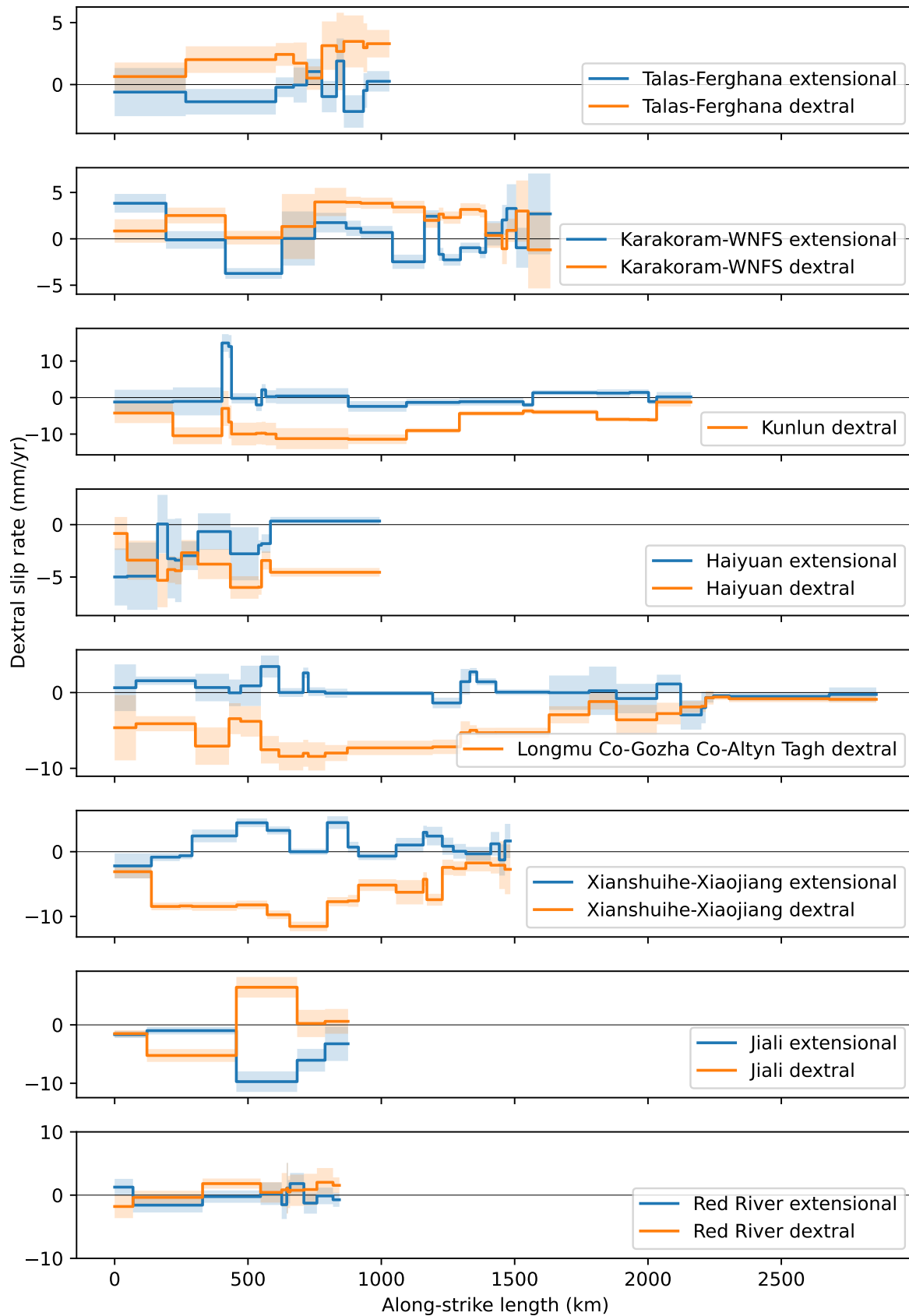


Figure 5: Slip rates for major strike-slip fault systems along strike. Dextral rates are in orange (negative rates are sinistral) and extensional rates are in blue (negative rates are contraction). 2- σ uncertainties are shown as pale envelopes around rates.

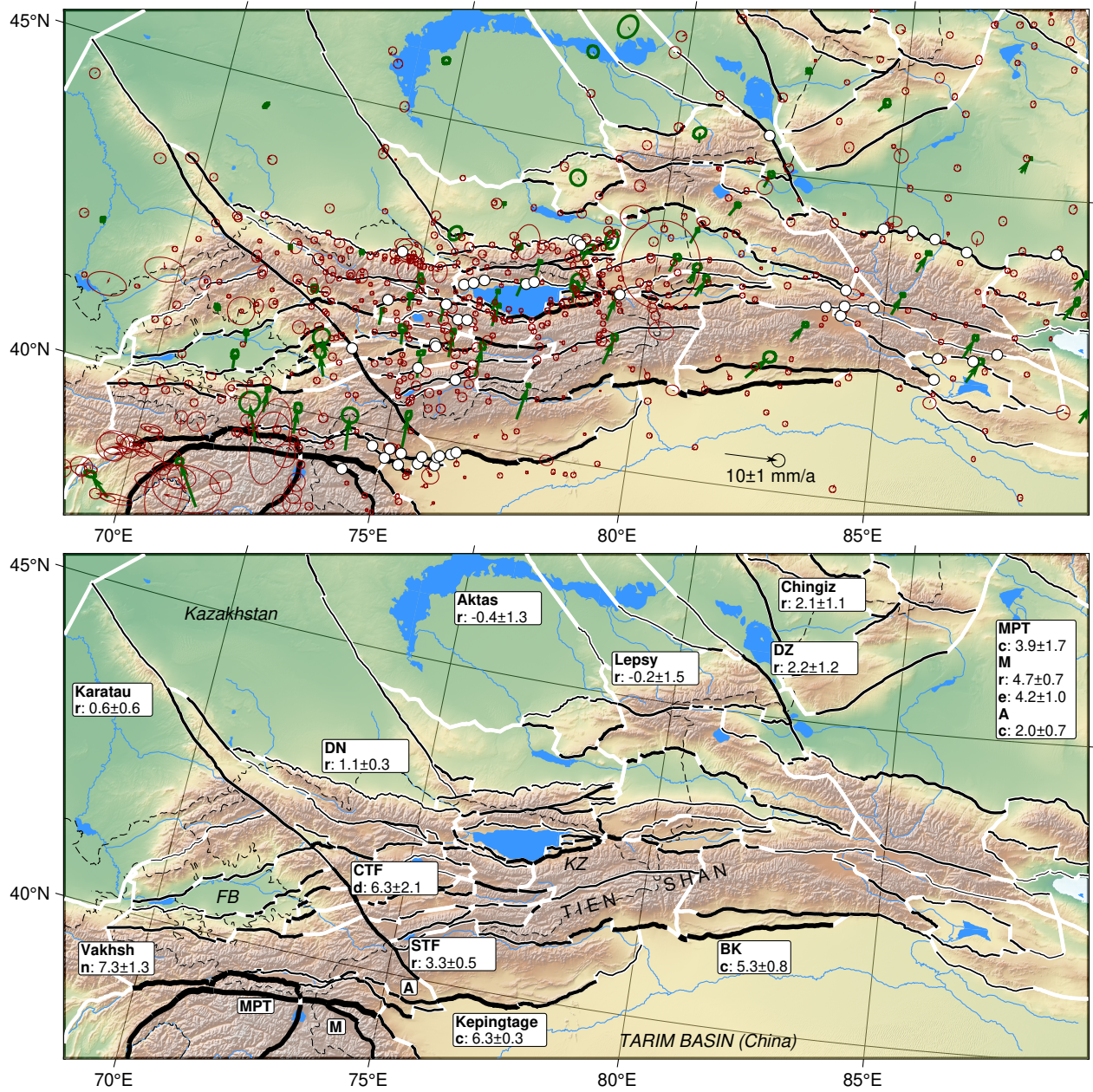


Figure 6: Active faults of the western Tien Shan. In this and subsequent maps, block velocities with respect to stable Eurasia are shown in green. GNSS velocity residuals are shown in red. Uncertainty ellipses are 2σ . Neither the observed nor predicted GNSS velocities are shown for clarity. Block boundaries are shown in white. Faults are shown in black, with line weights proportional to the estimated slip rate. National borders are shown with a thin dashed line. Physiographic names are in all capital letters, while country names are in lowercase. KZ = Kyrgyzstan. FB = Ferghana basin. STF = southern Talas-Ferghana fault. CTF = central Talas-Ferghana fault. MPT = Main Pamir Thrust. M = Muji fault. A = Atushi-Talanghe-Mutule anticline. BK = Baicheng-Kuche fault. DZ = Dzhungarian fault. DN = Dzhalaïr-Naiman fault.

The distributed nature of deformation is evident in the contraction rates for individual structures (which range from $\sim 0.3\text{--}4\text{ mm a}^{-1}$, Figure 6), and is well constrained by the dense coverage of both GNSS data and neotectonic slip rate measurements. As the contraction rates across the Tien Shan decrease by half to the east, the number of structures accommodating the shortening decreases, while the typical shortening rate on a given structure does not.

The highest shortening rates are found along the southern frontal thrusts, where the Tien Shan overrides the Tarim Basin; see Section 3.4.1.

The faults of the eastern Tien Shan have similar kinematics but diminished rates compared to those farther west. Contraction across the far eastern Tien Shan sums to under 2 mm a^{-1} , similar Quaternary rates by Charreau et al. (2017). More rapid shortening is accommodated on mostly blind thrusts at northeastern range front, at $2.2 \pm 0.2\text{ mm a}^{-1}$, in agreement with geologic estimates (e.g., Lu et al., 2019).

The modeling in this study also indicates that the Tien Shan extends east-west, as evident in the increasing eastward velocity of GNSS data with increasing longitude. However, few structures are found that clearly accommodate this extension.

3.3.1 NW-striking dextral faults

Several major NW-striking dextral faults cut through the Kazakh shield into the northern Tien Shan. The westernmost is the 1000 km long Talas-Ferghana fault, which bisects the range. The kinematic role and slip rate on the Talas-Ferghana fault has been contested through the decades. The earliest modern neotectonic slip rate estimates for the fault are $\sim 1\text{ cm a}^{-1}$ (Burtman et al., 1996), in line with a few more modern estimates (e.g., Rust et al., 2018). However, geodetic studies (Metzger et al., 2020; e.g., S. Mohadjer et al., 2010; Zubovich et al., 2010) limit the slip rates to a few mm a^{-1} , as do other geologic studies. Rizza et al. (2019), for example, find low rates and demonstrate that the radiocarbon dates used to infer the age of undeformed stream channels on the fault may simply record the date of the last major earthquake.

I find rates consistent with the lower set of estimates; rates are zero within uncertainty (sinistral at $0.6 \pm 0.6\text{ mm a}^{-1}$) at the northwestern end of the fault, also known as the Karatau fault (M. B. Allen et al., 2001) and increase southeastward to $6.3 \pm 2.1\text{ mm a}^{-1}$ of dextral slip. Dextral rate estimates of $\sim 1\text{ cm a}^{-1}$ are inconsistent with the regional fault kinematics, as they would require most of the shortening in the Tien Shan to the east of the fault to be accommodated along the southern thrusts bordering the Tarim Basin, while to the west of the fault, the shortening would have to be accommodated north of the Ferghana basin in the Chaktal ranges; this is not supported by either the neotectonic slip rates or geodetic data within the Tien Shan demonstrating distributed shortening.

Parallel strike-slip faults to the east terminate in the northern margins of the Tien Shan rather than in the interior of the ranges (e.g., Tapponnier & Molnar, 1979). Slip rates on the Dhzalair-Naiman, Aktas, and Lepsy faults all have rates in this solution at or below 1 mm a^{-1} , though they have a clear topographic expression and yield evidence for large-magnitude if infrequent Holocene seismicity (e.g., Campbell et al., 2015).

Farther to the east, the Dzhungarian fault cuts through northern Tien Shan, bifurcating the Ala-Tau and Kertau ranges at the Dzhungarian Gate, before merging with thrusts south of the Dzhungarian basin. I find that the dextral slip rate increases from north to south, with a rate of $2.2 \pm 1.2\text{ mm a}^{-1}$ in the Dzhungarian Gate, in agreement with the rate of 2.2 ± 0.8 found by Campbell et al. (2013).

The Ferghana Valley is an intermontaine basin in the western Tien Shan, north of the Pamir and west of the Talas-Ferghana fault. The valley holds 12-15 million people (Borthakur, 2017), and is bound on the northern and southern margins by active thrusts; as such, it is the most populated region fully encapsulated by the orogen and a major source of seismic risk. The results of this study yield slip rates of $\sim 0.5\text{--}3\text{ mm a}^{-1}$ on the thrusts surrounding the basin.

3.4 Pamir

The Pamir converges with the Alai ranges of the southeastern Tian Shan at the Alai Valley, the western margin of the Tarim basin to the east, and the northeastern margin of the Tajik basin to the west [Figure 6]. North-south shortening in this convergence zone is very rapid, with $3.9 \pm 1.7\text{ mm a}^{-1}$ on the Main Pamir Thrust, $6.5 \pm 2.1\text{ mm a}^{-1}$ on the Pamir Frontal Thrust, and $0.2 \pm 0.8\text{ mm a}^{-1}$ on the Vakhsh fault bordering the northern Alai valley.

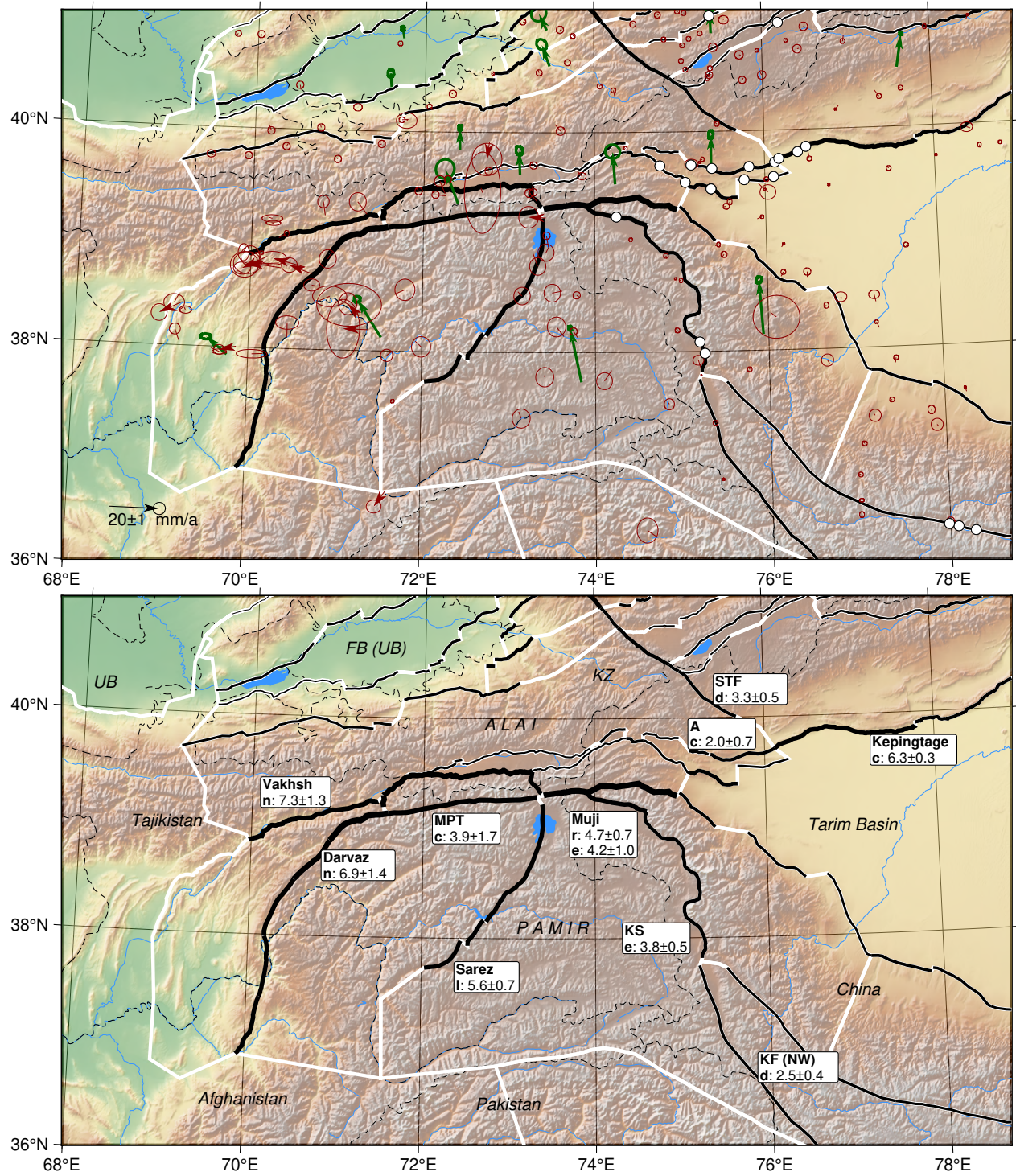


Figure 7: Fault and block geometry for the Pamir and surroundings. STF = Southern Talas-Ferghana fault. A = Atushi-Telange-Mutule anticline. KS = Kongur Shan. KF = Karakoram fault. MPT = Main Pamir Thrust.

East–west extension is also relatively rapid, but decreases to the south. The Kongur Shan normal fault extends at $3.8 \pm 0.5 \text{ mm a}^{-1}$, a bit higher than the geologic rates of 1.65 ± 0.35 extension by M.-L. Chevalier et al. (2015), and the kinematically-linked Muji fault extends at $4.2 \pm 1.0 \text{ mm a}^{-1}$, with dextral slip of $4.7 \pm 0.7 \text{ mm a}^{-1}$, consistent with the dextral rate from M.-L. Chevalier et al. (2011). The NE-striking Sarez fault cuts through the center of the Pamir, separating the eastern and western blocks at $5.6 \pm 0.7 \text{ mm a}^{-1}$ sinistral slip in the south, which changes to about half that sinistral slip rate and an extension rate of $4.0 \pm 1.0 \text{ mm a}^{-1}$ in the north where it meets the Main Pamir Thrust.

The northeast corner of the Tajik basin is bound in the east by the Darvaz fault, where it underthrusts the Pamir, and in the north by the Vakhsh fault, where it underthrusts the Alai ranges (e.g., Metzger et al., 2020). Slip rates near the Alai valley are high, with $7.3 \pm 1.3 \text{ mm}$ dextral-reverse faulting on the Vakhsh fault matched by $6.9 \pm 1.4 \text{ mm a}^{-1}$ sinistral-reverse slip along the Darvaz fault. This is broadly consistent with the tectonic escape model proposed by Metzger et al. (2020) though our block modeling indicates that the Euler pole between the Tajik basin and the Pamir is relatively close by to the southeast, so that relative deformation rates decrease to the southwest.

3.4.1 Western Tarim Basin

The western Tarim Basin is bound by the Tien Shan to the north and the Pamir to the south. The thrusting in the Tarim foreland is somewhat complex, and the mapping here is more of a simplification than in other locations. Nonetheless, the major structures are resolved. A major structure in the region is the Atushi-Talanghe-Mutule anticline (here considered a north-dipping thrust merging into the Tien Shan) which has a shortening rate of $2.0 \pm 0.7 \text{ mm/y}$ in the west (somewhat consistent with the geologic rates by Scharer et al. (2004) and Thompson Jobe et al. (2017)). Rates increase to the east along the Kepingtage anticline, with $6.3 \pm 0.3 \text{ mm a}^{-1}$ shortening. High rates are maintained eastward for several hundred kilometers along the Baicheng-Kuche fault, with $5.3 \pm 0.8 \text{ mm a}^{-1}$ contraction, and then decrease farther east. Smaller folds and thrusts creating the foothills of the Pamir have shortening rates up to 2 mm a^{-1} .

3.5 Himalaya

Much of the convergence between India and Eurasia is accommodated on the Main Himalayan Thrust, which is the plate boundary fault separating the two continents (e.g., Ader et al., 2012; P Kapp & DeCelles, 2019). Though the Himalayan wedge is constructed of many stacked nappes separated by thrusts that have been active at various times throughout the Cenozoic (e.g., P Kapp & DeCelles, 2019), most or all of the slip on the Main Himalayan Thrust is transferred to the Main Frontal Thrust at the very tip of the wedge and perhaps the Main Boundary Thrust that daylights a few tens of km towards the hinterland; these are uniformly interpreted to merge at depth. A significant body of research holds that additional out of sequence thrusts, as well as thrust-parallel normal faults, may be active in the interior of the Himalayan wedge, most prominently the Main Central Thrust and South Tibetan Detachment in Nepal that separate the High Himalaya from the Lesser Himalaya below and Tethyan Himalaya above (e.g., Hodges et al., 2004).

This study considers the Main Frontal Thrust and Main Himalayan Thrust to be one and the same, dipping at 10° (Ader et al., 2012), and does not include the Main Boundary Thrust, Main Central thrust, or other splays, with the exception of the Western Nepal Fault System described below. This simplification is due to the complexity of geodetic block modeling of vertically stacked splay faults that merge at depth. It is hoped that future work more focused on the Himalaya, rather than the entire orogen, may incorporate more structural complexity.

3.5.1 Main Frontal Thrust

Estimates of slip rates on the Main Himalayan Thrust range between $\sim 10\text{--}20 \text{ mm a}^{-1}$, or about a third to a half of the total Indo-Asian convergence. Many authors consider that rates change along strike, increasing from the northwest, with geologic rates from $9 \pm 7\text{--}13 \text{ mm a}^{-1}$ (Kumar et al., 2001), to over 20 mm a^{-1} in the eastern Himalaya (Burgess et al., 2012). These results broadly replicate that trend. The results for the northwest Himalaya (immediately south of the Thakkhola graben in central-western Nepal all the way to Pakistan) yield shortening rates between $13\text{--}16 \text{ mm a}^{-1}$, all within uncertainty of geologic rates (Kumar et al., 2001; Powers et al., 1998; Wesnousky et al., 1999). In the central Himalaya, between the Thakkhola graben and the Yadong rift, the shortening rates resolved here are slightly lower, $9\text{--}13 \text{ mm a}^{-1}$, which is a much poorer fit with geologic rates of $20\text{--}26 \text{ mm a}^{-1}$.

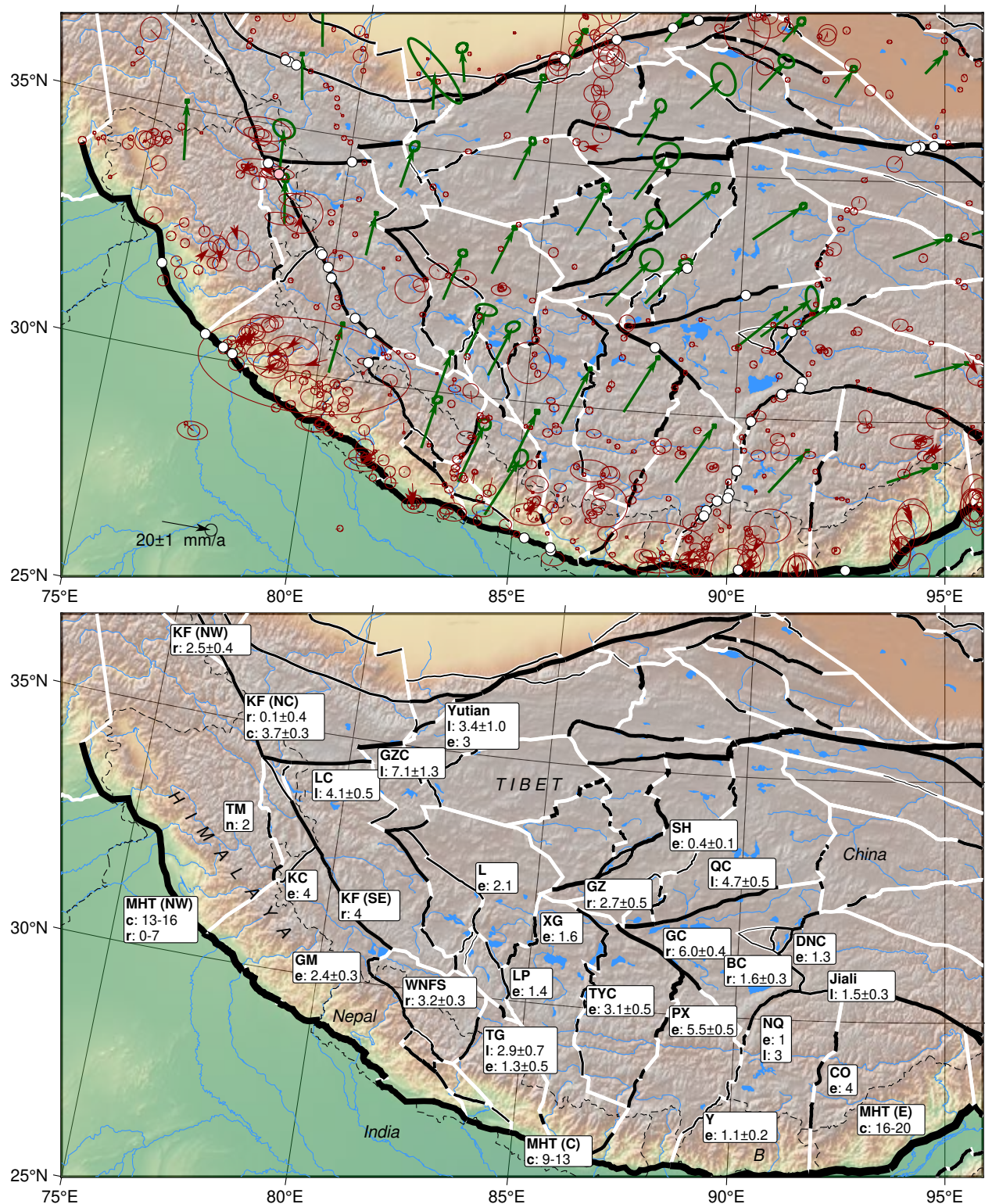


Figure 8: Himalaya and Tibet. MHT = Main Himalayan Thrust. WNFS = Western Nepal Fault System. TM = Tso Morari fault. KC = Kaurik–Chango fault. GM = Gurla Mandhata fault. TG = Thakkhola Graben. Y = Yadong rift. KF = Karakoram fault. L = Lunggar rift. LP = Lopukangri rift. XG = Xiangjiang rift. TYC = Tangra Yum Co rift. GZ = Garze fault. GC = Gyaring Co fault. PX = Pum Qu–Xainza rift. NQ = Nyainqentanghla fault. CO = Cona–Oiga rift. EHS = Eastern Himalaya Syntaxis. BC = Beng Co fault. DNC = Dong Co fault. J = Jiali fault LC = Longmu Co fault. GZC = Gozha Co fault. SH = Shuang Hu graben. QX = Qixiang Co fault. ATF = Altyn Tagh fault.

(Bollinger et al., 2014; Lavé & Avouac, 2000), as well as with many geodetic rates, also around 20 mm a^{-1} (Ader et al., 2012; Stevens & Avouac, 2015). This discrepancy diminishes to the east, where I find contraction rates of $16\text{--}20 \text{ mm a}^{-1}$, in agreement with the geologic rates by Burgess et al. (2012) and Berthet et al. (2014).

Strike-slip deformation on the Main Himalayan Thrust is generally dextral in the northwest and central Himalaya, replicating observations from geology (Malik et al., 2015; Malik & Nakata, 2003; Shah et al., 2021) and geodesy (Jouanne et al., 2004; Kundu et al., 2014; Stevens & Avouac, 2015), and sinistral in the east, but rates vary greatly segment to segment. The primary reason for the short-wavelength variability is moderate variations in the strike of adjacent segments, but some of it is likely due to larger-scale kinematics. In either case, it is unclear exactly how and where strike-slip deformation is accommodated. Focal mechanisms and coseismic finite fault models in the Himalaya are well partitioned into relatively pure dip slip on the thrusts and strike slip on structures in the hanging wall (e.g., Bendick et al., 2007; Styron et al., 2011), consistent with plate convergence zones globally (e.g., Jarrard, 1986; McCaffrey, 1994). However, the broader-scale oblique partitioning models consider the Karakoram fault to be the locus of strike-slip deformation and backstop of a translating forearc sliver (McCaffrey & Nabelek, 1998; Styron et al., 2011); this analysis shows that the dextral slip rates in on the northwestern Main Himalayan Thrust are as great or greater than on the Karakoram fault, up to 7 mm a^{-1} .

The discrepancy between coseismic evidence for slip partitioning and interseismic model indicating oblique strain accumulation is difficult to resolve. Geologic observations of dextral slip on splay faults within the frontal Himalayan wedge exist (Malik et al., 2015; Malik & Nakata, 2003; Nakata, 1989; Shah et al., 2021; Silver et al., 2015) but most of these faults are within a few tens of kilometers of the frontal thrusts, and likely merge with the Main Himalayan Thrust at fairly shallow depths, well within its interseismically locked and putatively seismogenic boundaries; given a dip of around 10° , substantially oblique slip during a major earthquake on the Main Himalayan Thrust would be very surprising.

3.5.2 Intra-Himalayan faults

Several fault systems cut into or through the Himalaya. These are typically normal or oblique-normal fault systems that are linked with rifts in southern Tibet (e.g., Armijo et al., 1986; Styron et al., 2011), and divide the Himalaya into blocks that move with different velocity vectors relative to southern Tibet (McCaffrey & Nabelek, 1998; Styron et al., 2011).

In the west, the Tso Moriri rift has about 2 mm a^{-1} of dextral-normal slip, while the neighboring Kaurik-Chango fault bounding the western Leo Parghil dome has 4 mm a^{-1} of normal slip.

The next major intra-Himalayan fault system to the southeast is the Gurla Mandhata rift, which extends at $2.4 \pm 0.3 \text{ mm a}^{-1}$. The Western Nepal Fault System (Murphy et al., 2014) is thought to represent the propagation of slip on the Karakoram Fault southeastward through the Gurla Mandhata detachment to a set of ESE-striking faults that approach or merge with the Main Boundary Thrust (a splay fault of the Main Himalayan Thrust north of the Main Frontal Thrust). I find consistent dextral slip, with minor extension or contraction as fault orientation changes; a rate of 3.2 ± 0.3 from the center of the fault is typical.

The central and eastern Himalaya has several N-trending rifts. The most well-known of these are the Thakkhola graben in western Nepal and the Yadong rift on the Tibet-Bhutan border. The Thakkhola graben resolves here as sinistral ($2.9 \pm 0.7 \text{ mm a}^{-1}$), with minor extension ($1.3 \pm 0.5 \text{ mm a}^{-1}$).

Extension along the Yadong rift is consistent from $1.1 \pm 0.2 \text{ mm a}^{-1}$ in the Himalaya zone on the Bhutan border to $1.2 \pm 0.1 \text{ mm a}^{-1}$ 200 km farther north. These values are compatible with many of the geologic data which yield rates of about $0.5\text{--}2 \text{ mm a}^{-1}$ (inclusive of uncertainty) (Ha et al., 2019; S. Wang et al., 2020).

A few other faults are mapped here in the central Himalaya, where the boundaries between south Tibetan blocks extend south to meet the Main Frontal Thrust. Faults have been drawn where the topography is suggestive, though to my knowledge these are not described in the literature. These slip at a few mm per year, with variable kinematics.

The broader pattern of Himalayan block motions, manifest but perhaps not obvious in the fault slip rates, is that the range is undergoing ‘orocline unbending’, where the broad curvature of the range in map pattern is decreasing. Essentially, the center of the range (central Nepal through Bhutan) is moving faster to the north-northeast than the

eastern and northwestern flanks of the range. This results in sinistral slip along the NNE-striking intra-Himalayan rifts of western Nepal and India (the Thakkhola, Gurla Mandhata and Leo Parghil rifts).

3.6 Central Tibet

Faulting in central Tibet is dominated by east-west extension on ~N-striking normal faults, dextral-oblique slip on NW-striking faults, and sinistral-oblique slip on NE-striking faults (e.g., Taylor et al., 2003). Geodetic and geologic data are sparse in the region, particularly in the north. As a consequence, block motions here are not always well constrained, and in some cases the blocks likely encapsulate faults with slip rates high enough that they would separate blocks in better-studied regions. Regardless, for most of the faults in central Tibet, this study provides the first present-day slip rate estimates, and it is hoped that they are valuable even if they are less well constrained than elsewhere.

3.6.1 Karakoram fault

The Karakoram fault is a well-known and well-studied ~1000 km long dextral fault that separates the northwestern Himalaya from western Tibet (Figure 8). Like the Kunlun and Altyn Tagh faults, the Karakoram fault has been estimated to be slipping at a wide range of rates, and therefore to occupy different (but generally important) roles in various hypotheses for the geodynamics of Himalayan and Tibetan deformation (Styron et al., 2011).

The crust to either side of the Karakoram fault is broken into multiple blocks in the model, and consequently the slip rate on the Karakoram fault varies substantially along strike (Figure 5). The northernmost Karakoram fault section separates the southeastern Pamir from extreme northwestern Tibet, and slips dextrally at 2.5 ± 0.4 mm a⁻¹, with a very minor component of extension. However, south of the block boundary between the Pamir and the northwesternmost Himalaya, the strike-slip component decreases to 0.1 ± 0.4 mm a⁻¹, while the fault system hosts 3.7 ± 0.3 mm a⁻¹ of contraction; this is consistent with work by Robinson (2009) suggesting little to no late Quaternary strike-slip faulting on this section, and the contraction resolved on the fault zone may be linked to the extremely high peaks of the Karakoram range (including K2) adjacent to the fault. As postulated by Robinson (2009), dextral slip resumes farther southeast after the junction with the Longmu Co fault (Section 3.6.3).

The central and southeastern Karakoram fault has dextral slip rates generally consistent at around 4 mm a⁻¹; these are slower than many of the geologic rates of about 2–8 mm a⁻¹ (Brown, 2005; M.-L. Chevalier et al., 2005; M.-L. Chevalier et al., 2012; M.-L. Chevalier, Van der Woerd, et al., 2016) but do match the lower set of rates.

3.6.2 Southern Tibetan rifts and dextral faults

Southern Tibet hosts a set of clearly-defined, regularly-spaced N-trending rifts that show clear kinematic linkages with ESE-striking dextral faults (e.g., Armijo et al., 1989). The dextral faults typically have conjugate NE-striking sinistral-normal faults (Taylor et al., 2003).

The westernmost of the rift and dextral fault systems is a pair of parallel, closely-spaced dextral faults that link with the Lunggar Rift (P. Kapp et al., 2008) and the Yari rift to the west. Each of these systems slips at about 0.9–2.1 mm a⁻¹ (varying along strike). These rates are consistent with geodetic work by Taylor & Peltzer (2006) and H. Wang et al. (2019) on the strike-slip faults, and extension rates over the Pliocene through present on the North Lunggar rift from thermochronology (Sundell et al., 2013), though this work predicts much slower rates than the Pliocene to present rates for the South Lunggar rift (Styron et al., 2013). These faults may be linked to the Lopukangri (Sanchez et al., 2013) and Xiagangjiang (Volkmer et al., 2007) rifts to the east, which show similar rates of extension.

The next system to the east is the Tangra Yum Co rift and linked Garze dextral fault, with respective extension and right-slip rates of 3.1 ± 0.5 mm a⁻¹ and 2.7 ± 0.5 mm a⁻¹. Notably, H. Wang et al. (2019) detected essentially no decadal strain accumulation across the Garze fault.

The Gyaring Co dextral fault and Pum Qu–Xainza rift lies further east, and is substantially faster than the neighboring rifts. The Gyaring Co fault, west of the junction with the Pum Qu–Xainza rift, shows 6.0 ± 0.4 mm a⁻¹ of dextral slip, consistent with previous work (Shi et al., 2014; Taylor & Peltzer, 2006; H. Wang et al., 2019). The linked

northern Pum Qu–Xainza rift extends at $5.5 \pm 0.5 \text{ mm a}^{-1}$, but the extension rate decreases to the south to near zero close to the northern Himalaya.

The central and northern Yadong–Gulu rift, including the Damxung and Nyainqentanghla grabens, extends at more slowly the other rifts ($\sim 1 \text{ mm a}^{-1}$), but similar to geologic estimates (M.-L. Chevalier et al., 2020), and has a component of sinistral slip of $\sim 3 \text{ mm a}^{-1}$. Sinistral slip has long been recognized based on geologic evidence (J. L. D. Kapp et al., 2005), though rates have remained geologically unquantified.

The easternmost rift, the Cona–Oiga Rift (e.g., Yang Wang et al., 2019) is less geomorphically developed than the other rifts (i.e., the rift basin is not as wide or continuous along strike, and the footwall is not as broad or as elevated above the basin), but has a rapid extension rate, about 4 mm a^{-1} . This rates are linked to the increase in eastward motion of Tibetan crust near the Eastern Himalayan Syntaxis and Eastern Tibet. Though the results estimated here are high, they are compatible with 3 Ma to present rates based on thermochronology of $1.6\text{--}3.8 \text{ mm a}^{-1}$ (Bian et al., 2020); these authors also suggest a late Pliocene initiation of extension, which may explain why the rift is not as developed as its neighbors to the west.

The Beng Co–Dong Co fault system is a small conjugate strike-slip system with some internal N-striking normal faults north of the Gulu Rift. The Beng Co fault, the southern, SE-striking, dextral fault is well known for hosting a very large ($M \approx 8$) earthquake in 1951. Early slip rate estimates are $10\text{--}20 \text{ mm a}^{-1}$ (Armijo et al., 1989; Wu et al., 1992), though more recent geologic and geodetic rates are $1\text{--}4 \text{ mm a}^{-1}$ (Garthwaite et al., 2013; Hollingsworth et al., 2010). Here, we estimate dextral slip rates of $1.6 \pm 0.3 \text{ mm a}^{-1}$ on the southeastern section of the Beng Co fault, where the 1951 rupture is prominent in the landscape, and much slower slip farther northeast, where no rupture is visible; the fault hosts a southeastward increasing normal component, as well. The unnamed conjugate sinistral fault to the north slips at up to $3.7 \pm 0.3 \text{ mm a}^{-1}$, also slower in the west. Combined extension across the Daru Co and Dong Co normal faults in between the strike-slip faults is about 2 mm a^{-1} , consistent with geologic rates (K. Li et al., 2019). However, all of these rates are informed by very few data, and localized studies or increased geodetic coverage could refine these values quite a bit.

The Jiali fault is mapped here with its western terminus where the southern end of the north-striking Gulu Rift meets the Damxung/ Nyainqentanghla rift. The Jiali Fault continues east, separating the southern Tibetan and Himalayan blocks from those of east-central Tibet, before splitting into several other faults north of the Eastern Himalayan Syntaxis. Though the Jiali fault has long been considered a dextral fault (e.g., Armijo et al., 1989), the western Jiali fault resolves as sinistral, similar to (and in continuation of) the northern Damxung rift, with sinistral slip of $1.5 \pm 0.3 \text{ mm a}^{-1}$. Though signs of Quaternary surface faulting are evident along the trace, no clear kinematic indicators were observed, and those noted by Armijo et al. (1989) were equivocal in the satellite imagery. The sinistral component decreases eastward, and the splaying faults to its east show rapid dextral slip (as discussed in Section 3.9.3).

The decrease in left slip rate on the Jiali fault is met by an increasing component of contraction across the fault zone (Figure 5), exceeding 1 cm a^{-1} east of the Eastern Himalayan Syntaxis, where it is accommodated on two structures, the Puqu and Parlung faults (Section 3.9.3). The terrain surrounding the eastern Jiali fault is high even by South Tibetan standards, with many peaks between 6–7 km, and the high-altitude areas are much more broad than the similarly high rift-flank uplifts farther west. This suggests that N-S contraction in the region may be somewhat distributed. Discrete active reverse faults have not been mapped to my knowledge, but the zone is easily among the world's most rugged and inaccessible.

3.6.3 Central Tibetan sinistral faults and associated normal faults

Central Tibet deforms through slip on NE-striking sinistral faults that are typically conjugates to dextral faults in southern Tibet (Taylor et al., 2003). These sinistral faults are commonly transtensive, with small extensional stepovers, rather than linking to large, well-defined rift systems as in southern Tibet.

The westernmost of these faults is the Longmu Co–Gozha Co fault system (Avouac & Tapponnier, 1993; M.-L. Chevalier et al., 2017), which links with the Yutian rift and Ashikule stepover (Bie & Ryder, 2014) before merging with the Altyn Tagh fault system (Section 3.7.2). This study finds that the Longmu Co fault (in the southwest) has a sinistral slip rate of $4.1 \pm 0.5 \text{ mm a}^{-1}$, in line with geologic estimates (M.-L. Chevalier et al., 2017), and the Gozha Co fault farther northeast has a sinistral rate of $7.1 \pm 1.2 \text{ mm a}^{-1}$. The sinistral rate drops back down to 3.4

$\pm 1.0 \text{ mm a}^{-1}$ with about 3 mm a^{-1} extension across the Yutian rift. This sinistral shear is transferred onto the Altyn Tagh fault to the northeast.

Spread over a thousand kilometers east of the Longmu Co–Gozha Co faults, several sets of E– to NE–striking sinistral faults (associated with minor NW– to NE–striking normal faults) accommodate E–W extension of Central Tibet. Almost all of them slip at about $2.5\text{--}3.5 \text{ mm a}^{-1}$, with some component of extension as well. The relative magnitudes of strike slip and extension vary substantially with fault strike (faults striking N or NW have the fastest extension and slowest strike-slip). The only Quaternary fault slip rate in the region is on a fault in the Shuang Hu graben; there, Blisniuk & Sharp (2003) find extension rates of about 0.1 mm a^{-1} on a single fault trace, which is a fraction of the $0.4 \pm 0.1 \text{ mm a}^{-1}$ extension found here across the entire rift at that location.

The longest and fastest-slipping of the NE-striking faults is a 450 km long fault called the Qixiang Co (or Kyebxiang Co) fault, which is a conjugate of the Gyaring Co fault. The inversion here yields a sinistral slip rate of $4.7 \pm 0.6 \text{ mm a}^{-1}$, consistent with the Holocene rate of 3.6 ± 1.2 found by K. Li et al. (2018).

Generally, the blocks in north-central Tibet fan outward, with east-west extension increasing northward. The northern margin of this fan is the western Kunlun fault system, which acts here in a transfer capacity, increasing in slip rate to the east as extension between north-central Tibetan blocks is absorbed.

3.6.4 Tanggula Shan and central–eastern Tibet

An area with great uncertainty in the block and fault geometry exists in central-eastern Tibet. The western part of this region encompasses the Tanggula Shan, an isolated northwest-southeast trending mountain range of moderate relief characterized by northeast-striking normal faults cutting the range into sections along its length, that do not visibly extend into the relatively lower terrain to the north and south of the range (Styron et al., 2010; Taylor & Yin, 2009). This geometry is not unique in the plateau; the many small rifts in the Gangdese Shan in southern Tibet show a similar pattern of extension limited to high terrain. It is difficult to accommodate this type of fault geometry into a block model, and indeed to understand how extension within an isolated area (such as a mountain range) may be accommodated in surrounding regions that show no evidence for this deformation. In reality, the localized net displacements and extension rates on the faults probably go to zero at the fault tips, and the broader deformation field includes non-uniformly distributed strain to accommodate this. It is not possible to include this in the current block model, primarily due to the sparsity of velocity observations.

Instead, two of the most prominent fault zones are used as block boundaries. The more western, a north-trending rift, hosts several geodetic stations along the Lhasa–Golmud Highway. Extension on this rift is calculated at $3.2 \pm 0.7 \text{ mm a}^{-1}$, which may aggregate extension in the less clearly defined rifts of the Tanggula Shan extending over 300 km west to the next block boundary (and geodetic station) at the Shuang Hu graben (Section 3.6.3).

To the southeast, a large NE-striking rift valley is shown to have 2.9 ± 0.7 sinistral slip, with statistically insignificant extension. The block boundary at this sinistral fault continues to the northeast along discontinuous topographic lineaments where it merges with the Yushu segment of the Xianshuihe–Xiaojiang fault system, and may contribute a majority of the Yushu fault’s slip, although definitive Quaternary faulting along the boundary was not able to be identified or mapped. To the southeast from the aforementioned sinistral fault in the Tanggula Shan, the block boundary continues along strike until it merges with the unnamed sinistral conjugate of the dextral Beng Co fault (Section 3.6.2). This creates a ~ 750 km long zone of sinistral shear, connecting the conjugate strike-slip fault systems of central–western Tibet with the Xianshuihe–Xiaojiang system of eastern Tibet (Figure ??).

A broad region of eastern Tibet, extending roughly 350 km north-south between the Jiali and Yushu faults, and 850 km between the Tanggula Shan and Batang fault, has received little neotectonic study and remains poorly characterized. Unlike central and western Tibet, this area is externally drained and is much more rugged, and the topography holds a strong imprint of tectonism throughout the Cenozoic and perhaps earlier (e.g., Spurlin et al., 2005; Staisch et al., 2016). Though seismic activity in the region is generally less than the surrounding regions, scattered moderate-magnitude events are observed. Active faults were not able to be identified in the available imagery (mostly Landsat) with confidence, though a non-fault block boundary was drawn on candidate structures that may be part of the regional extent of the Banggong–Nujiang suture (Taylor & Yin, 2009). Analysis of the relative block rotations indicates that $\sim 3\text{--}4 \text{ mm a}^{-1}$ of deformation may occur throughout the region, perhaps localized on a small number of structures, or perhaps distributed more broadly.

The wide swath of crust between central and eastern Tibet is little explored but likely contains many structures of scientific interest, linking the transtensive tectonics of the high plateau to the west with the complex strike-slip and reverse faults of the orogen's eastern margin. The lack of evidence for active faulting here should not be taken as evidence of absence, but simply a reflection of the challenges of working in the more rugged terrain where rivers incise deep valleys into the plateau.

3.7 Northern Tibet

Deformation in northern Tibet is dominated by two major, subparallel sinistral strike-slip fault systems, the Kunlun and Altyn Tagh fault systems, as well as a transpressional fold belt that connects the eastern margins of the strike-slip systems.

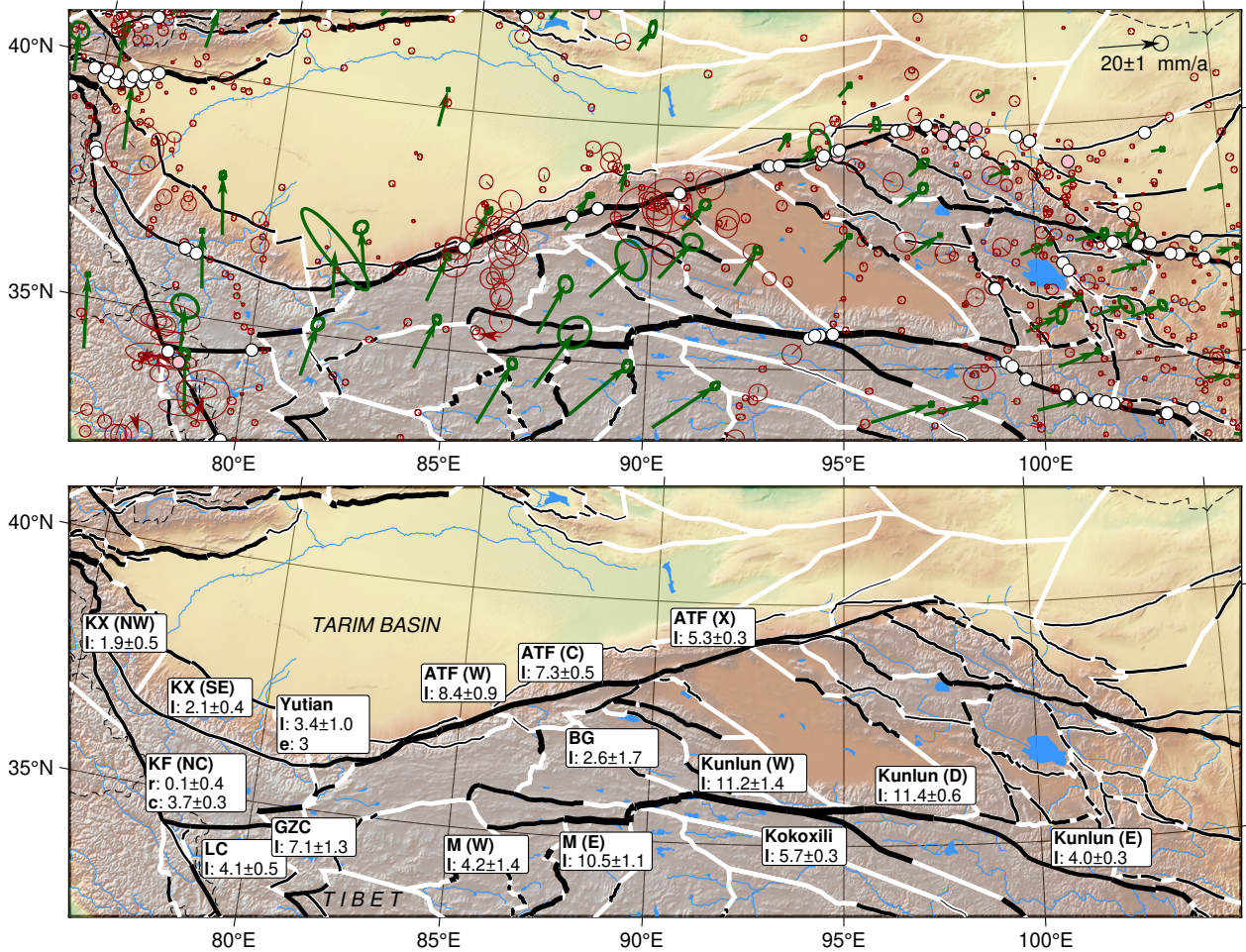


Figure 9: Northern Tibet. KX = Karakax fault. ATF = Altyn Tagh fault. KF = Karakoram fault. LC = Longmu Co fault. GZC = Gozha Co fault. M = Manyi fault. BG = Baiganghu fault.

3.7.1 Kunlun fault system

The sinistral Kunlun fault system as mapped here extends for over 1500 km from northwestern Tibet east to near the Longmen Shan at the eastern margin of the orogen (Figure 9, 11). Like many of the major strike-slip systems in the orogen, the Kunlun fault system serves as a large-scale transfer fault (Figure 4), aggregating strain from extensional-sinistral systems in central Tibet and contractional systems in northern Tibet, transferring it east to the Xianshuihe, Longmen Shan, and other fault systems on the eastern margin of the plateau.

The westernmost part of this system has two parallel E-striking faults in this model; the southern fault is the Manyi

fault, which ruptured in the eponymous *Mw* 7.6 event in 1997 (e.g., Funning et al., 2007), and the northern fault, which may be the western continuation of the Kunlun fault proper (Bell et al., 2011). The Manyi fault is at the northern terminus of the sinistral-normal faults of north-central Tibet; extension and sinistral slip to the south is transferred onto (or off of) sinistral slip on the Kunlun system. The western Manyi fault slips at $4.2 \pm 1.4 \text{ mm a}^{-1}$ sinistral, increasing to 10.5 ± 1.2 past a junction with a rift system to the south.

Sinistral slip rates on the Kunlun fault increase to the east, as extension in north-central Tibet links in with the system. The west-central Kunlun fault slips at about $11.2 \pm 1.4 \text{ mm a}^{-1}$, increasing as reverse faults in the Qimen Tagh region to the north feed in. The highest rates are in the center of the fault system in the Dongdatan valley, at $11.4 \pm 0.7 \text{ mm a}^{-1}$ sinistral, matching Quaternary slip rates (J. Van der Woerd et al., 1998, 2001; J. V. der Van der Woerd et al., 2000). Slip rates on the Kunlun fault decrease by more than half east of the center, as slip is transferred into the faults of the transpressional southeastern Qimen Tagh in northeastern Tibet and farther east from there (Mark B. Allen et al., 2017; e.g., Duvall & Clark, 2010). Sinistral slip rates on the eastern Kunlun fault are $4.0 \pm 0.3 \text{ mm a}^{-1}$, slightly below most Quaternary measurements (Harkins et al., 2010; e.g., Eric Kirby et al., 2007). Slip on the system remains significant towards its eastern terminus, where it links with the faults of the Min Shan and Longmen Shan. The Kokoxili branch of the fault (which hosted the 2001 *Mw* 7.9 earthquake) slips at $5.7 \pm 0.3 \text{ mm a}^{-1}$ sinistral.

3.7.2 Altyn Tagh fault system

The sinistral Altyn Tagh fault (Figure 9) is the longest strike-slip fault system in the Tibetan orogen (Figure 5). It is mapped continuously for 2000 km from the southeastern Pamir and along the northern rim of the Tibetan plateau just south of the Tarim Basin, until it diminishes at the northeasternmost thrusts of the Qilian Shan. It can be observed in satellite imagery discontinuously for another 800 km east to the northern Ordos block.

The Karakax fault is the westernmost fault in the Altyn Tagh system. The fault as mapped here has its northwestern end quite close to the Kongur Shan fault (Figure 6), and extends southeast for 500 km. Sinistral slip increases from $1.9 \pm 0.5 \text{ mm a}^{-1}$ in the northwest to $2.1 \pm 0.4 \text{ mm a}^{-1}$ farther east. There is very little extension or contraction across the fault zone; instead, contraction is accommodated on south-dipping thrust north of the Altyn Tagh where the Tarim basin underthrusts the Tibetan plateau. These thrusts show $1\text{--}2.5 \text{ mm a}^{-1}$ of contraction.

The northeast-striking Altyn Tagh fault proper begins where the Karakax fault and Longmu Co–Gozha Co faults join; the latter fault system has a much faster slip rate than the former (Section 3.6.3), though the former has more structural continuity with the Altyn Tagh.

The fault system here is transpressional, with the Altyn Tagh fault trace flanked to the north and south by reverse faults, dipping towards the Altyn Tagh trace and uplifting narrow mountain ranges (e.g., Cowgill et al., 2000). However, the western Altyn Tagh fault zone itself seems to be locally transtensive, as evidenced by small releasing bends along its length. I find rates of sinistral slip on the western Altyn Tagh fault to be $8.4 \pm 0.9 \text{ mm a}^{-1}$, with up to $2.6 \pm 0.3 \text{ mm a}^{-1}$ extension at the releasing bends. The oblique-reverse faults to the north and south of the primary Altyn Tagh trace accommodate a significant amount of the total deformation across the Altyn Tagh fault system as a whole, at least as expressed in the geodetic data, and compensate for the localized extension along the primary fault zone. These faults accommodate $-0.5 \pm 1.0 \text{ mm a}^{-1}$ of left slip and $0.3 \pm 0.7 \text{ mm a}^{-1}$ shortening. The western Altyn Tagh fault system as a whole accommodates $7.9 \pm 1.3 \text{ mm a}^{-1}$ sinistral slip and $0.3 \pm 0.8 \text{ mm a}^{-1}$ shortening.

The central Altyn Tagh fault system also shows strain to be partitioned between the main Altyn Tagh fault, the North Altyn fault (Cowgill et al., 2000), and the Baiganghu fault to the south. Given the close proximity of these faults and the sparsity of the geodetic data, the block inversion cannot clearly differentiate strain accumulation rates on these three sub-parallel structures. Left unrestrained, the inversion allocates $2\text{--}3 \text{ mm a}^{-1}$ sinistral slip on each. Though no geologic rates have been published for the North Altyn and Baiganghu faults, sinistral slip of $\sim 3 \text{ mm a}^{-1}$ is incompatible with geologic slip rates of $\sim 8.5\text{--}20 \text{ mm a}^{-1}$ on the main Altyn Tagh trace. Therefore I have penalized slip rates on the splays. Following this, the main Altyn Tagh trace is found to slip here at $7.3 \pm 0.5 \text{ mm a}^{-1}$ sinistral with little contraction; this is much more compatible, though still less than, the geologic slip rates of $\sim 8.5\text{--}9.5 \text{ mm a}^{-1}$ (e.g., Cowgill, 2007; Gold et al., 2009) at the well-studied Cherchen He and nearby sites, which use more realistic upper terrace ages for the reconstructions.

The Baiganghu fault (Liu et al., 2017), though essentially unstudied, displays very clear evidence for late Quaternary rupture in satellite imagery along its 160 km length. The Baiganghu fault shows $2.6 \pm 1.7 \text{ mm a}^{-1}$ of left-lateral slip in the southwest, where it has a narrow mountain range with about 1 km relief in the footwall; rates drop to near zero towards the northeast, after the junction with the thrusts of the Qimen Tagh, before it merges with the main Altyn Tagh fault.

The slip rate on the Altyn Tagh fault system decreases to the northeast, as slip is transferred into NW-striking thrust faults of the Qilian Shan–Nan Shan ranges (e.g., Meyer et al., 1998; Yin et al., 2008). The Xorkoli segment of the Altyn Tagh is east of the junction with the Qimen Tagh ranges, with a sinistral rate of $5.3 \pm 0.3 \text{ mm a}^{-1}$. At the Akato Bend, the fault splits into two branches. The southern branch loses much of its rate to the east before joining with the thrusts of the western Qilian Shan, while the northern branch increases its rate to the east; the rates estimated here are in reasonable agreement with A. J. Elliott et al. (2018). Farther to the northeast, the fault slips sinistral at $3.6 \pm 1.0 \text{ mm a}^{-1}$, progressively losing slip to the Qilian Shan thrusts until the Hexi Corridor (Figure 11).

3.7.3 Gobi-Altai and Gobi

The Gobi-Altai region lies at the intersection of Mongolia, Kazakhstan, China and Russia (Figure 9). The region has experienced some of the largest intraplate earthquakes in recorded history, (e.g., Chéry et al., 2001; Schlupp & Cisternas, 2007) along distributed strike-slip faults. The fault network is continuous with faults in the northeastern and southeastern Tien Shan [Section 3.3] and extends east through Mongolia and the Baikal region of Russia. Only faults on the southern and western margins of the region are included in this study; a fault dataset covering Northeastern Asia (Styron et al., 2018) has been produced by GEM as part of a seismic hazard model, though no block modeling has been completed for that dataset.

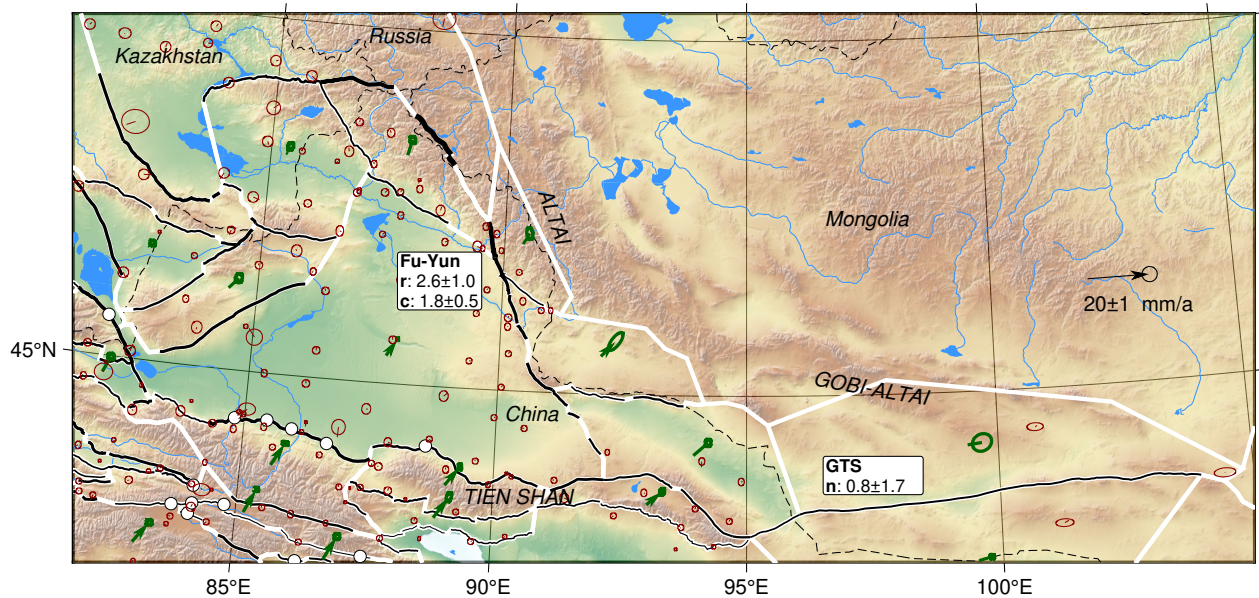


Figure 10: Faults in the Gobi-Altai and surroundings. GTS = Gobi–Tien Shan fault.

Deformation in the western Gobi-Altai is transpressive; east-striking structures accommodate N-S contraction (up to $\sim 2.5 \text{ mm a}^{-1}$) with a secondary sinistral component, while NW-striking structures are dextral-reverse with similar rates; most prominent in this latter set is the Fu-Yun fault that produced a $M 7.9$ earthquake in 1931 (Klinger et al., 2011; Tapponnier & Molnar, 1979), with $2.6 \pm 1.0 \text{ mm a}^{-1}$ dextral and $1.8 \pm 0.5 \text{ mm a}^{-1}$ contraction.

Contraction across the far eastern Tien Shan sums to around 1 mm a^{-1} , as more shortening is accommodated within Tibet to the south than along strike to the west, consistent with a substantial eastward decrease in topography. However, a component of sinistral shear across the range is present in this area as well, which strengthens to the east, as fault geomorphology indicates a transition to a strike-slip dominated regime. The 700 km long master

fault of the Gobi–Tien Shan Fault System (e.g., Cunningham, 2013) shows a left-reverse slip rate of $0.8 \pm 1.7 \text{ mm a}^{-1}$. The trace of this fault is quite straight over its length, suggesting that earthquake ruptures may propagate unimpeded across the fault, leading to large (M 7+) events.

3.7.4 Qimen Tagh

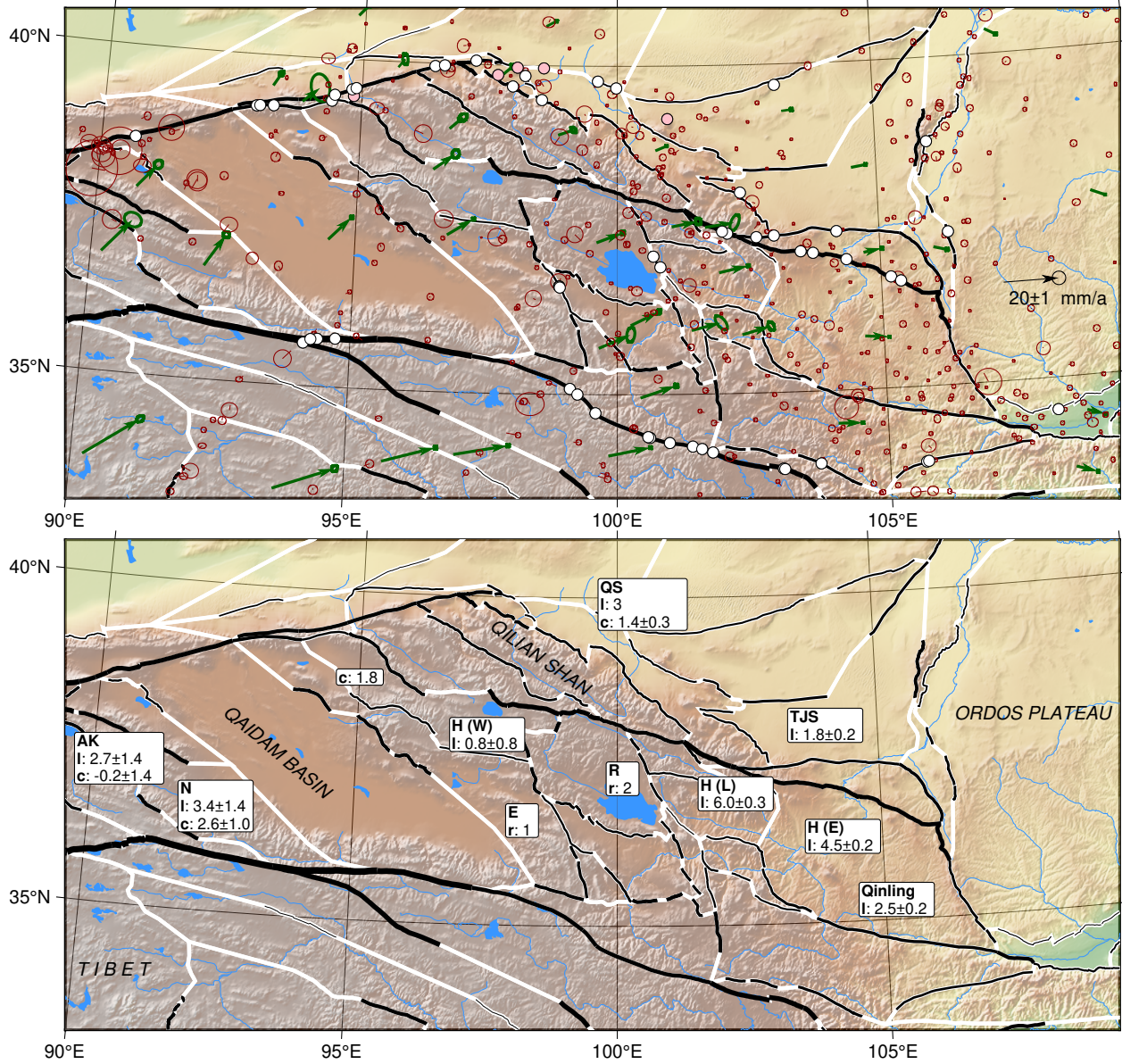


Figure 11: Northeastern Tibet. AK = Ayak Kum Kol fault. N = Narin thrust. H (W) = Western Haiyuan fault. H (L) = Haiyuan fault, Lenglongling fault. H (E) = Eastern Haiyuan fault. E = Elashan fault. R = Ryueshan fault. QS = Qilian Shan thrust. TJS = Tianjinshan fault.

The Qimen Tagh comprises several closely-spaced mountain ranges extending from the central Altyn Tagh fault, east of the Charchen He site, to the central Kunlun fault (Figure 11). The ranges are sinistral-reverse, with slip rates that increase towards the south. The Ayak Kum Kol thrust in the north shows $2.7 \pm 1.4 \text{ mm a}^{-1}$ sinistral slip and no resolvable contraction ($-0.2 \pm 1.4 \text{ mm a}^{-1}$), while the Narin thrust along strike to the southeast shows $3.4 \pm 1.4 \text{ mm a}^{-1}$ and $2.6 \pm 1.1 \text{ mm a}^{-1}$ sinistral and reverse slip, respectively. Like the Qilian Shan thrust belt farther east, these thrusts form a very large transpressional stepover between the Altyn Tagh and Kunlun faults, essentially

transferring sinistral slip from the western Altyn Tagh to the central Kunlun.

3.7.5 Qilian Shan and Hexi Corridor

The Qilian Shan is a contractional basin and range zone that is the northeastern limit of the high topography of the Tibetan orogen. The region hosts an array of NW-striking reverse faults, and WNW- and NNW-striking strike-slip faults. The reverse faults of the Qilian Shan have contractional rates up to 1.8 mm a^{-1} , and up to 3 mm a^{-1} sinistral slip. The northeastern Altyn Tagh fault borders the Qilian Shan on the northwestern margin, and a substantial decrease in its slip rate is linked to crustal shortening along the Qilian Shan, particularly the northeasternmost (frontal) Qilian Shan thrust along the Hexi Corridor. Shortening of this latter structure is $1.4 \pm 0.3 \text{ mm a}^{-1}$ in this study, far greater than geologic slip rates (W. Chen, 2003; W. Min et al., 2002).

3.7.6 Haiyuan fault

The Haiyuan fault is a $\sim 1000 \text{ km}$ long WNW-striking sinistral fault that bisects the Qilian Shan. It is well studied in part because of a great ($M 8+$) earthquake in 1920 (e.g., Liu-Zeng et al., 2007). Like many of the strike-slip faults in the orogen, the slip rate on the Haiyuan fault system is highest in its central segments (Figure 5), increasing from $0.8 \pm 0.8 \text{ mm a}^{-1}$ in the west to $6.0 \pm 0.4 \text{ mm a}^{-1}$ in the central (Lenglongling) segment, as the Qilian Shan thrust feeds slip in. To the east, it splits, with the northern branch becoming the Tianjingshan fault (with a sinistral slip rate of $1.8 \pm 0.2 \text{ mm a}^{-1}$) and the southern continuing as the Haiyuan (with a sinistral slip rate of $4.5 \pm 0.2 \text{ mm a}^{-1}$). The central and eastern Haiyuan and the Tianjinshan faults have received substantial geologic investigation. The rates here are consistent with modern studies (Jiang, Han, et al., 2017; C. Li et al., 2009; X. Li et al., 2017; Zheng et al., 2013).

South of the Haiyuan fault, the WNW-trending ranges are cut by two prominent NW-striking dextral faults that extend south to near the Kunlun fault, the Riyueshan and Elashan faults. These faults accommodate NE-SW shortening and distributed sinistral shear through counterclockwise bookshelf rotation (Duvall & Clark, 2010). Dextral rates on each fault are $1\text{--}2 \text{ mm a}^{-1}$, in line with geologic estimates for those fault segments (Yuan et al., 2011).

3.7.7 Qinling fault

The sinistral West Qinling fault parallels the Haiyuan fault about 200 km south of the Haiyuan, extending farther east into the Weihe graben (Section 3.10.1), which separates the Ordos block in the north from the Qinling mountains to the south. The fault is over 550 km long and quite straight, making it a candidate structure for large magnitude strike-slip earthquakes; historical seismicity includes several $M 7\text{--}8$ earthquakes in the past two millennia (P. Chen & Lin, 2019), though the uncertainties on these magnitude estimates may be large. The West Qinling fault is here estimated to slip sinistally at $2.5 \pm 0.2 \text{ mm a}^{-1}$, right in line with geologic estimates of $2.5\text{--}2.9 \text{ mm a}^{-1}$ by P. Chen & Lin (2019), even though these geologic data were not able to be used in the inversion because the sites could not be located accurately enough.

3.8 Eastern Tibet and the Longmen Shan

The eastern margin of the Tibetan plateau is a physiographic and kinematic transition zone. Here, the rapid strain rates and structural complexity of the high orogen grade into much slower (and less dense) fault separating larger blocks of eastern China. However, the fault slip rates are still moderate by global standards. Most are above the global median of 0.6 mm a^{-1} for intraplate faults (Styron & Pagani, 2020). Combined with the dramatic increase in population density at the orogenic front, this region has some of the highest seismic risk in China.

3.8.1 Eastern termination of the Kunlun fault

Though the slip rate of the Kunlun fault decreases eastward from its central high (Figure 5; Section 3.7.1), this study shows that the rate increases at its eastern terminus, where the Bayan Har crust south of the fault moves rapidly east against the relatively slower western Qinling crust. At this point, the easternmost Kunlun fault (the Maqu segment (Lin & Guo, 2008)) splits into the parallel Bailongjiang fault to the northeast and the Tazang fault

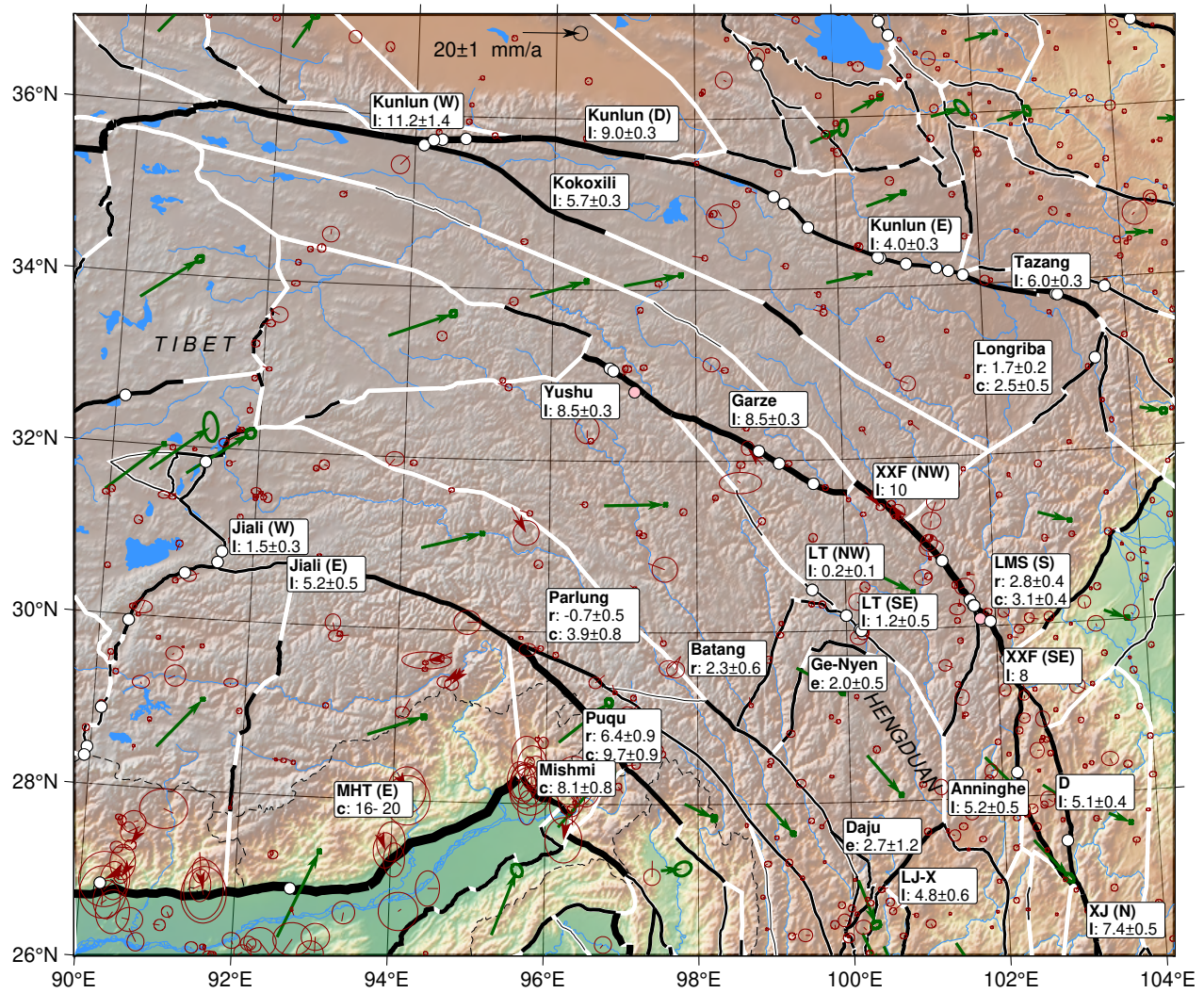


Figure 12: Southeastern Tibet. XS = Xianshuihe fault. D = Daliangshan fault. XJ = Xiaojiang fault. LT = Litang fault. LJ-X = Lixiang-Xiaojinje fault. LMS=Longmenshan fault. MHT = Main Himalayan Thrust.

to the southeast. Though geologic sinistral slip rates on each branch are around 2 mm a^{-1} (H. Li et al., 2020; Ren et al., 2013b), this study finds equivalent rates for the Bailongjiang but faster rates of $6.0 \pm 0.3 \text{ mm a}^{-1}$ for the Tazang.

3.8.2 Longmen Shan

The eastern Tazang fault meets three faults in the Min Shan region. The Longriba fault (Ren et al., 2013a; Xiwei Xu et al., 2008) to the southwest is the fastest slipping, with $1.7 \pm 0.2 \text{ mm a}^{-1}$ right-lateral slip and $2.5 \pm 0.5 \text{ mm a}^{-1}$ shortening. These rates decrease following the block boundary to the southwest, past where the Longriba fault has been mapped or is readily identifiable in satellite imagery. The middle fault east of this fault junction is the Min Shan fault (E. Kirby et al., 2000), and the easternmost may be unnamed; these two faults have sinistral-reverse slip rates of $1\text{--}2 \text{ mm a}^{-1}$.

The southeastern margin of the Longmenshan is bounded by the Longmenshan fault zone, most well known for the devastating 2008 M 7.9 Wenchuan earthquake. The results here show that the Longmenshan range-front fault (here representing both the Beichuan and Pengguan faults (Densmore et al., 2007), though located at the Pengguan fault trace) has $3.1 \pm 0.4 \text{ mm a}^{-1}$ contraction and $2.8 \pm 0.4 \text{ mm a}^{-1}$ dextral slip, which change along strike to the northeast to $3.1 \pm 0.4 \text{ mm a}^{-1}$ dextral and $4.6 \pm 0.7 \text{ mm a}^{-1}$ reverse slip. This northeastern increase in dextral shear was also seen in the kinematics of the 2008 earthquake rupture (Xiwei Xu et al., 2009; G. Zhang et al., 2011).

We also find just over $0.8 \pm 0.5 \text{ mm a}^{-1}$ left-reverse slip on the Longquan fault in western Sichuan Basin.

3.8.3 Xianshuihe–Xiaojiang fault system

South of the eastern Kunlun fault, the sinistral Xianshuihe–Xiaojiang fault system (XXF) is another great strike-slip fault system in the orogen. Like the Altyn Tagh, Kunlun, and Haiyuan fault systems, the XXF accommodates southeastward transport of Tibetan crust away from the impinging Indian crust (e.g., Peltzer & Tapponnier, 1988). Unlike the others, however, the XXF is arcuate, approximating a small circle around the Eastern Himalaya Syntaxis, and is paired by parallel (rather than conjugate) dextral faults, the Puqu and Sagaing fault systems (Figure 13). The crust in between the fault systems moves south-southeast with more gentle internal velocity (and topography) gradients compared to the gradients across the bounding faults.

The XXF starts in the NW along the Jinsha suture (Yang et al., 2012). Here, the fault system comprises several en-echelon segments, including the Yushu segment which ruptured in 2010 (e.g., Z. Li et al., 2011). Geologic left-lateral slip rates for the Yushu segment are around 7.5 mm a^{-1} (X. Huang et al., 2019). This work yields sinistral rates of $8.5 \pm 0.3 \text{ mm a}^{-1}$ for the Yushu segment, and very similar rates for the segments farther southeast, on the Garze fault. Sinistral geologic slip rates on the Garze fault vary between $5\text{--}9 \text{ mm a}^{-1}$ (M.-L. Chevalier et al., 2018).

These rates continue on the Xianshuihe fault proper, $8\text{--}10 \text{ mm a}^{-1}$, a bit higher than the geologic rates of $5\text{--}9 \text{ mm a}^{-1}$ (Bai et al., 2018; G. Chen et al., 2016), with the exception of a rather high rate of 17 mm a^{-1} using a lower terrace age by G. Chen et al. (2016). The source of the discrepancy, on both the Yushu and Xianshuihe faults, is unclear but may be related to inaccurate block geometry resulting from an incomplete catalog of faults that would better represent possible splays as well as fault junctions, on either side of the well-mapped XXF fault system traces.

Fault branches are more common on the southeastern XXF than the northwest. The most prominent is a branch at the southeastern Xianshuihe fault, where it splits into the Anninghe fault to the southwest and the Daliangshan fault to the southeast. The Anninghe fault takes half of the southern Xianshuihe fault, $5.2 \pm 0.5 \text{ mm a}^{-1}$ (He & Ikeda, 2007), and the Daliangshan fault takes $5.1 \pm 0.4 \text{ mm a}^{-1}$ (He et al., 2008). These faults merge about 275 km south of the northern split, at the northern Xiaojiang fault.

The Xiaojiang fault runs N-S for about 300 km through eastern Yunnan province. In the north, the slip rate is $7.4 \pm 0.5 \text{ mm a}^{-1}$, decreasing slightly to the south. The Xiaojiang fault is the fastest slipping, and perhaps most clearly defined, of $5\text{--}6$ parallel sinistral faults spaced $10\text{--}40$ km apart. The next fault to the west, the Puduhe fault, runs through Kunming (the capital of Yunnan, with a metro area population above 6 million), and has a sinistral rate of $1.9 \pm 0.4 \text{ mm a}^{-1}$. These faults accommodate $>10 \text{ mm a}^{-1}$ sinistral shear. All of these faults terminate to the south against the Qujiang fault, a dextral splay of the Red River fault.

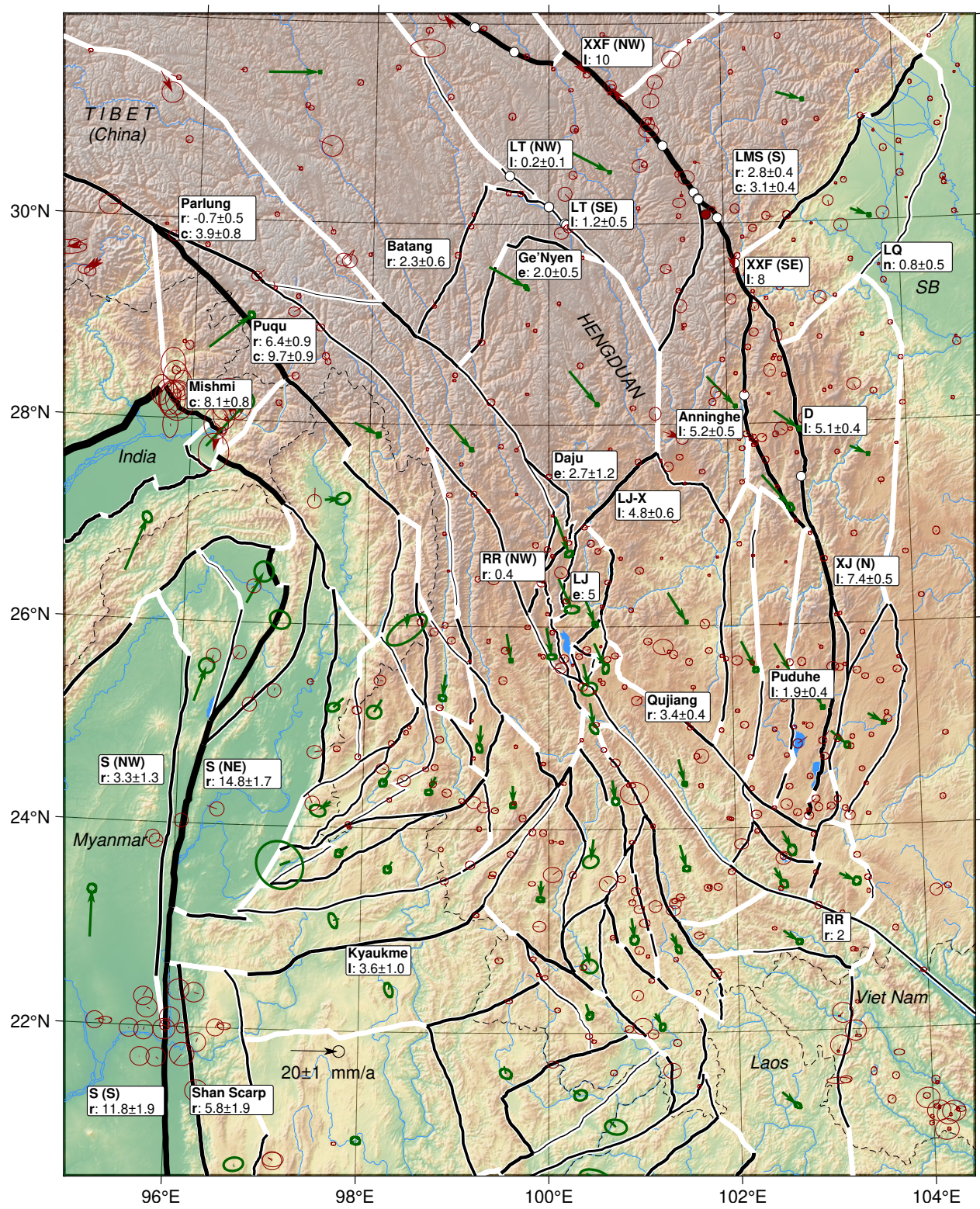


Figure 13: Hengduan area. XXF = Xianshuihe fault. LMS = Longmenshan fault. LQ = Longquan fault. D = Daliangshan fault. LT = Litang fault. LJ-X = Lijiang-Xiaojinhe fault. LJ = Lijiang fault. XJ = Xiaojiang fault. S = Sagaing fault. RR = Red River fault.

3.9 Southeastern Tibet and Indochina

In contrast to most of the margins of the Tibetan plateau, the southeastern margin is topographically gentle (Marin Kristen Clark & Royden, 2000) and has a similarly broad and gentle velocity gradient with respect to south China (Gan et al., 2007), which is not accommodated by reverse faulting. The region can be roughly characterized by a clockwise rotation of a package of crustal material around the Eastern Himalayan Syntaxis, bound on the outer (northern and eastern) margins by the XXF and on the inner by the Puqu and Sagaing faults systems. However, some second-order patterns are important, as well: First, this rotating package of crust is cut obliquely by the dextral Red River fault system, which marks a distinct change in the configuration of faults and blocks on either side, and leads to some structural complexities such as fault stepovers. Second, this rotating package of crust is also undergoing sinistral shear along concentric planes, such that the inner parts of the package have a greater angular velocity than the outer parts; this is particularly apparent south of the Red River fault system. All of these factors lead to greater tectonic complexity than is found anywhere else in the orogen.

In spite of the tectonic complexity, the area has received comparatively little neotectonic study. GNSS coverage is good within China and northern Viet Nam, but is very sparse in Burma, Laos, and northern Thailand. Very little geologic slip rate data are available, and none were found south of the Red River fault. While this made characterizing and modeling the region more challenging than some other regions, it also means that there is a great opportunity for future work, which will refine or refute the results presented here.

3.9.1 High-elevation transtensive faults

The high plateau margin in between the Longmen Shan and the Eastern Himalayan Syntaxis, often called the Hengduan Shan, has relatively few known faults. The few that are known are transtensive, indicating that the crust is accelerating to the SE here. The most well-studied fault is the Litang fault, a sinistral-normal fault parallel to the Xianshuihe fault; the sinistral slip rate on this fault 0.2 ± 0.1 to 1.2 ± 0.5 along strike to the SE, and changes from slightly contractional to having a larger normal component, in reasonable agreement with late Quaternary rates (M.-L. Chevalier, Leloup, et al., 2016; Xiwei Xu et al., 2005).

The Litang fault and its splays are paired by two NE-striking conjugate right-lateral faults, which terminate to the southwest against the Zhongdian fault. The longer, western fault is the Batang fault (E. Wang & Burchfiel, 2000) (not to be confused with another Batang fault at the northwestern end of the XXF), with 2.3 ± 0.6 mm a⁻¹ dextral slip. The eastern fault is not previously described to my knowledge, but has an 85 km long, straight fault trace that is well expressed in topographic and satellite imagery. Most interestingly, this fault is interpreted to meet its conjugate left-normal fault at a narrow Quaternary basin at the foot of the 6200 m Ge'Nyen peak. The mountain front of this peak rises 2600 m above the basin and has well-developed triangular facets up to 1 km tall. This morphology strongly suggests that the peak is the footwall of a relatively narrow rift, an interpretation supported by several moderate magnitude normal earthquakes in 1989 with compatible strikes. The block model results place 2.0 ± 0.5 mm a⁻¹ extension on this fault.

3.9.2 Zhongdian–Lijiang–Dali fault system

Another zone of structural complexity exists in northern Yunnan and southwestern Sichuan provinces, south of the transtensive faults mentioned in Section 3.9.1 (Figure 12). The Zhongdian fault is a dextral fault that parallels the northernmost Red River fault about 80 km northeast of the latter fault. At its southwestern end, it splays into a set of transtensive faults that function as a broad extensional stepover between the Zhongdian and central Red River faults. This zone stretches from Tiger Leaping Gorge just north of Lijiang, south to Dali where the system meets the Red River fault. The Lijiang–Xiaojinhe fault (Xiwei Xu et al., 2003) extends from this area northeast to a half-graben near Yanjingzhen, breaking up the 500 km in between the Litang and Red River splays into two blocks.

At Tiger Leaping Gorge, the Daju normal fault raises the Jade Dragon Snow Mountain (5956 m elevation) in its footwall, creating the 3800 m deep gorge. I find extension of about 2.7 ± 1.2 mm a⁻¹ on this fault, in agreement with the 4 mm a⁻¹ rate observed through dating of the fault scarp by Kong et al. (2010). South of the intersection with the Lijiang–Xiaojinhe fault, the north-striking faults in the Lijiang and Dali areas accommodate about 5 mm a⁻¹ of E-W extension, with lower sinistral strike-slip rates that vary locally based on local block rotations. The Lijiang–Xiaojinhe fault itself accommodates 4.8 ± 0.6 mm a⁻¹ left-slip, with a subordinate reverse component,

similar to geologic rates estimated by Xiwei Xu et al. (2003).

Though the southern end of the Zhongdian–Lijiang–Dali fault system is bound by the Red River fault system, more dextral shear ($3.4 \pm 0.4 \text{ mm a}^{-1}$) is transferred onto the Qujiang fault, north of the Red River fault by about 50 km.

3.9.3 Red River fault system

At the Eastern Himalayan Syntaxis, the Jiali fault splits into the dextral-reverse Parlung and Puqu faults. The Parlung fault continues southeast to the South China Sea as the Red River fault system, while the Puqu fault feeds dextral slip south into a complicated stepover system in northernmost Myanmar that eventually merges with the Sagaing fault system.

Both the Puqu and Parlung faults absorb a substantial amount of shortening ($9.7 \pm 0.9 \text{ mm a}^{-1}$ on the Puqu and $3.9 \pm 0.7 \text{ mm a}^{-1}$ on the Parlung). The area in between the faults is the Kangri Garpo range, which tops out above 6800 m, though the Puqu fault itself is at elevations as low as 1400 m where it crosses the Chayu (Lohit) river a short distance from the range crest. The locations of the Puqu and Parlung faults are readily apparent based on the linearity of the river valleys superposed on them, and separate major tectonostratigraphic packages (Ding et al., 2001), though the active traces are not easily observed in topographic and satellite imagery. Nonetheless, given the linearity of the inferred traces across several kilometers of relief, the faults must dip fairly steeply, so the shortening across the fault systems is likely accommodated on auxiliary reverse faults and perhaps crustal folding. Alternatively, it is possible that the true fault surface of the megathrust as it wraps around from the NW–dipping Main Himalayan Thrust system of the easternmost Himalaya to the NE–dipping Mishmi Thrust is poorly represented by the rectangular faults in the block model, and that much of this shortening is actually accommodated on the Mishmi Thrust (Section 3.9.4).

The Puqu fault also has a high dextral slip rate. The northwestern section of the fault slips dextrally at $6.4 \pm 0.9 \text{ mm a}^{-1}$, though this rate decreases dramatically to the southeast. The concern with this rate is the same as with the convergence rate noted previously.

The Red River fault extends southeast from the Parlung fault, cutting through the clockwise rotating crust of Southeast Tibet with a dextral slip rate varying between $0.4\text{--}2 \text{ mm a}^{-1}$.

Sinistral fault systems to the northeast and southwest terminate against the Red River fault, rather than offsetting it (C. R. Allen et al., 1984). However the clockwise rotation does seem to deform the Red River fault (e.g., Schoenbohm et al., 2006). The trace of the fault is offset in map pattern by about 60 km to the southwest over the central 650 km of the whole trace; the location of this deflection corresponds to the most rapid clockwise rotation, from west of Lijiang to the intersection with the Xiaojiang fault system. The fault-normal component of deformation at the bends is opposite to that of typical releasing and restraining bends.

A retrodeformation of the block model using the instantaneous Euler poles derived in this study shows that the Red River fault system would be approximately linear at about 6 Ma, which suggests that may have been linear in the past (I do not think this should be taken for granted, and I do not think *a priori* that the Euler poles derived here apply millions of years in the past, so the 6 Ma age may not be particularly meaningful). Of the major strike-slip fault systems in Tibet, the Red River fault is the only one that deforms in such a manner; it may be a rare phenomenon worldwide, and indicative of unique or superposed tectonic conditions.

However, the section of the Red River fault between Dali and the Xiaojiang fault has a much lower slip rate than adjacent segments. Instead, the parallel Qujiang fault to the north, and the subparallel Wuliang Shan fault to the south, both accommodate more significant dextral shear. It is possible that the deformation of the Red River fault by regional sinistral shear is slowly deactivating it, and instead transferring dextral shear to more optimally oriented or located segments.

Dextral slip rates on the Red River fault trace itself increase around the intersection with the Xiaojiang fault system, southeast of which there are few parallel faults on which to distribute strain. However, the most southeastern segment of the Red River fault (in northern Viet Nam) also shows very little strike-slip activity; dextral strain along NW-striking planes in the coastal region seems to be accommodated farther south, on a fault near the Viet Nam–Laos border.

3.9.4 Northeast Assam and Mishmi thrust

The northeastern margin of the Assam valley is bordered by the Mishmi hills which rise progressively into the Kangri Garpo range. These mountains are underlain by the Mishmi thrust, the source of the 1950 Mw ~8.6 Assam earthquake (Priyanka et al., 2017). I find contraction rates of $8.1 \pm 0.8 \text{ mm a}^{-1}$ across the Mishmi thrust, with minor strike-slip motion (Figures 13, 14). This rate is fairly high by most standards but one third to one half of the contraction across the adjacent Main Himalaya Thrust. It is also substantially lower than the along-strike continuation to the south, where the northeastern Indo-Burman ranges converge with the crust of northernmost Myanmar along the Dihing River.

3.9.5 Clockwise rotation and sinistral shear in Myanmar and Yunnan

West of the northern Red River fault system and the Lijiang–Dali area, deformation is accommodated through dextral shear along N-striking strike-slip faults in the valleys of the Nu (Mekong) and Lancang (Salween) rivers; these faults are the northern part of the regionally-important Cenozoic Gaoligong dextral shear zone (G. Wang et al., 2008). Dextral slip across these faults is cumulatively about 5 mm a^{-1} . The system changes dramatically from transpressive in the north, related to Himalayan convergence, to transtensive in the south, potentially linked to toroidal mantle flow around the Eastern Himalayan Syntaxis (Soto et al., 2012).

South of the north-striking dextral faults of the northern Gaoligong shear zone, deformation in eastern Myanmar and western Yunnan is primarily accommodated by arcuate, E– to NE–striking sinistral faults that describe small circles around the Eastern Himalaya Syntaxis (similar to the XXF). The northernmost of these faults are relatively short and linked to the north-striking dextral faults; these faults are part of the southwestern Gaoligong shear zone (G. Wang et al., 2008). South of this shear zone, the arcuate sinistral faults become much longer (300–500 km) and in some cases extend from the Sagaing fault to the Red River fault. The most rapid of these is the Kyaukme fault, with a sinistral rate of $3.6 \pm 1.1 \text{ mm a}^{-1}$. In other cases, the fault and block geometry is more complex, particularly where E–W extension is more rapid. The most clear case of this is south of the eastern Nanting fault (the longest of the E–W faults), where the crustal velocity field diverges; to the northwest, the GNSS stations move southwest with respect to Eurasia (part of the clockwise rotation), but to the southeast, the GNSS stations move south and then southeast (a counterclockwise rotation). The smaller blocks west of the Red River fault and south of the Nanting fault accommodate the divergence in the velocity field through counterclockwise bookshelf rotation, with dextral and extensional slip on the faults between them.

These patterns of north-south shortening and east-west extension sinistral slip on broadly ENE–striking faults (small circles around the Eastern Himalaya Syntaxis) and dextral slip on NW-striking faults continue south into northern Laos and Thailand. However, both geologic and geodetic data are much more sparse south of Yunnan, and available evidence suggests that strain rates decrease to the south as well. Further characterization of the region south of Yunnan will await a future project.

3.9.6 Sagaing fault

The north–striking dextral Sagaing fault is directly south of the Eastern Himalaya Syntaxis, running from the Indo-Burman ranges of northern Myanmar south to the Indian Ocean at the Irrawaddy delta. The Sagaing fault is generally considered the main plate boundary fault between the Indian and Eurasian (or Indochina) plates southeast of the Himalaya (Vigny et al., 2003).

Though the total velocity difference between the crust on either side of the Sagaing fault system is about 20 mm a^{-1} in the north and 15 mm a^{-1} farther south, as the crust to the east has a greater southward velocity in the north than in the south. The northern Sagaing fault (between 23°N and 25°N latitude) is split into two strands, with 3.3 ± 1.3 and $14.8 \pm 1.7 \text{ mm a}^{-1}$ dextral slip in the west and east, respectively. Between 23°N and 20°N , the Sagaing is single-stranded, with $11.8 \pm 1.8 \text{ mm a}^{-1}$ of dextral slip, but closely paralleled to the east by the Shan Scarp fault (with $5.8 \pm 1.8 \text{ mm a}^{-1}$ dextral slip), and the Kyaukkyan fault (S. Min et al., 2017) another 65 km to the east, with $1.8 \pm 1.3 \text{ mm a}^{-1}$ dextral shear. Dip slip is variable but minor on these structures.

3.9.7 Indo-Burman ranges and the Shillong Plateau

The Shillong Plateau is an enigmatic basement-cored plateau in the Bramaputra valley of India, the foreland of both the Himalaya and the Indo-Burman ranges (Figure 14). Though active fault traces are challenging to discern in topography data, the current scientific consensus holds that both the northern and southern margins of the plateau are bound by ~E-striking reverse-sense shear zones cutting through the Indian crust, the Dauki fault in the south and the Oldham fault in the north (Biswas et al., 2007; Marin K. Clark & Bilham, 2008; e.g., N. P. Rao & Kumar, 1997).

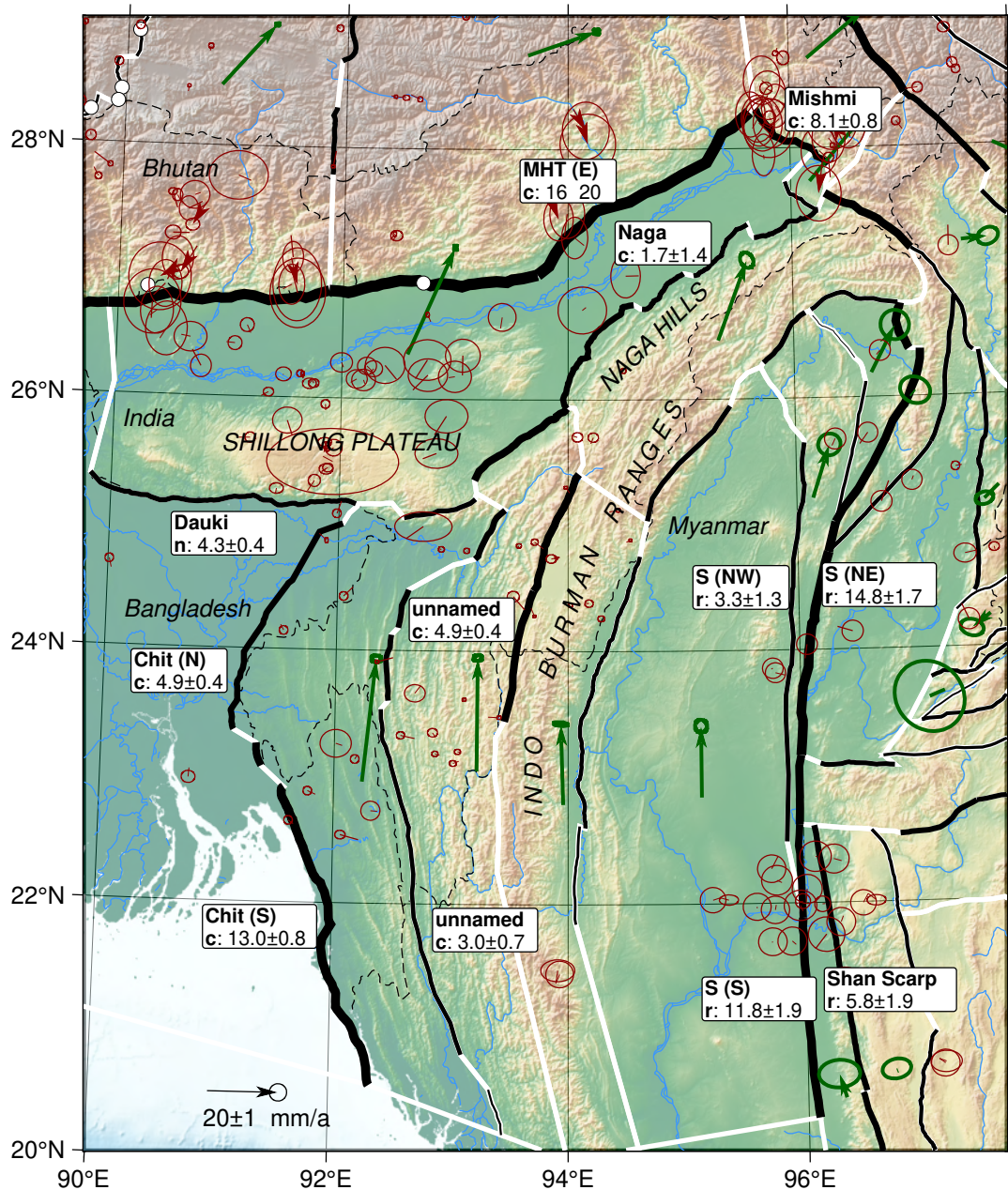


Figure 14: Indo-Burman area and surroundings. MHT = Main Himalayan Thrust. S = Sagaing fault. Chit = Chittagong Coastal Thrust.

Though the Oldham fault is the purported source of a great ($\sim M 8$) earthquake in 1897 (Bilham & England, 2001), its trace is quite cryptic, while the Dauki fault's trace (or at least potential surface projection) is much better located.

Therefore this study locates a block boundary along the Dauki fault, but extends the Shillong block north to the Himalayan front. The Dauki fault on the south side of the Shillong Plateau accommodates $4.3 \pm 0.4 \text{ mm a}^{-1}$ of reverse-sinistral slip. Inspection of the residual velocities do not suggests unmodeled strain localization along the northern margin of the plateau, where the Oldham fault lies.

The Indo-Burman ranges form a N- to NW-striking thrust belt between the Indian subcontinent and the crust of southeastern Eurasia and Indochina, west of the Sagaing fault. The Indo-Burman ranges accommodate contraction related to the eastward component of India's motion relative to Myanmar, as well as some dextral shear on north-striking faults.

The Indo-Burman ranges can be divided into two segments that are partially separated by the eastern Shillong Plateau. The Naga Hills are in the northeast, where the ranges overthrust the Indian crust in the Brahmaputra valley, opposite the easternmost Himalaya. The Chittagong-Tripura fold belt, a thrust wedge atop the east-dipping Chittagong Coastal Thrust, occupies the southwestern part of the ranges. The north-striking Churachandpur Mao fault forms the backstop to the thrust wedge here.

The Chittagong Coastal thrust accommodates much of the E-W shortening across the Indo-Burman ranges south of the Naga Hills. Contraction ranges from $13.0 \pm 0.8 \text{ mm a}^{-1}$ in the south to 4.9 ± 0.4 in the north. Early block model geometries of this region had a single block for the entire fold belt west of the Churachandpur Mao fault, but patterns in the residual GNSS velocities indicated that shortening was occurring within the wedge. An additional N-striking thrust was added, cutting the fold belt in twain, somewhat arbitrarily at a boundary between relatively widely-spaced, low-elevation faults and folds to the west and more tightly-spaced, higher-elevation structures to the east. This removes the systematic pattern to the residuals. Unlike the Chittagong Coastal Thrust, contraction across this fault is highest in the north at $4.9 \pm 0.4 \text{ mm a}^{-1}$, decreasing to 3.0 ± 0.7 towards the coast where more shortening is accommodated on the western frontal thrust.

The Naga Hills thrust shows $1.7 \pm 1.3 \text{ mm a}^{-1}$ contraction near the midpoint of the range, with rates increasing from northeast to southwest, consistent with a clockwise rotation of the block (e.g., Vernant et al., 2014). A dextral component is resolved as well, though this varies with variations in strike.

3.10 Eastern and Northeastern China

Faulting in eastern and northern China is related to the greater eastward motion of southeastern China than northeastern China (in a Eurasia fixed reference frame). The tectonic boundary between these zones is a northeast-trending belt of short, *en-echelon* rifts (the Weihe and Shanxi grabens) accommodating oblique normal faulting. Farther east, the slow relative motions of coastal blocks with the mainland lead to slip on the Tanlu and Yitang-Yilong faults, a great Mesozoic fault zone spanning more than 3000 km. Though seismicity in the region is much less frequent than farther west, earthquakes here have been some of the most deadly in human history.

3.10.1 Ordos plateau and marginal grabens

The Ordos plateau is a rigid block to the northeast of the of the Tibetan plateau and west of the North China plain. The plateau is separated from nearly all of the surrounding crust by normal faults, with the exception of its southwestern flank, which undergoes contraction at $1\text{--}4 \text{ mm a}^{-1}$ against the eastward impinging crust between the Haiyuan and West Qinling faults.

The Yinchuan graben lies to the west of the Ordos block, and extends at $0.7 \pm 0.2 \text{ mm a}^{-1}$, quite similar to rates by Middleton et al. (2016). Extension rates increase to the north, with the Linhe fault extending at $1.7 \pm 0.2 \text{ mm a}^{-1}$. The southern and eastern margins of the Ordos block are the Weihe and Shanxi grabens, respectively.

The Weihe graben is between the Ordos Plateau and the Qinling ranges to the south and southeast. In spite of fairly high rates of extension inferred from geologic estimates of $>1 \text{ mm a}^{-1}$ uplift rates of the rift flanks (G. Rao et al., 2014), the net extension across the rift is here estimated lower, around 0.6 ± 0.4 near Xi'an and the study area of G. Rao et al. (2014). These rates are typical for extension throughout the Weihe and southern Shanxi grabens.

Extension rates are similar in the northern Shanxi rifts, in line with expectations from previous work (Middleton et al., 2017; B. Zhang et al., 1986). I find rates of extension at 0.6 mm a^{-1} across the zone of rifts, slightly lower than geologic rates.

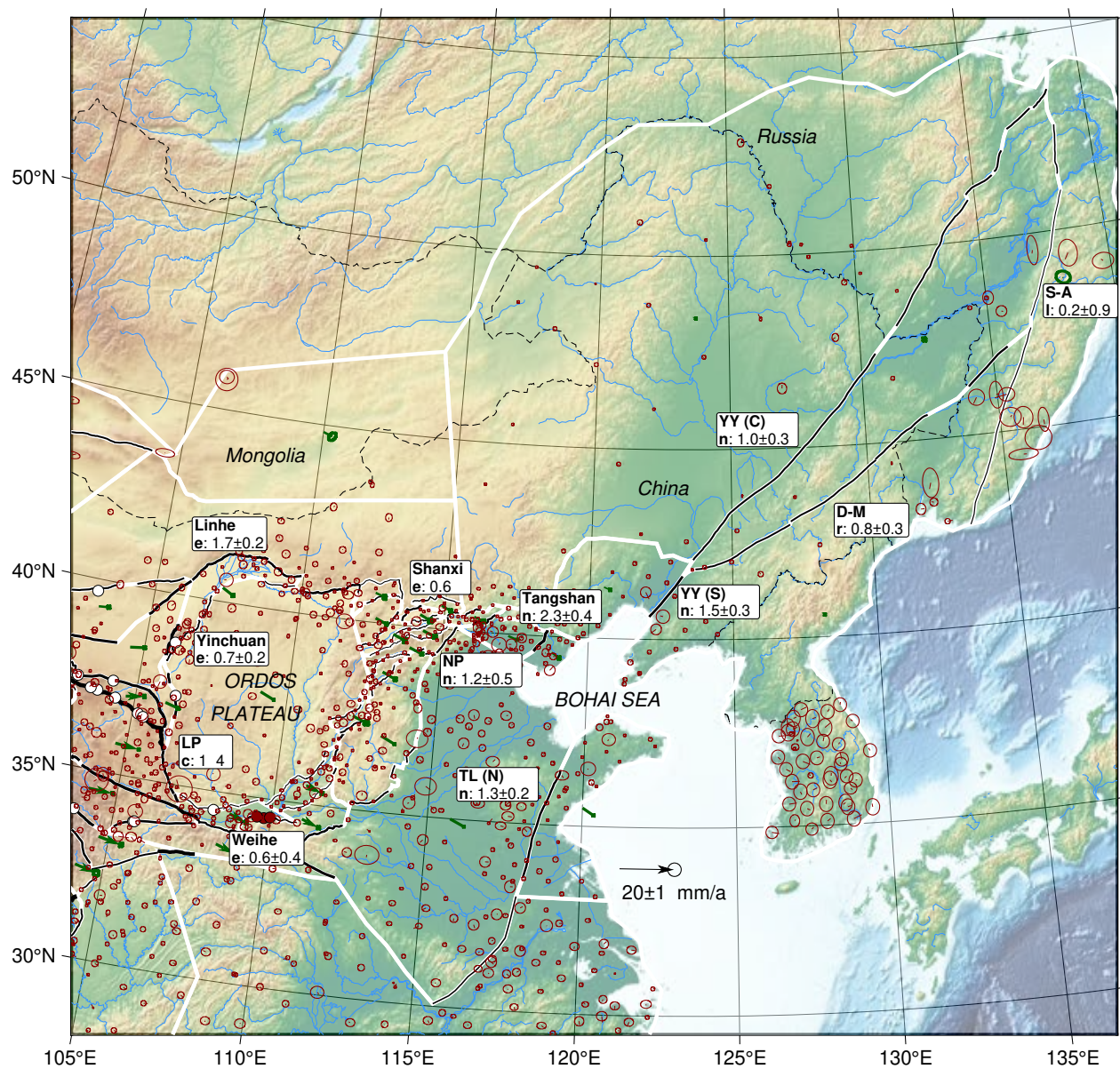


Figure 15: Northeastern China. YY = Yilan-Yitong fault system. S-A = Sikhote-Alin fault system. DM = Dunhua-Mishan fault system. NP = Nankou Piedmont fault. TL = Tanlu fault sustem. LP = Liupan Shan thrust.

3.10.2 Tangshan fault and Bohai Sea

The eastern end of the Shanxi graben transition into a somewhat cryptic zone of faulting that extends eastward past Beijing to the Bohai Sea, where it merges with the great Yilan-Yitong–Tanlu fault system of northeast China and the Amur region of Russia. The faults in this transitional zone are of moderate length (tens of kilometers) and have moderate slip rates. The Nankou Piedmont fault immediately north of Beijing slips at $1.2 \pm 0.5 \text{ mm a}^{-1}$ in a dextral-normal sense; this is typical for the region.

The Tangshan fault (Guo et al., 2011), source of the immensely destructive eponymous earthquake in 1976 (killing at least 242,000 people), is found here to have a slip rate of $2.3 \pm 0.4 \text{ mm a}^{-1}$, mostly dextral with a small normal component. This fault is illustrative of the great seismic risk posed by faults of moderate lengths and slip rates in densely populated areas.

The Bohai sea lies east of the Tangshan fault. This basin is generally interpreted as being influenced by the Tanlu fault zone, with perhaps an earlier phase of rifting (e.g., M. B. Allen et al., 1997). Though deformation on the Tanlu–Yilan-Yitong system passes through the basin still (e.g., Ye et al., 2021), faults in the sea were not well located in available bathymetry, and left out of the model.

3.10.3 Yilan-Yitong fault, Tanlu fault

The Yilan-Yitong and Tanlu faults are sections of the same $\sim 3500 \text{ km}$ long strike-slip fault system stretching from the Sea of Okhotsk to central China; though terminology is inconsistent in the literature, the Yilan-Yitong fault is considered to be north of the Bohai Sea and the Tanlu fault is to the south.

Deformation rates are highest on the fault system near the Bohai Sea. The segment of the Yilan-Yitong on the north shore of the sea slips at $1.5 \pm 0.3 \text{ mm a}^{-1}$, with a dextral-reverse sense, while the long section through Jilin and Heilongjiang provinces, up to the Russian border, slips at $1.0 \pm 0.3 \text{ mm a}^{-1}$ with the same slip sense. Deformation rates decrease by less than half through the Russian segments. Though no Quaternary slip rates are available in the English-language literature, several studies have documented paleoseismicity along the fault (W. Min et al., 2013; Yu et al., 2018), with a similar dextral sense as found here.

The slip rate of the northern Tanlu fault just south of the Bohai Sea is 1.3 ± 0.2 , also dextral-reverse. Holocene activity has been documented on the fault by W. Huang et al. (1996), and a strong earthquake in 1668 has been assigned to the structure by Jiang, Zhang, et al. (2017), who estimate a dextral rate of $2.2\text{--}2.6 \text{ mm a}^{-1}$. Farther south, both the topographic expression of the fault and its estimated rate decrease.

Two major fault systems were mapped to the east of the Yilan-Yitong fault and included in the model based on their strong topographic signature, despite a paucity of existing research supporting current activity. The Dunhua-Mishan fault splays off of the southern Yilan-Yitong fault (W. Min et al., 2013), crossing east into Russia where it terminates at the Sikhote-Alin fault system (Shestakov et al., 2011). The Dunhua-Mishan fault system slips dextrally at $0.8 \pm 0.3 \text{ mm a}^{-1}$, and the Sikhote-Alin slips sinistrally at $0.2 \pm 0.9 \text{ mm a}^{-1}$.

4 Discussion

4.1 Comparison of results with previous geodetic studies

The Indo-Asian collision zone has been the subject of geodetic investigation for decades (Bendick et al., 2000; e.g., Larson et al., 1999; P-Z. Zhang et al., 2004). Geodetic studies of deformation on faults generally fall into two methodological categories: analysis of velocities projected onto profiles across faults, and block models. Other researchers interpolate the velocity observations into a velocity field, and decompose the results into rotation and dilatation components (e.g., Gan et al., 2007) but these results are difficult to quantitatively compare to faults.

In general, the slip rates resolved on faults in these studies is dependent on the size of the blocks, or, equivalently, the length of the across-fault velocity profiles and the spacing of faults included in the profiles. In an idealized case with distributed faulting, larger blocks and more widely-spaced faults will lower slip rates, as strain is allocated onto fewer and fewer blocks. In practice, this is often but not always the case, as more complex deformation patterns within a block can be averaged out.

The most comparable geodetic studies to this study are other block models. These are numerous, and may span a similar spatial scale (Loveless & Meade, 2011; e.g., Brendan J. Meade, 2007; W. Wang et al., 2017), or may be target a smaller region (X. Li et al., 2021; e.g., W. Wang et al., 2021). All of these models have at most a few tens of blocks; the orogen-scale models therefore have very broad blocks relative to the present study, with more rapid slip concentrated at the block boundaries, particularly boundaries that are not directly co-located with known faults, or those farther from the more well studied parts of Tibet (though the orogen-scale model by Loveless & Meade (2011) includes intra-block strain, which reduces these effects somewhat). Nonetheless, all of these studies yield fairly similar rates for most faults.

The regional studies fit more closely with the results presented here, which is not surprising as they have a higher block density, and use much of the same GNSS data. The block model of Northeast Tibet by X. Li et al. (2021) is the only study in the orogen at the same spatial resolution and block density as the present study, and the results agree quite well.

4.2 Comparison of geologic and geodetic slip rates

Discrepancies between fault slip rates estimated from geologic versus geodetic techniques are widely reported, both in the Indo-Asian collision zone and elsewhere. These discrepancies are often considered to be biased, where geologic rates are typically higher than geodetic rates, either due to systematic error in the estimation of geologic slip rates (Cowgill, 2007; Solmaz Mohadjer et al., 2017), or to issues related to the different time scales sampled by the two techniques such as variations in elastic strain accumulation rates throughout the postseismic and interseismic phases (Dolan & Meade, 2017; Hetland & Hager, 2005).

The modeled and “observed” geologic slip rates from this study are shown in Figure 3; please note that geologic slip rates are not directly observed or measured, but are derived based on independent measurements of offset and time, both of which can contain errors in measurement and assumptions (Cowgill, 2007; Solmaz Mohadjer et al., 2017). Furthermore, this study also does not use rates that rely on lower-terrace reconstructions, which removes many of the improbably high geologic slip rates from consideration even before these comparisons are made.

The results displayed in Figure 3 show that many of the geologic rates are within the uncertainty of the geodetic rates, and as discussed in Section 3 on a case by case basis, for most fault studied there is a strong degree of consistency. However, there are some outliers, particularly at the highest slip rates. Indeed, the pattern of the modeled vs. observed rates is perhaps more sigmoidal than linear, with the largest deviations proportional to the rates occurring at the highest values. This is consistent with a recent review of the study region by Solmaz Mohadjer et al. (2017), who found that geologic slip rates were higher than geodetic rates, particularly for large, relatively fast-slipping strike-slip faults.

No claim is made here with regards to the nature of these discrepancies. It is possible that there are systematic issues with many Quaternary slip rate estimation techniques (Cowgill, 2007; Rizza et al., 2019). Or perhaps parts of the geodetic modeling are biased—particularly as blocks get smaller, the corrections used for interseismic strain accumulation will be more significant, which could in principle affect how much strain appears to be smoothly distributed versus allocated onto a few rapidly-slipping faults. It should be noted that these are not mutually-exclusive explanations.

Furthermore, the systematic nature of these discrepancies may not be related to methodological errors, but to real phenomena, such as spatiotemporal variation in strain distribution. Full-earthquake cycle models suggest that geodetically-measured slip rates should vary throughout the cycle, although this has not been uniformly observed in the few cases where it has been investigated (Dolan & Meade, 2017). Earthquake cycle behavior is be more complex than our fairly simple seismic cycle models of periodic, characteristic earthquakes on faults in horizontally-uniform rheological models. Temporally-clustered earthquakes will lead to variations in Quaternary slip rate measurements, as well (Gold et al., 2017; Styron, 2019), which may not be apparent in the interseismic geodetic velocity field. Alternatively, the loading rates on faults in complex networks may change dramatically over thousands of years, even if the orogen-bounding tectonic plate rates are constant (e.g., Zinke et al., 2017).

5 Conclusions

A new active fault database of the Indo-Asian collision zone is presented as HimaTibetMap v.2.0. The mapping is higher resolution than the previous version. The database also contains internally-consistent slip rates, with uncertainties, for all 987 fault sections, derived from an orogen-scale, high-resolution block inversion constrained by GNSS geodetic and Quaternary geologic slip rates. This is a dramatic increase in the completeness of information for fault slip rates in the study area, and will enable more accurate seismic hazard and risk assessments.

6 Data Availability

The fault and block mapping, the GNSS and geologic slip rate data used in the inversion, a script to perform the inversion, and the results are all included in the supplementary information, as well as in a code repository (Styron, 2022a). Running the block inversion requires the free and open-source *Oiler* software (Styron, 2022b). Many figures in this paper were made with *GMT* (Wessel et al., 2019) and *PyGMT* (Uieda et al., 2022).

References

- Abdel-Aziz, M. R. (2006). On the solution of constrained and weighted linear least squares problems. *International Mathematical Forum*, 1067–1076. <https://doi.org/10.12988/imf.2006.06087>
- Ader, T., Avouac, J.-P., Liu-Zeng, J., Lyon-Caen, H., Bollinger, L., Galetzka, J., et al. (2012). Convergence rate across the Nepal Himalaya and interseismic coupling on the Main Himalayan Thrust: Implications for seismic hazard. *Journal of Geophysical Research: Solid Earth*, 117(B4), n/a–n/a. <https://doi.org/10.1029/2011JB009071>
- Allen, C. R., Gillespie, A. R., Han, Y., Sieh, K. E., Zhang, B., & Zhu, C. (1984). Red River and associated faults, Yunnan Province, China: Quaternary geology, slip rates, and seismic hazard. *GSA Bulletin*, 95(6), 686–700. [https://doi.org/10.1130/0016-7606\(1984\)95%3C686:RRAAFY%3E2.0.CO;2](https://doi.org/10.1130/0016-7606(1984)95%3C686:RRAAFY%3E2.0.CO;2)
- Allen, M. B., Macdonald, D. I. M., Xun, Z., Vincent, S. J., & Brouet-Menzies, C. (1997). Early Cenozoic two-phase extension and late Cenozoic thermal subsidence and inversion of the Bohai Basin, northern China. *Marine and Petroleum Geology*, 14(7), 951–972. [https://doi.org/10.1016/S0264-8172\(97\)00027-5](https://doi.org/10.1016/S0264-8172(97)00027-5)
- Allen, M. B., Alsop, G. I., & Zhemchuzhnikov, V. G. (2001). Dome and basin refolding and transpressive inversion along the Karatau Fault System, southern Kazakhstan. *Journal of the Geological Society*, 158(1), 83–95. <https://doi.org/10.1144/jgs.158.1.83>
- Allen, Mark B., Walters, R. J., Song, S., Saville, C., Paola, N. D., Ford, J., et al. (2017). Partitioning of oblique convergence coupled to the fault locking behavior of fold-and-thrust belts: Evidence from the Qilian Shan, northeastern Tibetan Plateau. *Tectonics*, 36(9), 1679–1698. <https://doi.org/10.1002/2017TC004476>
- Armijo, R., Tapponnier, P., Mercier, J. L., & Han, T.-L. (1986). Quaternary extension in southern Tibet: Field observations and tectonic implications. *Journal of Geophysical Research*, 91(B14), 13803. <https://doi.org/10.1029/JB091iB14p13803>
- Armijo, R., Tapponnier, P., & Han, T. (1989). Late Cenozoic right-lateral strike-slip faulting in southern Tibet. *Journal of Geophysical Research: Solid Earth*, 94(B3), 2787–2838. <https://doi.org/10.1029/JB094iB03p02787>
- Avouac, J.-P., & Tapponnier, P. (1993). Kinematic model of active deformation in central Asia. *Geophysical Research Letters*, 20(10), 895–898. <https://doi.org/10.1029/93GL00128>
- Bai, M., Chevalier, M.-L., Pan, J., Replumaz, A., Leloup, P. H., Métois, M., & Li, H. (2018). Southeastward increase of the late Quaternary slip-rate of the Xianshuihe fault, eastern Tibet. Geodynamic and seismic hazard implications. *Earth and Planetary Science Letters*, 485, 19–31. <https://doi.org/10.1016/j.epsl.2017.12.045>
- Bell, M. A., Elliott, J. R., & Parsons, B. E. (2011). Interseismic strain accumulation across the Manyi fault (Tibet) prior to the 1997 Mw 7.6 earthquake. *Geophysical Research Letters*, 38(24). <https://doi.org/10.1029/2011GL049762>

- 1224 Bendick, R., Bilham, R., Freymueller, J., Larson, K., & Yin, G. (2000). Geodetic evidence for a low slip rate in the
1225 Altyn Tagh fault system. *Nature*, 404(6773), 69–72. <https://doi.org/10.1038/35003555>
- 1226 Bendick, R., Bilham, R., Khan, M. A., & Khan, S. F. (2007). Slip on an active wedge thrust from geodetic
1227 observations of the 8 October 2005 Kashmir earthquake. *Geology*, 35(3), 267–270. Retrieved from <http://geology.gsapubs.org/content/35/3/267.short>
1228
- 1229 Berthet, T., Ritz, J.-F., Ferry, M., Pelgay, P., Cattin, R., Drukpa, D., et al. (2014). Active tectonics of the eastern
1230 Himalaya: New constraints from the first tectonic geomorphology study in southern Bhutan. *Geology*, 42(5),
1231 427–430. <https://doi.org/10.1130/G35162.1>
- 1232 Bezanson, J., Edelman, A., Karpinski, S., & Shah, V. B. (2017). Julia: A Fresh Approach to Numerical Computing.
1233 *SIAM Review*, 59(1), 65–98. <https://doi.org/10.1137/141000671>
- 1234 Bian, S., Gong, J., Zuza, A. V., Yang, R., Tian, Y., Ji, J., et al. (2020). Late Pliocene onset of the Cona rift, eastern
1235 Himalaya, confirms eastward propagation of extension in Himalayan-Tibetan orogen. *Earth and Planetary
1236 Science Letters*, 544, 116383. <https://doi.org/10.1016/j.epsl.2020.116383>
- 1237 Bie, L., & Ryder, I. (2014). Recent seismic and aseismic activity in the Ashikule stepover zone, NW Tibet. *Geophysical
1238 Journal International*, 198(3), 1632–1643. <https://doi.org/10.1093/gji/ggu230>
- 1239 Bilham, R., & England, P. (2001). Plateau ‘pop-up’ in the great 1897 Assam earthquake. *Nature*, 410(6830),
1240 806–809.
- 1241 Biswas, S., Coutand, I., Grujic, D., Hager, C., Stöckli, D., & Grasemann, B. (2007). Exhumation and uplift of
1242 the Shillong plateau and its influence on the eastern Himalayas: New constraints from apatite and zircon
1243 (U-Th-[Sm])/He and apatite fission track analyses. *Tectonics*, 26(6). <https://doi.org/10.1029/2007TC002125>
- 1244 Blisniuk, P. M., & Sharp, W. D. (2003). Rates of late Quaternary normal faulting in central Tibet from U-series
1245 dating of pedogenic carbonate in displaced fluvial gravel deposits. *Earth and Planetary Science Letters*, 215(1-2),
1246 169–186. [https://doi.org/10.1016/S0012-821X\(03\)00374-1](https://doi.org/10.1016/S0012-821X(03)00374-1)
- 1247 Bollinger, L., Sapkota, S. N., Tapponnier, P., Klinger, Y., Rizza, M., Woerd, J. V. der, et al. (2014). Estimating
1248 the return times of great Himalayan earthquakes in eastern Nepal: Evidence from the Patu and Bardibas
1249 strands of the Main Frontal Thrust. *Journal of Geophysical Research: Solid Earth*, 119(9), 7123–7163. <https://doi.org/10.1002/2014JB010970>
1250
- 1251 Borthakur, A. (2017). An Analysis of the Conflict in the Ferghana Valley. *Asian Affairs*, 48(2), 334–350. <https://doi.org/10.1080/03068374.2017.1313591>
1252
- 1253 Brown, E. T. (2005). Comment on "Slip-Rate Measurements on the Karakorum Fault May Imply Secular Variations
1254 in Fault Motion". *Science*, 309(5739), 1326b–1326b. <https://doi.org/10.1126/science.1112508>
- 1255 Burchfiel, B. C., Quidong, D., Molnar, P., Royden, L., Yipeng, W., Peizhen, Z., & Weiqi, Z. (1989). Intracrustal
1256 detachment within zones of continental deformation. *Geology*, 17(8), 748–752. [https://doi.org/10.1130/0091-7613\(1989\)017%3C0448:IDWZOC%3E2.3.CO;2](https://doi.org/10.1130/0091-7613(1989)017%3C0448:IDWZOC%3E2.3.CO;2)
1257
- 1258 Burgess, W. P., Yin, A., Dubey, C. S., Shen, Z.-K., & Kelty, T. K. (2012). Holocene shortening across the Main
1259 Frontal Thrust zone in the eastern Himalaya. *Earth and Planetary Science Letters*, 357-358, 152–167. <https://doi.org/10.1016/j.epsl.2012.09.040>
1260
- 1261 Burtman, V. S., Skobelev, S. F., & Molnar, P. (1996). Late Cenozoic slip on the Talas-Ferghana fault, the Tien Shan,
1262 central Asia. *GSA Bulletin*, 108(8), 1004–1021. [https://doi.org/10.1130/0016-7606\(1996\)108%3C1004:LCSOTT%3E2.3.CO;2](https://doi.org/10.1130/0016-7606(1996)108%3C1004:LCSOTT%3E2.3.CO;2)
1263
- 1264 Campbell, G. E., Walker, R. T., Abdrakhmatov, K., Schwenninger, J., Jackson, J., Elliott, J. R., & Copley, A.
1265 (2013). The Dzhungarian fault: Late Quaternary tectonics and slip rate of a major right-lateral strike-slip
1266 fault in the northern Tien Shan region. *Journal of Geophysical Research: Solid Earth*, 118(10), 5681–5698.
1267 <https://doi.org/10.1002/jgrb.50367>
- 1268 Campbell, G. E., Walker, R. T., Abdrakhmatov, K., Jackson, J., Elliott, J. R., Mackenzie, D., et al. (2015). Great
1269 earthquakes in low strain rate continental interiors: An example from SE Kazakhstan. *Journal of Geophysical*

Research: *Solid Earth*, 120(8), 5507–5534. <https://doi.org/10.1002/2015JB011925>

Charreau, J., Saint-Carlier, D., Dominguez, S., Lavé, J., Blard, P.-H., Avouac, J.-P., et al. (2017). Denudation outpaced by crustal thickening in the eastern Tianshan. *Earth and Planetary Science Letters*, 479, 179–191. <https://doi.org/10.1016/j.epsl.2017.09.025>

Chase, C. G. (1972). The N Plate Problem of Plate Tectonics. *Geophysical Journal International*, 29(2), 117–122. <https://doi.org/10.1111/j.1365-246X.1972.tb02202.x>

Chen, G., Xu, X., Wen, X., & Chen, Y.-G. (2016). Late Quaternary Slip-rates and Slip Partitioning on the Southeastern Xianshuihe Fault System, Eastern Tibetan Plateau. *Acta Geologica Sinica - English Edition*, 90(2), 537–554. <https://doi.org/https://doi.org/10.1111/1755-6724.12689>

Chen, P., & Lin, A. (2019). Tectonic topography and Late Pleistocene activity of the West Qinling Fault, northeastern Tibetan Plateau. *Journal of Asian Earth Sciences*, 176, 68–78. <https://doi.org/10.1016/j.jseae.2019.02.007>

Chen, W. (2003). *Principal tectonic deformation features and their generation mechanism in the Hexi Corridor and its adjacent regions since the late Quaternary* ({PhD}). Institute of Geology, China Earthquake Administration, Beijing.

Chéry, J., Carretier, S., & Ritz, J.-F. (2001). Postseismic stress transfer explains time clustering of large earthquakes in Mongolia. *Earth and Planetary Science Letters*, 194(1), 277–286.

Chevalier, M.-L., Ryerson, F. J., Tapponnier, P., Finkel, R. C., Woerd, J. V. D., Haibing, L., & Qing, L. (2005). Slip-Rate Measurements on the Karakorum Fault May Imply Secular Variations in Fault Motion. *Science*, 307(5708), 411–414. <https://doi.org/10.1126/science.1105466>

Chevalier, M.-L., Li, H., Pan, J., Pei, J., Wu, F., Xu, W., et al. (2011). Fast slip-rate along the northern end of the Karakorum fault system, western Tibet. *Geophysical Research Letters*, 38(22). <https://doi.org/10.1029/2011GL049921>

Chevalier, M.-L., Tapponnier, P., Van der Woerd, J., Ryerson, F. J., Finkel, R. C., & Li, H. (2012). Spatially constant slip rate along the southern segment of the Karakorum fault since 200ka. *Tectonophysics*, 530–531, 152–179. <https://doi.org/10.1016/j.tecto.2011.12.014>

Chevalier, M.-L., Pan, J., Li, H., Liu, D., & Wang, M. (2015). Quantification of both normal and right-lateral late Quaternary activity along the Kongur Shan extensional system, Chinese Pamir. *Terra Nova*, 27(5), 379–391. <https://doi.org/https://doi.org/10.1111/ter.12170>

Chevalier, M.-L., Van der Woerd, J., Tapponnier, P., Li, H., Ryerson, F. J., & Finkel, R. C. (2016). Late Quaternary slip-rate along the central Bangong-Chaxikang segment of the Karakorum fault, western Tibet. *GSA Bulletin*, 128(1-2), 284–314. <https://doi.org/10.1130/B31269.1>

Chevalier, M.-L., Leloup, P. H., Replumaz, A., Pan, J., Liu, D., Li, H., et al. (2016). Tectonic-geomorphology of the Litang fault system, SE Tibetan Plateau, and implication for regional seismic hazard. *Tectonophysics*, 682, 278–292. <https://doi.org/10.1016/j.tecto.2016.05.039>

Chevalier, M.-L., Pan, J., Li, H., Sun, Z., Liu, D., Pei, J., et al. (2017). First tectonic-geomorphology study along the Longmu–Gozha Co fault system, Western Tibet. *Gondwana Research*, 41, 411–424. <https://doi.org/10.1016/j.gr.2015.03.008>

Chevalier, M.-L., Leloup, P. H., Replumaz, A., Pan, J., Métois, M., & Li, H. (2018). Temporally constant slip rate along the Ganzi fault, NW Xianshuihe fault system, eastern Tibet. *GSA Bulletin*, 130(3-4), 396–410. <https://doi.org/10.1130/B31691.1>

Chevalier, M.-L., Tapponnier, P., Woerd, J. van der, Leloup, P. H., Wang, S., Pan, J., et al. (2020). Late Quaternary Extension Rates Across the Northern Half of the Yadong-Gulu Rift: Implication for East-West Extension in Southern Tibet. *Journal of Geophysical Research: Solid Earth*, 125(7), e2019JB019106. <https://doi.org/10.1029/2019JB019106>

Clark, Marin K., & Bilham, R. (2008). Miocene rise of the Shillong Plateau and the beginning of the end for the Eastern Himalaya. *Earth and Planetary Science Letters*, 269(3), 337–351. <https://doi.org/10.1016/j.epsl.2008>

- Clark, Marin Kristen, & Royden, L. H. (2000). Topographic ooze: Building the eastern margin of Tibet by lower crustal flow. *Geology*, 28(8), 703. [https://doi.org/10.1130/0091-7613\(2000\)28%3C703:TOBTEM%3E2.0.CO;2](https://doi.org/10.1130/0091-7613(2000)28%3C703:TOBTEM%3E2.0.CO;2)
- Cowgill, E. (2007). Impact of riser reconstructions on estimation of secular variation in rates of strike-slip faulting: Revisiting the Charchen River site along the Altyn Tagh Fault, NW China. *Earth and Planetary Science Letters*, 254(3-4), 239–255. <https://doi.org/10.1016/j.epsl.2006.09.015>
- Cowgill, E., Yin, A., Feng, W. X., & Qing, Z. (2000). Is the North Altyn fault part of a strike-slip duplex along the Altyn Tagh fault system? *Geology*, 28(3), 255–258.
- Cowgill, E., Yin, A., Harrison, T. M., & Xiao-Feng, W. (2003). Reconstruction of the Altyn Tagh fault based on U-Pb geochronology: Role of back thrusts, mantle sutures, and heterogeneous crustal strength in forming the Tibetan Plateau: RECONSTRUCTION OF THE ALTYN TAGH FAULT SYSTEM. *Journal of Geophysical Research: Solid Earth*, 108(B7). <https://doi.org/10.1029/2002JB002080>
- Cox, A., & Hart, R. B. (1986). *Plate tectonics: How it works*. Palo Alto: Blackwell Scientific Publications.
- Cunningham, D. (2013). Mountain building processes in intracontinental oblique deformation belts: Lessons from the Gobi Corridor, Central Asia. *Journal of Structural Geology*, 46, 255–282. <https://doi.org/10.1016/j.jsg.2012.08.010>
- Davis, T. A. (2004). Algorithm 832: UMFPACK V4.3—an unsymmetric-pattern multifrontal method. *ACM Transactions on Mathematical Software*, 30(2), 196–199. <https://doi.org/10.1145/992200.992206>
- Densmore, A. L., Ellis, M. A., Li, Y., Zhou, R., Hancock, G. S., & Richardson, N. (2007). Active tectonics of the Beichuan and Pengguan faults at the eastern margin of the Tibetan Plateau. *Tectonics*, 26(4). <https://doi.org/https://doi.org/10.1029/2006TC001987>
- Ding, L., Zhong, D., Yin, A., Kapp, P., & Harrison, T. M. (2001). Cenozoic structural and metamorphic evolution of the eastern Himalayan syntaxis (Namche Barwa). *Earth and Planetary Science Letters*, 192(3), 423–438. [https://doi.org/10.1016/S0012-821X\(01\)00463-0](https://doi.org/10.1016/S0012-821X(01)00463-0)
- Dolan, J. F., & Meade, B. J. (2017). A Comparison of Geodetic and Geologic Rates Prior to Large Strike-Slip Earthquakes: A Diversity of Earthquake-Cycle Behaviors? *Geochemistry, Geophysics, Geosystems*, 18(12), 4426–4436. <https://doi.org/10.1002/2017GC007014>
- Duvall, A. R., & Clark, M. K. (2010). Dissipation of fast strike-slip faulting within and beyond northeastern Tibet. *Geology*, 38(3), 223–226.
- Elliott, A. J., Oskin, M. E., Liu-zeng, J., & Shao, Y.-X. (2018). Persistent rupture terminations at a restraining bend from slip rates on the eastern Altyn Tagh fault. *Tectonophysics*, 733, 57–72. <https://doi.org/10.1016/j.tecto.2018.01.004>
- Elliott, J., & Freymueller, J. T. (2020). A Block Model of Present-Day Kinematics of Alaska and Western Canada. *Journal of Geophysical Research: Solid Earth*, 125(7), e2019JB018378. <https://doi.org/https://doi.org/10.1029/2019JB018378>
- Evans, E. L., Loveless, J. P., & Meade, B. J. (2015). Total variation regularization of geodetically and geologically constrained block models for the Western United States. *Geophysical Journal International*, 202(2), 713–727. <https://doi.org/10.1093/gji/ggv164>
- Faulds, J. E., & Varga, R. J. (1998). The role of accommodation zones and transfer zones in the regional segmentation of extended terranes. In *Accommodation zones and transfer zones; the regional segmentation of the Basin and Range Province*. Geological Society of America. <https://doi.org/10.1130/0-8137-2323-X.1>
- Funning, G. J., Parsons, B., & Wright, T. J. (2007). Fault slip in the 1997 Manyi, Tibet earthquake from linear elastic modelling of InSAR displacements. *Geophysical Journal International*, 169(3), 988–1008. <https://doi.org/10.1111/j.1365-246X.2006.03318.x>

- Gan, W., Zhang, P., Shen, Z.-K., Niu, Z., Wang, M., Wan, Y., et al. (2007). Present-day crustal motion within the Tibetan Plateau inferred from GPS measurements. *Journal of Geophysical Research*, 112(B8). <https://doi.org/10.1029/2005JB004120>
- Garthwaite, M. C., Wang, H., & Wright, T. J. (2013). Broad-scale interseismic deformation and fault slip rates in the central Tibetan Plateau observed using InSAR. *Journal of Geophysical Research: Solid Earth*, 118(9), 5071–5083. <https://doi.org/10.1002/jgrb.50348>
- Gibbs, A. D. (1984). Structural evolution of extensional basin margins. *Journal of the Geological Society*, 141(4), 609–620.
- Gold, R. D., Cowgill, E., Arrowsmith, J. R., Gosse, J., Chen, X., & Wang, X. (2009). Riser diachroneity, lateral erosion, and uncertainty in rates of strike-slip faulting: A case study from Tuzidun along the Altyn Tagh Fault, NW China. *Journal of Geophysical Research*, 114(B4). <https://doi.org/10.1029/2008JB005913>
- Gold, R. D., Cowgill, E., Arrowsmith, J. R., & Friedrich, A. M. (2017). Pulsed strain release on the Altyn Tagh fault, northwest China. *Earth and Planetary Science Letters*, 459, 291–300. <https://doi.org/10.1016/j.epsl.2016.11.024>
- Gulliksson, M., & Wedin, P. (1992). Modifying the QR-Decomposition to Constrained and Weighted Linear Least Squares. *SIAM Journal on Matrix Analysis and Applications*, 13(4), 1298–1313. <https://doi.org/10.1137/0613079>
- Guo, H., Jiang, W., & Xie, X. (2011). Late-Quaternary strong earthquakes on the seismogenic fault of the 1976 Ms7.8 Tangshan earthquake, Hebei, as revealed by drilling and trenching. *Science China Earth Sciences*, 54(11), 1696. <https://doi.org/10.1007/s11430-011-4218-x>
- Ha, G., Wu, Z., & Liu, F. (2019). Late Quaternary vertical slip rates along the Southern Yadong–Gulu Rift, Southern Tibetan Plateau. *Tectonophysics*, 755, 75–90. <https://doi.org/10.1016/j.tecto.2019.02.014>
- Hammond, W. C., Blewitt, G., & Kreemer, C. (2011). Block modeling of crustal deformation of the northern Walker Lane and Basin and Range from GPS velocities. *Journal of Geophysical Research: Solid Earth*, 116(B4). <https://doi.org/10.1029/2010JB007817>
- Harkins, N., Kirby, E., Shi, X., Wang, E., Burbank, D., & Chun, F. (2010). Millennial slip rates along the eastern Kunlun fault: Implications for the dynamics of intracontinental deformation in Asia. *Lithosphere*, 2(4), 247–266. <https://doi.org/10.1130/L85.1>
- He, H.-L., & Ikeda, Y. (2007). Faulting on the Anninghe fault zone, Southwest China in Late Quaternary and its movement model. *Acta Seismologica Sinica*, 20(5), 571–583. <https://doi.org/10.1007/s11589-007-0571-4>
- He, H.-L., Ikeda, Y., He, Y., Togo, M., Chen, J., Chen, C., et al. (2008). Newly-generated Daliangshan fault zone — Shortcutting on the central section of Xianshuihe-Xiaojiang fault system. *Science in China Series D: Earth Sciences*, 51(9), 1248–1258. <https://doi.org/10.1007/s11430-008-0094-4>
- Hetland, E. A., & Hager, B. H. (2005). Postseismic and interseismic displacements near a strike-slip fault: A two-dimensional theory for general linear viscoelastic rheologies. *Journal of Geophysical Research*, 110(B10). <https://doi.org/10.1029/2005JB003689>
- Hodges, K. V., Wobus, C., Ruhl, K., Schildgen, T., & Whipple, K. (2004). Quaternary deformation, river steepening, and heavy precipitation at the front of the Higher Himalayan ranges. *Earth and Planetary Science Letters*, 220(3-4), 379–389. [https://doi.org/10.1016/S0012-821X\(04\)00063-9](https://doi.org/10.1016/S0012-821X(04)00063-9)
- Hollingsworth, J., Wernicke, B. P., & Ding, L. (2010). Fault slip-rate estimate for the right-lateral Beng Co strike-slip fault, based on Quaternary dating of displaced paleo-lake shorelines. *AGU Fall Meeting Abstracts*, 43, T43C-2229. Retrieved from <http://adsabs.harvard.edu/abs/2010AGUFM.T43C2229H>
- Huang, W., Gao, W., & Ding, G. (1996). Neogene volcanism and Holocene earthquakes in the Tanlu fault zone, eastern China. *Tectonophysics*, 260(4), 259–270. [https://doi.org/10.1016/0040-1951\(95\)00195-6](https://doi.org/10.1016/0040-1951(95)00195-6)
- Huang, X., Jing, Z., Xie, F., & Zhao, J. (2019). Late quaternary slip rate of the east segment of the Yushu fault in the central-eastern Tibetan Plateau. *Quaternary International*, 532, 146–156. <https://doi.org/10.1016/j.quaint>

- Jarrard, R. D. (1986). Relations among subduction parameters. *Reviews of Geophysics*, 24(2), 217. <https://doi.org/10.1029/RG024i002p00217>
- Jiang, W., Zhang, J., Han, Z., Tian, T., Jiao, Q., Wang, X., & Jiang, H. (2017). Characteristic Slip of Strong Earthquakes Along the Yishu Fault Zone in East China Evidenced by Offset Landforms. *Tectonics*, 36(10), 1947–1965. <https://doi.org/10.1002/2016TC004363>
- Jiang, W., Han, Z., Guo, P., Zhang, J., Jiao, Q., Kang, S., & Tian, Y. (2017). Slip rate and recurrence intervals of the east Lenglongling fault constrained by morphotectonics: Tectonic implications for the northeastern Tibetan Plateau. *Lithosphere*, 9(3), 417–430. <https://doi.org/10.1130/L597.1>
- Jouanne, F., Mugnier, J. L., Gamond, J. F., Fort, P. L., Pandey, M. R., Bollinger, L., et al. (2004). Current shortening across the Himalayas of Nepal. *Geophysical Journal International*, 157(1), 1–14. <https://doi.org/10.1111/j.1365-246X.2004.02180.x>
- Kapp, J. L. D., Harrison, T. M., Kapp, P., Grove, M., Lovera, O. M., & Lin, D. (2005). Nyainqentanglha Shan: A window into the tectonic, thermal, and geochemical evolution of the Lhasa block, southern Tibet. *Journal of Geophysical Research: Solid Earth*, 110(B8). <https://doi.org/10.1029/2004JB003330>
- Kapp, P., & DeCelles, P. G. (2019). Mesozoic–Cenozoic geological evolution of the Himalayan–Tibetan orogen and working tectonic hypotheses. *American Journal of Science*, 319(3), 159–254. <https://doi.org/10.2475/03.2019.01>
- Kapp, P., Taylor, M., Stockli, D., & Ding, L. (2008). Development of active low-angle normal fault systems during orogenic collapse: Insight from Tibet, 4.
- Kirby, E., Whipple, K. X., Burchfiel, B. C., Tang, W., Berger, G., Sun, Z., & Chen, Z. (2000). Neotectonics of the Min Shan, China: Implications for mechanisms driving Quaternary deformation along the eastern margin of the Tibetan Plateau. *Geological Society of America Bulletin*, 112(3), 375–393. [https://doi.org/10.1130/0016-7606\(2000\)112%3C375:NOTMSC%3E2.0.CO;2](https://doi.org/10.1130/0016-7606(2000)112%3C375:NOTMSC%3E2.0.CO;2)
- Kirby, Eric, Harkins, N., Wang, E., Shi, X., Fan, C., & Burbank, D. (2007). Slip rate gradients along the eastern Kunlun fault. *Tectonics*, 26(2). <https://doi.org/https://doi.org/10.1029/2006TC002033>
- Klinger, Y., Etchebes, M., Tapponnier, P., & Narteau, C. (2011). Characteristic slip for five great earthquakes along the Fuyun fault in China. *Nature Geoscience*, 4(6), 389–392. <https://doi.org/10.1038/ngeo1158>
- Kong, P., Fink, D., Na, C., & Xiao, W. (2010). Dip-slip rate determined by cosmogenic surface dating on a Holocene scarp of the Daju fault, Yunnan, China. *Tectonophysics*, 493(1), 106–112. <https://doi.org/10.1016/j.tecto.2010.07.006>
- Kreemer, C., Blewitt, G., & Klein, E. C. (2014). A geodetic plate motion and Global Strain Rate Model. *Geochemistry, Geophysics, Geosystems*, 15(10), 3849–3889. <https://doi.org/10.1002/2014GC005407>
- Kumar, S., Wesnousky, S. G., Rockwell, T. K., Ragona, D., Thakur, V. C., & Seitz, G. G. (2001). Earthquake Recurrence and Rupture Dynamics of Himalayan Frontal Thrust, India. *Science*, 294(5550), 2328–2331. <https://doi.org/10.1126/science.1066195>
- Kundu, B., Yadav, R. K., Bali, B. S., Chowdhury, S., & Gahalaut, V. K. (2014). Oblique convergence and slip partitioning in the NW Himalaya: Implications from GPS measurements: NW HIMALAYAN TECTONICS. *Tectonics*, 33(10), 2013–2024. <https://doi.org/10.1002/2014TC003633>
- Larson, K. M., Bürgmann, R., Bilham, R., & Freymueller, J. T. (1999). Kinematics of the India-Eurasia collision zone from GPS measurements. *Journal of Geophysical Research: Solid Earth*, 104(B1), 1077–1093. <https://doi.org/10.1029/1998JB900043>
- Lavé, J., & Avouac, J. P. (2000). Active folding of fluvial terraces across the Siwaliks Hills, Himalayas of central Nepal. *Journal of Geophysical Research: Solid Earth*, 105(B3), 5735–5770. <https://doi.org/10.1029/1999JB900292>
- Lensen, G. J. (1964). The General Case of Progressive Fault Displacement of Flights of Degradational Terraces. *New Zealand Journal of Geology and Geophysics*, 7(4), 864–870. <https://doi.org/10.1080/00288306.1964.10428134>

- Li, C., Zhang, P., Yin, J., & Min, W. (2009). Late Quaternary left-lateral slip rate of the Haiyuan fault, northeastern margin of the Tibetan Plateau. *Tectonics*, 28(5). <https://doi.org/10.1029/2008TC002302>
- Li, H., Zhang, Y., Dong, S., Zhang, J., Sun, Y., & Wang, Q. (2020). Neotectonics of the Bailongjiang and Hanan faults: New insights into late Cenozoic deformation along the eastern margin of the Tibetan Plateau. *GSA Bulletin*, 132(9-10), 1845–1862. <https://doi.org/10.1130/B35374.1>
- Li, K., Wang, D., Shao, Q.-F., & Xu, X. (2018). Holocene slip rate along the NE-trending Qixiang Co fault in the central Tibetan Plateau and its tectonic implications. *Seismology and Geology*, 40(6), 1204–1215. <https://doi.org/10.3969/j.isn.0253-4967.2018.06.002>
- Li, K., Kirby, E., Xu, X., Chen, G., Ren, J., & Wang, D. (2019). Rates of Holocene normal faulting along the Dong Co fault in central Tibet, based on ¹⁴C dating of displaced fluvial terraces. *Journal of Asian Earth Sciences*, 183, 103962. <https://doi.org/10.1016/j.jseas.2019.103962>
- Li, X., Li, C., Wesnousky, S. G., Zhang, P., Zheng, W., Pierce, I. K. D., & Wang, X. (2017). Paleoseismology and slip rate of the western Tianjingshan fault of NE Tibet, China. *Journal of Asian Earth Sciences*, 146, 304–316. <https://doi.org/10.1016/j.jseas.2017.04.031>
- Li, X., Pierce, I. K. D., Bormann, J. M., Hammond, W. C., Zhang, Z., Li, C., et al. (2021). Tectonic Deformation of the Northeastern Tibetan Plateau and Its Surroundings Revealed With GPS Block Modeling. *Journal of Geophysical Research: Solid Earth*, 126(5), e2020JB020733. <https://doi.org/10.1029/2020JB020733>
- Li, Z., Elliott, J. R., Feng, W., Jackson, J. A., Parsons, B. E., & Walters, R. J. (2011). The 2010 MW 6.8 Yushu (Qinghai, China) earthquake: Constraints provided by InSAR and body wave seismology. *Journal of Geophysical Research: Solid Earth*, 116(B10). <https://doi.org/https://doi.org/10.1029/2011JB008358>
- Lin, A., & Guo, J. (2008). Nonuniform Slip Rate and Millennial Recurrence Interval of Large Earthquakes along the Eastern Segment of the Kunlun Fault, Northern Tibet. *Bulletin of the Seismological Society of America*, 98(6), 2866–2878. <https://doi.org/10.1785/0120070193>
- Liu, D., Li, H., Sun, Z., Pan, J., Wang, M., Wang, H., & Marie-LuceChevalier. (2017). AFT dating constrains the Cenozoic uplift of the Qimen Tagh Mountains, Northeast Tibetan Plateau, comparison with LA-ICPMS Zircon U–Pb ages. *Gondwana Research*, 41, 438–450. <https://doi.org/10.1016/j.gr.2015.10.008>
- Liu-Zeng, J., Klinger, Y., Xu, X., Lasserre, C., Chen, G., Chen, W., et al. (2007). Millennial Recurrence of Large Earthquakes on the Haiyuan Fault near Songshan, Gansu Province, China. *Bulletin of the Seismological Society of America*, 97(1B), 14–34. <https://doi.org/10.1785/0120050118>
- Loveless, J. P., & Meade, B. J. (2011). Partitioning of localized and diffuse deformation in the Tibetan Plateau from joint inversions of geologic and geodetic observations. *Earth and Planetary Science Letters*, 303(1-2), 11–24. <https://doi.org/10.1016/j.epsl.2010.12.014>
- Lu, H., Li, B., Wu, D., Zhao, J., Zheng, X., Xiong, J., & Li, Y. (2019). Spatiotemporal patterns of the Late Quaternary deformation across the northern Chinese Tian Shan foreland. *Earth-Science Reviews*, 194, 19–37. <https://doi.org/10.1016/j.earscirev.2019.04.026>
- Malik, J. N., & Nakata, T. (2003). Active faults and related Late Quaternary deformation along the Northwestern Himalayan Frontal Zone, India. Retrieved from <https://www.earth-prints.org/handle/2122/996>
- Malik, J. N., Sahoo, S., Satuluri, S., & Okumura, K. (2015). Active Fault and Paleoseismic Studies in Kangra Valley: Evidence of Surface Rupture of a Great Himalayan 1905 Kangra Earthquake (Mw 7.8), Northwest Himalaya, India. *Bulletin of the Seismological Society of America*, 105(5), 2325–2342. <https://doi.org/10.1785/0120140304>
- McCaffrey, R. (1994). Global variability in subduction thrust zone-forearc systems. *Pure and Applied Geophysics*, 142(1), 173–224. <https://doi.org/10.1007/BF00875971>
- McCaffrey, R. (2002). Crustal Block Rotations and Plate Coupling. In S. Stein & J. T. Freymueller (Eds.), *Geodynamics Series* (pp. 101–122). Washington, D. C.: American Geophysical Union. <https://doi.org/10.1029/GD030p0101>

- 1498 McCaffrey, R., & Nabelek, J. (1998). Role of oblique convergence in the active deformation of the Himalayas and
1499 southern Tibet plateau. *Geology*, 26(8), 691–694. Retrieved from [http://geology.gsapubs.org/content/26/8/6](http://geology.gsapubs.org/content/26/8/691.short)
1500 91.short
- 1501 McGuire, R., Toro, G., Veneziano, D., Cornell, C., Hu, Y., Jin, Y., et al. (1992). Non-stationarity of historical
1502 seismicity in China. In *Proc. Tenth World Conf. On Earthquake Engineering, Balkema, Rotterdam* (pp. 287–292).
- 1503 Meade, Brendan J. (2007). Present-day kinematics at the India-Asia collision zone. *Geology*, 35(1), 81. <https://doi.org/10.1130/G22924A.1>
1504
- 1505 Meade, B. J., & Loveless, J. P. (2009). Block Modeling with Connected Fault-Network Geometries and a Linear
1506 Elastic Coupling Estimator in Spherical Coordinates. *Bulletin of the Seismological Society of America*, 99(6),
1507 3124–3139. <https://doi.org/10.1785/0120090088>
- 1508 Metzger, S., Schurr, B., Ratschbacher, L., Sudhaus, H., Kufner, S.-K., Schöne, T., et al. (2017). The 2015 Mw7.2 Sarez
1509 Strike-Slip Earthquake in the Pamir Interior: Response to the Underthrusting of India's Western Promontory.
1510 *Tectonics*, 2017TC004581. <https://doi.org/10.1002/2017TC004581>
- 1511 Metzger, S., Ischuk, A., Deng, Z., Ratschbacher, L., Perry, M., Kufner, S.-K., et al. (2020). Dense GNSS Profiles
1512 Across the Northwestern Tip of the India-Asia Collision Zone: Triggered Slip and Westward Flow of the Peter
1513 the First Range, Pamir, Into the Tajik Depression. *Tectonics*, 39(2), e2019TC005797. [https://doi.org/10.1029/](https://doi.org/10.1029/2019TC005797)
1514 2019TC005797
- 1515 Meyer, B., Tapponnier, P., Bourjot, L., Métivier, F., Gaudemer, Y., Peltzer, G., et al. (1998). Crustal thickening in
1516 Gansu-Qinghai, lithospheric mantle subduction, and oblique, strike-slip controlled growth of the Tibet plateau.
1517 *Geophysical Journal International*, 135(1), 1–47. <https://doi.org/10.1046/j.1365-246X.1998.00567.x>
- 1518 Middleton, T. A., Walker, R. T., Rood, D. H., Rhodes, E. J., Parsons, B., Lei, Q., et al. (2016). The tectonics of the
1519 western Ordos Plateau, Ningxia, China: Slip rates on the Luoshan and East Helanshan Faults. *Tectonics*, 35(11),
1520 2754–2777. <https://doi.org/10.1002/2016TC004230>
- 1521 Middleton, T. A., Elliott, J. R., Rhodes, E. J., Sherlock, S., Walker, R. T., Wang, W., et al. (2017). Extension rates
1522 across the northern Shanxi Grabens, China, from Quaternary geology, seismicity and geodesy. *Geophysical*
1523 *Journal International*, 209(2), 535–558. <https://doi.org/10.1093/gji/ggx031>
- 1524 Min, S., Watkinson, I. M., Tun, S. T., Naing, W., & Swe, T. L. (2017). The Kyaukkyan Fault, Myanmar. *Geological*
1525 *Society, London, Memoirs*, 48(1), 453–471. <https://doi.org/10.1144/M48.21>
- 1526 Min, W., Zhang, P., He, W., Li, C., Mao, F., & Zhang, S. (2002). Research on the active faults and paleoearthquakes
1527 in the western Jiuquan basin. *Seismology and Geology*, 24(1), 35–44.
- 1528 Min, W., Liu, Y., Jiao, D., Shen, J., & Pan, X. (2013). Evidence for Holocene activity of the Yilan-Yitong fault,
1529 northeastern section of the Tan-Lu fault zone in Northeast China. *Journal of Asian Earth Sciences*, 67–68,
1530 207–216. <https://doi.org/10.1016/j.jseae.2013.02.031>
- 1531 Minster, J. B., Jordan, T. H., Molnar, P., & Haines, E. (1974). Numerical modelling of instantaneous plate tectonics.
1532 *Geophysical Journal International*, 36(3), 541–576. Retrieved from [http://onlinelibrary.wiley.com/doi/10.1111/](http://onlinelibrary.wiley.com/doi/10.1111/1/j.1365-246X.1974.tb00613.x/full)
1533 1/j.1365-246X.1974.tb00613.x/full
- 1534 Mohadjer, S., Bendick, R., Ischuk, A., Kuzikov, S., Kostuk, A., Saydullaev, U., et al. (2010). Partitioning of India-
1535 Eurasia convergence in the Pamir-Hindu Kush from GPS measurements. *Geophysical Research Letters*, 37(4),
1536 L04305. <https://doi.org/10.1029/2009GL041737>
- 1537 Mohadjer, Solmaz, Ehlers, T. A., Bendick, R., & Mutz, S. G. (2017). Review of GPS and Quaternary fault slip rates
1538 in the Himalaya-Tibet orogen. *Earth-Science Reviews*, 174(Supplement C), 39–52. [https://doi.org/10.1016/j.ear](https://doi.org/10.1016/j.earscirev.2017.09.005)
1539 rscirev.2017.09.005
- 1540 Murphy, M. A., Yin, A., Kapp, P., Harrison, T. M., Manning, C. E., Ryerson, F. J., et al. (2002). Structural evolution of
1541 the Gurla Mandhata detachment system, southwest Tibet: Implications for the eastward extent of the Karakoram
1542 fault system. *Geological Society of America Bulletin*, 114(4), 428–447. [https://doi.org/10.1130/0016-](https://doi.org/10.1130/0016-7606(2002)114%3C0428:SEOTGM%3E2.0.CO;2)
1543 7606(2002)114%3C0428:SEOTGM%3E2.0.CO;2

- Murphy, M. A., Taylor, M. H., Gosse, J., Silver, C. R. P., Whipp, D. M., & Beaumont, C. (2014). Limit of strain partitioning in the Himalaya marked by large earthquakes in western Nepal. *Nature Geoscience*, 7(1), 38–42. <https://doi.org/10.1038/ngeo2017>
- Nakata, T. (1989). Active faults of the Himalaya of India and Nepal. In *Geological Society of America Special Papers* (Vol. 232, pp. 243–264). Geological Society of America. <https://doi.org/10.1130/SPE232-p243>
- Peltzer, G., & Tapponnier, P. (1988). Formation and evolution of strike-slip faults, rifts, and basins during the India-Asia Collision: An experimental approach. *Journal of Geophysical Research: Solid Earth*, 93(B12), 15085–15117. <https://doi.org/10.1029/JB093iB12p15085>
- Powers, P. M., Lillie, R. J., & Yeats, R. S. (1998). Structure and shortening of the Kangra and Dehra Dun reentrants, Sub-Himalaya, India. *GSA Bulletin*, 110(8), 1010–1027. [https://doi.org/10.1130/0016-7606\(1998\)110%3C1010:SASOTK%3E2.3.CO;2](https://doi.org/10.1130/0016-7606(1998)110%3C1010:SASOTK%3E2.3.CO;2)
- Priyanka, R. S., Jayangondaperumal, R., Pandey, A., Mishra, R. L., Singh, I., Bhushan, R., et al. (2017). Primary surface rupture of the 1950 Tibet-Assam great earthquake along the eastern Himalayan front, India. *Scientific Reports*, 7(1), 5433. <https://doi.org/10.1038/s41598-017-05644-y>
- Rao, G., Lin, A., Yan, B., Jia, D., & Wu, X. (2014). Tectonic activity and structural features of active intracontinental normal faults in the Weihe Graben, central China. *Tectonophysics*, 636, 270–285. <https://doi.org/10.1016/j.tecto.2014.08.019>
- Rao, N. P., & Kumar, M. R. (1997). Uplift and Tectonics of the Shillong Plateau, Northeast India. *Journal of Physics of the Earth*, 45(3), 167–176. <https://doi.org/10.4294/jpe1952.45.167>
- Ren, J., Xu, X., Yeats, R. S., & Zhang, S. (2013a). Latest Quaternary paleoseismology and slip rates of the Longriba fault zone, eastern Tibet: Implications for fault behavior and strain partitioning. *Tectonics*, 32(2), 216–238. <https://doi.org/https://doi.org/10.1002/tect.20029>
- Ren, J., Xu, X., Yeats, R. S., & Zhang, S. (2013b). Millennial slip rates of the Tazang fault, the eastern termination of Kunlun fault: Implications for strain partitioning in eastern Tibet. *Tectonophysics*, 608, 1180–1200. <https://doi.org/10.1016/j.tecto.2013.06.026>
- Rizza, M., Abdrakhmatov, K., Walker, R., Braucher, R., Guillou, V., Carr, A. S., et al. (2019). Rate of Slip From Multiple Quaternary Dating Methods and Paleoseismic Investigations Along the Talas-Fergana Fault: Tectonic Implications for the Tien Shan Range. *Tectonics*, 38(7), 2477–2505. <https://doi.org/10.1029/2018TC005188>
- Robinson, A. C. (2009). Evidence against Quaternary slip on the northern Karakorum Fault suggests kinematic reorganization at the western end of the Himalayan–Tibetan orogen. *Earth and Planetary Science Letters*, 286(1-2), 158–170. <https://doi.org/10.1016/j.epsl.2009.06.025>
- Rust, D., Korzhennikov, A., & Tibaldi, A. (2018). Geologic Slip-Rate Determinations on the Talas-Fergana Fault: Mismatch With Geodetic Slip Rate. *Geophysical Research Letters*, 45(9), 3880–3888. <https://doi.org/10.1002/2017GL076990>
- Sanchez, V. I., Murphy, M. A., Robinson, A. C., Lapen, T. J., & Heizler, M. T. (2013). Tectonic evolution of the India–Asia suture zone since Middle Eocene time, Lopukangri area, south-central Tibet. *Journal of Asian Earth Sciences*, 62, 205–220. <https://doi.org/10.1016/j.jseas.2012.09.004>
- Savage, J. C., & Burford, R. O. (1973). Geodetic determination of relative plate motion in central California. *Journal of Geophysical Research*, 78(5), 832–845. <https://doi.org/10.1029/JB078i005p00832>
- Scharer, K. M., Burbank, D. W., Chen, J., Weldon, R. J., Rubin, C., Zhao, R., & Shen, J. (2004). Detachment folding in the Southwestern Tian Shan–Tarim foreland, China: Shortening estimates and rates. *Journal of Structural Geology*, 26(11), 2119–2137. <https://doi.org/10.1016/j.jsg.2004.02.016>
- Schlupp, A., & Cisternas, A. (2007). Source history of the 1905 great Mongolian earthquakes (Tsetserleg, Bolnay). *Geophysical Journal International*, 169(3), 1115–1131. <https://doi.org/10.1111/j.1365-246X.2007.03323.x>
- Schoenbohm, L. M., Burchfiel, B. C., Liangzhong, C., & Jiyun, Y. (2006). Miocene to present activity along the Red River fault, China, in the context of continental extrusion, upper-crustal rotation, and lower-crustal flow. *GSA*

Bulletin, 118(5-6), 672–688. <https://doi.org/10.1130/B25816.1>

Shah, A. A., Rajasekharan, A., Batmanathan, N., Farhan, Z., & Malik, J. N. (2021). Dras Fault: A major active fault in Kashmir Himalaya, 9.

Shestakov, N. V., Gerasimenko, M. D., Takahashi, H., Kasahara, M., Bormotov, V. A., Bykov, V. G., et al. (2011). Present tectonics of the southeast of Russia as seen from GPS observations. *Geophysical Journal International*, 184(2), 529–540. <https://doi.org/10.1111/j.1365-246X.2010.04871.x>

Shi, X., Kirby, E., Lu, H., Robinson, R., Furlong, K. P., & Wang, E. (2014). Holocene slip rate along the Gyaring Co Fault, central Tibet. *Geophysical Research Letters*, 41(16), 5829–5837. <https://doi.org/10.1002/2014GL060782>

Silver, C. R. P., Murphy, M. A., Taylor, M. H., Gosse, J., & Baltz, T. (2015). Neotectonics of the Western Nepal Fault System: Implications for Himalayan strain partitioning. *Tectonics*, 34(12), 2494–2513. <https://doi.org/10.1002/2014TC003730>

Soto, G. L., Sandvol, E., Ni, J. F., Flesch, L., Hearn, T. M., Tilmann, F., et al. (2012). Significant and vertically coherent seismic anisotropy beneath eastern Tibet. *Journal of Geophysical Research: Solid Earth*, 117(B5). <https://doi.org/https://doi.org/10.1029/2011JB008919>

Spurlin, M. S., Yin, A., Horton, B. K., Zhou, J., & Wang, J. (2005). Structural evolution of the Yushu-Nangqian region and its relationship to syncollisional igneous activity, east-central Tibet. *GSA Bulletin*, 117(9-10), 1293–1317. <https://doi.org/10.1130/B25572.1>

Staisch, L. M., Niemi, N. A., Clark, M. K., & Chang, H. (2016). Eocene to late Oligocene history of crustal shortening within the Hoh Xil Basin and implications for the uplift history of the northern Tibetan Plateau. *Tectonics*, 35(4), 2015TC003972. <https://doi.org/10.1002/2015TC003972>

Stevens, V. L., & Avouac, J. P. (2015). Interseismic coupling on the main Himalayan thrust. *Geophysical Research Letters*, 42(14), 5828–5837. <https://doi.org/10.1002/2015GL064845>

Styron, R. H. (2019). The impact of earthquake cycle variability on neotectonic and paleoseismic slip rate estimates. *Solid Earth*, 10(1), 15–25. <https://doi.org/https://doi.org/10.5194/se-10-15-2019>

Styron, R. H. (2022a, October). China Active Faults. <https://doi.org/10.5281/zenodo.7268805>

Styron, R. H. (2022b, October). Oiler. <https://doi.org/10.5281/zenodo.7262453>

Styron, R. H., & Pagani, M. (2020). The GEM Global Active Faults Database. *Earthquake Spectra*, 8755293020944182. <https://doi.org/10.1177/8755293020944182>

Styron, R. H., Taylor, M., & Okoronkwo, K. (2010). Database of Active Structures From the Indo-Asian Collision. *Eos, Transactions American Geophysical Union*, 91(20), 181–182. <https://doi.org/10.1029/2010EO200001>

Styron, R. H., Taylor, M. H., & Murphy, M. A. (2011). Oblique convergence, arc-parallel extension, and the role of strike-slip faulting in the High Himalaya. *Geosphere*, 7(2), 582–596. Retrieved from <http://geosphere.gsapubs.org/content/7/2/582.short>

Styron, R. H., Taylor, M. H., Sundell, K. E., Stockli, D. F., Oalmann, J. A. G., Möller, A., et al. (2013). Miocene initiation and acceleration of extension in the South Lunggar rift, western Tibet: Evolution of an active detachment system from structural mapping and (U-Th)/He thermochronology: SOUTH LUNGGAR RIFT, SW TIBET. *Tectonics*, n/a–n/a. <https://doi.org/10.1002/tect.20053>

Styron, R. H., Poggi, V., & Lunina, O. V. (2018). GEM Northeastern Asia Active Fault Database. Global Earthquake Model Foundation. <https://doi.org/10.13117/NE-ASIA-ACTIVE-FAULTS>

Styron, R. H., García-Pelaez, J., & Pagani, M. (2020). CCAF-DB: The Caribbean and Central American active fault database. *Natural Hazards and Earth System Sciences*, 20(3), 831–857. <https://doi.org/https://doi.org/10.5194/nhess-20-831-2020>

Sundell, K. E., Taylor, M. H., Styron, R. H., Stockli, D. F., Kapp, P., Hager, C., et al. (2013). Evidence for constriction and Pliocene acceleration of east-west extension in the North Lunggar rift region of west central Tibet: NORTH LUNGGAR RIFT, WEST CENTRAL TIBET. *Tectonics*, 32(5), 1454–1479. <https://doi.org/10.1002/tect.20086>

- Tapponnier, P., & Molnar, P. (1977). Active faulting and tectonics in China. *Journal of Geophysical Research* (1896-1977), 82(20), 2905–2930. <https://doi.org/10.1029/JB082i020p02905>
- Tapponnier, P., & Molnar, P. (1979). Active faulting and Cenozoic tectonics of the Tien Shan, Mongolia, and Baykal Regions. *Journal of Geophysical Research: Solid Earth*, 84(B7), 3425–3459. <https://doi.org/10.1029/JB084iB07p03425>
- Taylor, M., & Peltzer, G. (2006). Current slip rates on conjugate strike-slip faults in central Tibet using synthetic aperture radar interferometry: STRIKE-SLIP SAR RATES, CENTRAL TIBET. *Journal of Geophysical Research: Solid Earth*, 111(B12), n/a–n/a. <https://doi.org/10.1029/2005JB004014>
- Taylor, M., & Yin, A. (2009). Active structures of the Himalayan-Tibetan orogen and their relationships to earthquake distribution, contemporary strain field, and Cenozoic volcanism. *Geosphere*, 5(3), 199–214. <https://doi.org/10.1130/GES00217.1>
- Taylor, M., Yin, A., Ryerson, F. J., Kapp, P., & Ding, L. (2003). Conjugate strike-slip faulting along the Bangong-Nujiang suture zone accommodates coeval east-west extension and north-south shortening in the interior of the Tibetan Plateau: CONJUGATE STRIKE-SLIP FAULTING WITHIN TIBET. *Tectonics*, 22(4), n/a–n/a. <https://doi.org/10.1029/2002TC001361>
- Team, Q. D. (2022). QGIS Geographic Information System. QGIS Association. Retrieved from www.qgis.org
- Thompson Jobe, J. A., Li, T., Chen, J., Burbank, D. W., & Bufe, A. (2017). Quaternary tectonic evolution of the Pamir-Tian Shan convergence zone, Northwest China. *Tectonics*, 36(12), 2748–2776. <https://doi.org/10.1002/2017TC004541>
- Thompson, S. C., Weldon, R. J., Rubin, C. M., Abdrakhmatov, K., Molnar, P., & Berger, G. W. (2002). Late Quaternary slip rates across the central Tien Shan, Kyrgyzstan, central Asia. *Journal of Geophysical Research: Solid Earth*, 107(B9), ETG 7-1-ETG 7-32. <https://doi.org/10.1029/2001JB000596>
- Uieda, L., Tian, D., Leong, W. J., Jones, M., Schlitzer, W., Grund, M., et al. (2022, July). PyGMT: A Python interface for the Generic Mapping Tools. Zenodo. <https://doi.org/10.5281/zenodo.6702566>
- Van der Woerd, J., Ryerson, F. J., Tapponnier, P., Gaudemer, Y., Finkel, R., Meriaux, A. S., et al. (1998). Holocene left-slip rate determined by cosmogenic surface dating on the Xidatan segment of the Kunlun fault (Qinghai, China). *Geology*, 26(8), 695–698. [https://doi.org/10.1130/0091-7613\(1998\)026%3C0695:HLSRDB%3E2.3.CO;2](https://doi.org/10.1130/0091-7613(1998)026%3C0695:HLSRDB%3E2.3.CO;2)
- Van der Woerd, J., Xu, X., Li, H., Tapponnier, P., Meyer, B., Ryerson, F. J., et al. (2001). Rapid active thrusting along the northwestern range front of the Tanghe Nan Shan (western Gansu, China). *Journal of Geophysical Research: Solid Earth*, 106(B12), 30475–30504. <https://doi.org/10.1029/2001JB000583>
- Van der Woerd, J. V. der, Ryerson, F. J., Tapponnier, P., Meriaux, A.-S., Gaudemer, Y., Meyer, B., et al. (2000). Uniform slip-rate along the Kunlun Fault: Implications for seismic behaviour and large-scale tectonics. *Geophysical Research Letters*, 27(16), 2353–2356. <https://doi.org/10.1029/1999GL011292>
- Vernant, P., Bilham, R., Szeliga, W., Drupka, D., Kalita, S., Bhattacharyya, A. K., et al. (2014). Clockwise rotation of the Brahmaputra Valley relative to India: Tectonic convergence in the eastern Himalaya, Naga Hills, and Shillong Plateau. *Journal of Geophysical Research: Solid Earth*, 119(8), 6558–6571. <https://doi.org/10.1002/2014JB011196>
- Vigny, C., Socquet, A., Rangin, C., Chamot-Rooke, N., Pubellier, M., Bouin, M.-N., et al. (2003). Present-day crustal deformation around Sagaing fault, Myanmar. *Journal of Geophysical Research: Solid Earth*, 108(B11). <https://doi.org/10.1029/2002JB001999>
- Volkmer, J. E., Kapp, P., Guynn, J. H., & Lai, Q. (2007). Cretaceous-Tertiary structural evolution of the north central Lhasa terrane, Tibet. *Tectonics*, 26(6), n/a–n/a. <https://doi.org/10.1029/2005TC001832>
- Wang, E., & Burchfiel, B. C. (2000). Late Cenozoic to Holocene deformation in southwestern Sichuan and adjacent Yunnan, China, and its role in formation of the southeastern part of the Tibetan Plateau. *GSA Bulletin*, 112(3), 413–423. [https://doi.org/10.1130/0016-7606\(2000\)112%3C413:LCTHDI%3E2.0.CO;2](https://doi.org/10.1130/0016-7606(2000)112%3C413:LCTHDI%3E2.0.CO;2)

- Wang, G., Wan, J., Wang, E., Zheng, D., & Li, F. (2008). Late Cenozoic to recent transtensional deformation across the Southern part of the Gaoligong shear zone between the Indian plate and SE margin of the Tibetan plateau and its tectonic origin. *Tectonophysics*, 460(1), 1–20. <https://doi.org/10.1016/j.tecto.2008.04.007>
- Wang, H., Wright, T. J., Liu-Zeng, J., & Peng, L. (2019). Strain Rate Distribution in South-Central Tibet From Two Decades of InSAR and GPS. *Geophysical Research Letters*, 46(10), 5170–5179. <https://doi.org/10.1029/2019GL081916>
- Wang, M., & Shen, Z.-K. (2020). Present-Day Crustal Deformation of Continental China Derived From GPS and Its Tectonic Implications. *Journal of Geophysical Research: Solid Earth*, 125(2), e2019JB018774. <https://doi.org/10.1029/2019JB018774>
- Wang, S., Chevalier, M.-L., Pan, J., Bai, M., Li, K., Li, H., & Wang, G. (2020). Quantification of the late Quaternary throw rates along the Yadong rift, southern Tibet. *Tectonophysics*, 790, 228545. <https://doi.org/10.1016/j.tecto.2020.228545>
- Wang, W., Qiao, X., Yang, S., & Wang, D. (2017). Present-day velocity field and block kinematics of Tibetan Plateau from GPS measurements. *Geophysical Journal International*, 208(2), 1088–1102. <https://doi.org/10.1093/gji/ggw445>
- Wang, W., Qiao, X., & Ding, K. (2021). Present-Day Kinematics in Southeastern Tibet Inferred From GPS Measurements. *Journal of Geophysical Research: Solid Earth*, 126(1), e2020JB021305. <https://doi.org/10.1029/2020JB021305>
- Wang, Yu, Sieh, K., Tun, S. T., Lai, K.-Y., & Myint, T. (2014). Active tectonics and earthquake potential of the Myanmar region: Active Tectonics of Myanmar. *Journal of Geophysical Research: Solid Earth*, 119(4), 3767–3822. <https://doi.org/10.1002/2013JB010762>
- Wang, Yang, Wang, P., Ge, W., Zhou, R., Schoenbohm, L. M., Zhang, B., et al. (2019). Differential crustal deformation across the Cona-Oiga rift, southern Tibetan Plateau. *Journal of Asian Earth Sciences*, 177, 177–185. <https://doi.org/10.1016/j.jseas.2019.03.023>
- Wesnousky, S. G., Kumar, S., Mohindra, R., & Thakur, V. C. (1999). Uplift and convergence along the Himalayan Frontal Thrust of India. *Tectonics*, 18(6), 967–976. <https://doi.org/10.1029/1999TC900026>
- Wessel, P., Luis, J. F., Uieda, L., Scharroo, R., Wobbe, F., Smith, W. H. F., & Tian, D. (2019). The Generic Mapping Tools Version 6. *Geochemistry, Geophysics, Geosystems*, 20(11), 5556–5564. <https://doi.org/10.1029/2019GC008515>
- Wright, T., Fang, J., Ou, Q., Hooper, A., Lazecky, M., Maghsoudi, Y., et al. (2021). How does Tibet deform? A high-resolution 3D velocity field for the India-Eurasia collision from Sentinel-1 InSAR and GNSS. In *AGU Fall Meeting Abstracts* (Vol. 2021, pp. G22A–04). Retrieved from <https://ui.adsabs.harvard.edu/abs/2021AGUFM.G22A..04W>
- Wu, Z., Cao, Z., Shentu, B., & Deng, Q. (1992). Seismogenic structures of the 1411 southern Damxung earthquake of M= 8 in Tibet. *Earthquake Research in China*, 8(2), 46–52.
- Xu, Xiwei, Wen, X., Zheng, R., Ma, W., Song, F., & Yu, G. (2003). Pattern of latest tectonic motion and its dynamics for active blocks in Sichuan-Yunnan region, China. *Science in China Series D: Earth Sciences*, 46(2), 210–226. <https://doi.org/10.1360/03dz0017>
- Xu, Xiwei, Wen, X., Yu, G., Zheng, R., Luo, H., & Zheng, B. (2005). Average slip rate, earthquake rupturing segmentation and recurrence behavior on the Litang fault zone, western Sichuan Province, China. *Science in China Series D: Earth Sciences*, 48(8), 1183–1196. <https://doi.org/10.1360/04yd0072>
- Xu, XiWei, Wen, X., Chen, G., & Yu, G. (2008). Discovery of the Longriba Fault Zone in Eastern Bayan Har Block, China and its tectonic implication. *Science in China Series D-Earth Sciences*, 51(9), 1209–1223. <https://doi.org/10.1007/s11430-008-0097-1>
- Xu, Xiwei, Wen, X., Yu, G., Chen, G., Klinger, Y., Hubbard, J., & Shaw, J. (2009). Coseismic reverse-and oblique-slip surface faulting generated by the 2008 Mw 7.9 Wenchuan earthquake, China. *Geology*, 37(6), 515–518. Retrieved from <http://geology.gsapubs.org/content/37/6/515.short>

- 1726 Yang, T.-N., Hou, Z.-Q., Wang, Y., Zhang, H.-R., & Wang, Z.-L. (2012). Late Paleozoic to Early Mesozoic tectonic
1727 evolution of northeast Tibet: Evidence from the Triassic composite western Jinsha-Garzê-Litang suture. *Tectonics*,
1728 31(4). <https://doi.org/10.1029/2011TC003044>
- 1729 Ye, T., Chen, A., Hou, M., Niu, C., & Wang, Q. (2021). Characteristic of the Bodong segment of the Tanlu Fault
1730 Zone, Bohai sea area, eastern China: Implications for hydrocarbon exploration and regional tectonic evolution.
1731 *Journal of Petroleum Science and Engineering*, 201, 108478. <https://doi.org/10.1016/j.petrol.2021.108478>
- 1732 Yin, A., Dang, Y.-Q., Wang, L.-C., Jiang, W.-M., Zhou, S.-P., Chen, X.-H., et al. (2008). Cenozoic tectonic evolution
1733 of Qaidam basin and its surrounding regions (Part 1): The southern Qilian Shan-Nan Shan thrust belt and
1734 northern Qaidam basin. *Geological Society of America Bulletin*, 120(7-8), 813–846. Retrieved from <http://gsabulletin.gsapubs.org/content/120/7-8/813.short>
1735
- 1736 Yu, Z., Yin, N., Shu, P., Li, J., Wei, Q., Min, W., & Zhang, P. (2018). Late Quaternary paleoseismicity and seismic
1737 potential of the Yilan-Yitong Fault Zone in NE China. *Journal of Asian Earth Sciences*, 151, 197–225. <https://doi.org/10.1016/j.jseae.2017.10.038>
1738
- 1739 Yuan, D.-Y., Champagnac, J.-D., Ge, W.-P., Molnar, P., Zhang, P.-Z., Zheng, W.-J., et al. (2011). Late Quaternary
1740 right-lateral slip rates of faults adjacent to the lake Qinghai, northeastern margin of the Tibetan Plateau. *GSA*
1741 *Bulletin*, 123(9-10), 2016–2030. <https://doi.org/10.1130/B30315.1>
- 1742 Zhang, B., Liao, Y., Guo, S., Wallace, R. E., Bucknam, R. C., & Hanks, T. C. (1986). Fault scarps related to the 1739
1743 earthquake and seismicity of the Yinchuan graben, Ningxia Huizu Zizhiqu, China. *Bulletin of the Seismological*
1744 *Society of America*, 76(5), 1253–1287. <https://doi.org/10.1785/BSSA0760051253>
- 1745 Zhang, G., Qu, C., Shan, X., Song, X., Zhang, G., Wang, C., et al. (2011). Slip distribution of the 2008 Wenchuan
1746 Ms 7.9 earthquake by joint inversion from GPS and InSAR measurements: A resolution test study: Slip
1747 distribution of 2008 Wenchuan earthquake. *Geophysical Journal International*, 186(1), 207–220. <https://doi.org/10.1111/j.1365-246X.2011.05039.x>
1748
- 1749 Zhang, P.-Z., Shen, Z., Wang, M., Gan, W., Bürgmann, R., Molnar, P., et al. (2004). Continuous deformation
1750 of the Tibetan Plateau from global positioning system data. *Geology*, 32(9), 809–812. Retrieved from <http://geology.gsapubs.org/content/32/9/809.short>
1751
- 1752 Zheng, W., Zhang, P., He, W., Yuan, D., Shao, Y., Zheng, D., et al. (2013). Transformation of displacement
1753 between strike-slip and crustal shortening in the northern margin of the Tibetan Plateau: Evidence from
1754 decadal GPS measurements and late Quaternary slip rates on faults. *Tectonophysics*, 584, 267–280. <https://doi.org/10.1016/j.tecto.2012.01.006>
1755
- 1756 Zinke, R., Dolan, J. F., Rhodes, E. J., Van Dissen, R., & McGuire, C. P. (2017). Highly Variable Latest Pleistocene-
1757 Holocene Incremental Slip Rates on the Awatere Fault at Saxton River, South Island, New Zealand, Revealed
1758 by Lidar Mapping and Luminescence Dating. *Geophysical Research Letters*, 44(22), 11, 301–11, 310. <https://doi.org/10.1002/2017GL075048>
1759
- 1760 Zubovich, A. V., Wang, X., Scherba, Y. G., Schelochkov, G. G., Reilinger, R., Reigber, C., et al. (2010). GPS velocity
1761 field for the Tien Shan and surrounding regions. *Tectonics*, 29(6). <https://doi.org/https://doi.org/10.1029/2010TC002772>
1762